NASA Contractor Report 189703

P. 86

Air-Breathing Hypersonic Vehicle Guidance and Control Studies: An Integrated Trajectory/Control Analysis Methodology Phase II

Philip D. Hattis
Harvey L. Malchow

The Charles Stark Draper Laboratory, Inc.
Cambridge, Massachusetts

Contract NAS1-18565
October 1992

National Aeronautics and
Space Administration

Langley Research Center
Hampton, Virginia 23665-5225

Table of Contents

Table of Contents (Cont.)

Table of Contents (Cont.)

Table of Figures

Table of Figures (Cont.)

I. Task Synopsis

Air-breathing hypersonic vehicles, with fully integrated airframe and propulsion systems, are expected to face the most complicated design, trajectory, and control coupling challenges of any class of flight vehicles ever considered. Assessment of appropriate trajectory management and control strategies must be accomplished during the conceptual phases of vehicle design to assure a high probability that the fully integrated system will accomplish mission objectives. Also, a valid mathematical basis is needed to rate the relative performance of alternative vehicle design concepts and/or subsystem technologies against a common mission goal. To address these concerns, a generically applicable methodology has been developed under phase I of this task to generate and evaluate single-stage-to-orbit air-breathing hypersonic vehicle flight profiles. Capable of developing trajectory/control histories in an integrated manner, the formulation includes direct treatment of physically derived inequality constraints and permits determination of optimal propulsive mode phasing.

During the phase II effort reported here, the air-breathing flight analysis capabilities of the integrated analysis algorithm have been assessed by generation of near-minimum-fuel trajectories and desired control strategies using two different vehicle models and orbit targets. Both models used tabulated winged-cone accelerator vehicle representations that are combined with a multidimensional cubic spline data smoothing routine. Near-fuel-optimal, horizontal takeoff trajectories, imposing a dynamic pressure limit of 1000 psf, were developed.

The initial analysis methodology demonstration involved a polar orbit track with a target air-relative velocity of 25,000 ft/s. This case used an existing air-breathing propulsion model and included the dynamic effects of using elevons to maintain longitudinal trim. Analysis of results indicated problems with the adequacy of the propulsion model and highlighted dynamic pressure/altitude instabilities when using vehicle angle of attack as a control variable. Similar instabilities were encountered by Langley representatives in in-house trajectory studies for hypersonic vehicles. The Langley studies showed that use of pitch attitude relative to the local vertical as a control variable instead of angle of attack eliminates dynamic pressure/altitude instabilities, and suggested use of pitch attitude as control in the trajectory optimization algorithm. Application of the pitch control variable in this study showed a continued tendency toward dynamic pressure/altitude oscillation, but without divergent instability. Another observed effect was the magnitude of computed elevon deflections to maintain trim which suggests a need for an alternative pitch moment management strategy.

The second analysis methodology demonstration case reformulated the vehicle model and associated derivatives to use vehicle pitch attitude relative to the local vertical as the control variable. A new, more realistic, air-breathing propulsion model was incorporated. Also, to further simplify subsequent analysis, pitch trim calculations were dropped and an equatorial orbit was specified. A target altitude of 400,000 ft was established with states that institute a 100 NM apogee by 0 NM (sea level) perigee orbit. Changes in flight characteristics resulting from the effects of the new propulsion model were identified. Flight regimes demanding rapid attitude changes were characterized. Also, some issues regarding design of closed-loop controllers are ascertained.

The demonstration cases provided examples of the kind of information that the analysis methodology can develop for a wide range of HSV designs and mission applications. Near-fuel-optimal trajectories that satisfy the applied constraints were determined. Previously unspecified propulsive discontinuities were located. Flight regimes demanding rapid attitude changes were identified, dictating control effector and closed-loop G&C design requirements based on the required control response. Also, inadequacies in vehicle model representations and specific subsystem models with insufficient fidelity were determined.

After completion of analysis of the information resulting from use of the integrated trajectory/control methodology, closed-loop guidance and control design requirements can be established. This information must precede specification of on-board advanced information processing system design characteristics.

II. Introduction (Background on Task)

II.A. Problem Overview

Hypersonic air-breathing vehicles (HSVs) are under consideration for a range of advanced flight applications including horizontal single-stage-to-orbit (SSTO) launch operations. Relying on aerodynamic lift and air-breathing propulsion, the performance of these vehicles will be very sensitive to the trajectory management strategy. Additionally, all proposed HSV concepts have physical coupling between propulsion performance, aerodynamics, and trajectory dynamics to a degree that greatly exceeds previous flight vehicle experience. Even under ideal circumstances, much of the HSV ascent is accomplished by engines which produce only slightly more thrust than the overall vehicle drag. To achieve adequate acceleration, HSVs must operate much of the time near structural and/or thermal limits of the airframe, necessitating explicit treatment of those constraints in the trajectory management strategy. Multiple distinct air-breathing propulsive modes are likely, and a rocket capability is required to complete flight from subsonic takeoff conditions to the target orbit state. A poor guidance and control (G&C) implementation can result in reduced propulsive performance and excessive aerodynamic losses, possibly preventing successful accomplishment of mission objectives. Therefore, successful HSV trajectory management will be dependent on the development of a G&C system that efficiently manages the vehicle ascent path while accommodating the coupled system dynamics.

With currently anticipated technology, the HSV SSTO mission is at best marginally feasible. To achieve the SSTO capability with a significant payload, it is essential that near-minimum-fuel-to-orbit trajectories be flown. The relative merits of alternative vehicle configurations, subsystem technologies, and G&C design concepts can only be assessed in a valid manner if the comparative performance standard assures consideration of efficient trajectories for each case. To accomplish this, a generic tool that would generate near-minimum-fuel-to-orbit trajectory solutions for a wide variety of HSVs is required. The methodology should account for effects of key physical design constraints, the timing of propulsive phasing, and the principal sources of drag losses in order to provide an accurate indication of system performance and to evaluate desired G&C strategies.

Upon completion of development of integrated generic methodologies that determine near-optimal trajectory management and control strategies for HSVs, it is necessary to demonstrate the ability of the resulting tools to contribute to system performance analysis and design sensitivity studies. These capabilities are needed to support closed-loop G&C design requirements definition.

Application of the capabilities discussed above will help enable successful development of HSVs meeting a wide range of operational objectives.

II.B. Summary of Phase I Progress

During phase I of this task (performed from June 1990 to March 1991), a generic methodology to permit integrated trajectory/control analysis for generic HSVs was implemented [Ref. 1]. Including the effects of physically derived constraints, the methodology was successfully adapted from previously developed Draper Laboratory analysis tools [Refs. 2-5] to the assessment of single-stage-to-orbit HSVs with multi-mode propulsion systems. Both an overall trajectory evaluation algorithm and a preliminary near-fuel-optimal trajectory development tool were mathematically formulated and implemented for use in a work station computational environment. The methodology is capable of assessing the relative performance of alternative vehicles and/or subsystem technologies with respect to a single mathematically valid measure. To assure good numerical behavior of the analysis algorithms, a cubic spline based data smoothing routine was developed and included in the resulting tool to permit use of multidimensional tabulated vehicle models.

Efforts to demonstrate the generic analysis tool were initiated. A seven state vehicle dynamics model which included treatment of incremental forces due to maintenance of vehicle longitudinal moment trim was constructed. Angle of attack and fuel/air equivalence ratios were utilized as control variables based on a desire to permit some intuitive analysis to be applied. The model was implemented on a work station including all relevant partial derivatives.

A specific preliminary test case of the hypersonic vehicle integrated trajectory/control analysis methodology was defined, performed, and evaluated to get an early assessment of the capabilities of the algorithm. To limit the computational effort to derive some results during phase I of the task, the trajectory was derived by sequential computation of several trajectory segments from takeoff to high Mach flight. The computational procedures were based on methods developed under the task to construct suitable initial representations of the trajectory needed for overall integrated optimization. The performance data utilized by the example vehicle model was based on an early version of an air-breathing accelerator, winged-cone vehicle database [Ref 6]. Performance from horizontal takeoff to 20,000 ft/s relative airspeed on a polar orbit track was determined. A dynamic pressure constraint of 1000 psf was enforced. The following list summarizes some of the most significant phase I conclusions:

- Three near-fuel-optimal flight segments were derived that satisfy the applied constraints. They successively cover flight from horizontal takeoff to Mach 2, Mach 2 to 10,000 ft/s, and 10,000 ft/s to 20,000 ft/s (where velocity was specified in terms of relative air speed). Segment boundary condition matching criteria were enforced to permit eventual merger (during phase II) of the individual segment results into a single full trajectory usable for overall optimization.
- The analysis methodology was able to identify previously unspecified discontinuities and phasing characteristics in the vehicle propulsion model. This information was used to identify appropriate model improvements for phase II studies.
- Flight regimes with strong performance sensitivities and inadequate model fidelity were highlighted.
- Data to determine lower bound control effector response times and the remaining effector control authority after accounting for longitudinal moment trim was generated.
- Drag losses due to required elevon activity was shown to be very high, demonstrating a need to consider alternate longitudinal moment management strategies and/or effectors for the vehicle.

When analysis results were considered collectively, they showed the potential of the methodology to provide much of the information needed to define guidance and control system design requirements. Based on these results, more complete demonstration of the methodology was planned under phase II of the task.

III. List of Symbols and Acronyms

a	the atmospheric speed of sound (a function of r)
AIPS	advanced information processing system
C_D	the vehicle drag coefficient (a function of M_f and α)
C_J	a coefficient to establish the desired weight given to cost improvement contributions to variation terms
C_L	the vehicle lift coefficient (a function of M_f and α)
C_Q	the dynamic pressure constraint cost weighting term
C_T	the vehicle air-breathing engine thrust coefficient derived from the Langley data base with dimension ft^2 (a function of Φ_a and M_f)
C_Ψ	a diagonal matrix of constant coefficients to establish the desired weights given to equality constraint violation improvements in variation terms
D	the drag force acting on the vehicle
f	the derivative of the state vector x with respect to time
f_i	the derivative of x_i with respect to time
f_u	the partial derivative of the vector f with respect to the control vector u
f_x	the partial derivative of the vector f with respect to the state vector x
F	the LVLH vector of forces acting on the vehicle
F_g	the gravity force acting on the vehicle
F_T	the force component parallel to the vehicle free stream velocity vector
F_N	the force component normal to the vehicle free stream velocity vector, pointing down in the vehicle plane of symmetry
F_1	the force component normal to F_2 and F_3, pointing toward increasing μ
F_2	the force component parallel to the equatorial plane, pointing eastward, normal to F_3
F_3	the force component parallel to r - points toward Earth
g_0	a constant representing the number of pounds mass per slug (approx. 32.2)
G&C	guidance and control
h	vehicle altitude
H	the Hamiltonian
H_u	the partial derivative of the Hamiltonian H with respect to the control vector u
HSV	hypersonic vehicle
I_{JJ}	a scalar influence function of cost
I_{sp_a}	the air-breathing engine specific impulse derived from the Langley data base with dimension sec (a function of Φ_a and M_f)
$I_{\Psi J}$	a vector influence function of constraints and cost
$I_{\Psi_i J_i}$	a vector influence function of constraints and cost for the i^{th} trajectory segment

$\mathbf{I}_{\mathbf{vv}}$	a matrix influence function of constraints
J	a mathematical cost imposed on the system
J_s	a heuristically determined specified cost improvement
L	the distributed mathematical cost term
L_u	the partial derivative of the distributed mathematical cost term L with respect to the control vector u
L_x	the partial derivative of the distributed mathematical cost term L with respect to the state vector x
L	the distributed mathematical cost term
l	the lift force acting on the vehicle
L_u	the partial derivative of the distributed mathematical cost term L with respect to the control vector u
L_x	the partial derivative of the distributed mathematical cost term L with respect to the control vector x
LaRC	Langley Research Center
LVLH	the local vertical/local horizontal reference frame
m	the vehicle mass
m_a	the air-breathing engine fuel mass
m_0	the vehicle mass at takeoff
M_f	the free stream Mach number
NM	nautical miles
psf	pounds per square foot
Q	the dynamic pressure
Q_D	the desired dynamic pressure constraint bound
r	the vehicle distance from the center of the Earth
r_e	the radius of the Earth
r_{targ}	the target circular orbit altitude
r_0	the vehicle distance from the center of the Earth at takeoff
S_{ref}	the vehicle reference wing area
SSTO	single-stage-to-orbit
t	time
T	the thrust force acting on the vehicle
u	the control vector
u_a	the control for the air-breathing engine
u_i	the i^{th} element of the control vector
u_0	a step function which changes from 0 to 1 at a functional value designated in brackets
U	a diagonal matrix of functions of time to weight different elements of the control variation vector
v_D	the free stream velocity magnitude at the desired atmospheric exit conditions

v_f	the vehicle velocity magnitude relative to the free stream
v_1	the free stream velocity component normal to v_2 and v_3, pointing toward increasing μ
v_{1_0}	the northerly component of the takeoff velocity
v_2	the free stream velocity component parallel to the equatorial plane, pointing eastward, normal to v_3
v_{2_0}	the easterly component of the takeoff velocity
v_3	the vehicle free stream velocity component parallel to r (points toward Earth)
v_{3_D}	the desired vehicle free stream velocity component at takeoff parallel to r at atmospheric exit (points toward Earth)
v_{3_0}	the vehicle free stream velocity component at takeoff parallel to r (points toward Earth)
x	the state vector
x_i	the i^{th} component of the state vector x
x_0	the vehicle state vector at takeoff
α	the vehicle angle of attack
γ	the vehicle flight path angle
δ_e	the elevon deflection angle
θ	the vehicle pitch attitude relative to the Earth's surface
λ	the costate vector
Λ	a matrix influence function of equality constraints
μ	latitude, measured positive northward from the equator
μ_e	Earth's gravitational constant
μ_0	the takeoff latitude
ν	longitude, measured eastward
ν_0	the takeoff longitude
ρ	the atmospheric density (a function of r)
t_f	the terminal time of the trajectory
ϕ	the terminal cost term
ϕ_x	the partial derivative of the terminal cost term ϕ with respect to the state vector x
Φ_a	the air-breathing engine equivalence ratio
ψ	the flight azimuth angle
Ψ	tne equality constraint vector
Ψ_x	the derivative of the equality constraint vector Ψ with respect to the control vector x
ω_e	the Earth's rotation rate (.00418 deg/s)
Ω	the state integration cutoff function
Ω_x	the derivative of the cutoff function Ω with respect to the state vector x
()	when used in figures, indicates a negative number

IV. Research Goals

A number of research goals were set for this task. Some of them have been the focus of the phase II work done between April 1991 and March 1992, while the remainder have established guidelines for work under possible future efforts.

IV.A. Phase II Task Focus

SSTO HSVs are likely to have limited performance margins. Their delivered payload capacity will be very adversely affected by non-ideal flight conditions and/or G&C strategies. The most efficient trajectories, control strategies, and propulsive phasing histories that satisfy all relevant performance constraints must be identified and utilized. New methodologies to determine efficient, constrained HSV ascent trajectories are required.

Initial phase I activity on this task focussed on the implementation and preliminary demonstration of a novel generic HSV integrated trajectory/control analysis methodology. The resulting tool can determine HSV ascent paths that maximize payload performance while satisfying relevant constraints. Data derived using the methodology can also support development and assessment of G&C strategies for managing the flight path and propulsive phasing.

Phase II completed demonstration of the analysis methodology using two combinations of vehicle models and trajectory target conditions. Specific trajectory results were derived under realistic flight constraints. Interpretation of the resulting trajectory/control profiles has attempted to characterize the type of information that can be gleaned using the analysis methodology. The following subtasks were pursued:

IV.A.1. Completion of Analysis Using Phase I Vehicle Model

An HSV vehicle model which included the aerodynamic effects of maintaining longitudinal pitch trim with elevon was incorporated into the analysis tool as part of the phase I task work. Using angle of attack as a control, incorporating an early version of the propulsion model, targeting for a polar orbit, and constraining dynamic pressure to an upper bound near 1000 psf, a sequential series of flight segments were generated to assess expected vehicle performance to 20,000 ft/s relative air speed. Under phase II, an integrated optimization was performed for a single flight segment from Mach 2 (1950 ft/s) to 25,000 ft/s relative air speed. A separate flight segment from horizontal takeoff to Mach 2 was separately computed for reasons discussed in Ref. 1.

IV.A.2. Identification of Issues Resulting from Use of Phase I Implementation

Careful review during phase II of results derived from use of the phase I vehicle model was performed. The focus was to identify any state equation, algorithm, and model deficiencies that required attention to permit effective subsequent use of the analysis algorithm. Several significant problems were identified. These are summarized below, with their resolution discussed in subsequent sections of the report:

- The polar orbit state equations were found to have a singularity at the Earth's poles that would could cause the trajectory integration to break down if approached within a degree. The trajectory under study came within one degree of the pole at a relative air speed of about 21,000 ft/s.
- Use of angle of attack as a longitudinal control variable was found to produce a open loop instability during trajectory optimization. The effect was to produce a weakly divergent dynamic pressure oscillation at high Mach numbers around the upper bound (due to associated small altitude fluctuations). Since the period was about 200 seconds, the problem only became apparent when flight segments under analysis grew well beyond 1000 seconds duration.

- The phase I propulsion model manifested some inconsistencies when used in the analysis algorithm. The model specified separate calculations of specific impulse and thrust coefficient (which in fact are functionally related) causing great sensitivity to the effects of individual, small database errors. Contrary (and incorrect) performance trends for the two engine performance variables sometimes resulted. Unreasonable jumps in system performance as a function of Mach number were implied which caused convergence problems for the integrated analysis optimization algorithm.

IV.A.3. Algorithm Evaluation With Alternative Phase II Vehicle Model

The integrated analysis algorithm was demonstrated over an entire trajectory, from horizontal takeoff to atmospheric exit, using an updated phase II vehicle model. Problems identified using the phase I vehicle model were resolved, and subsequently some additional model simplifications were incorporated to expedite results. A new attitude control variable was introduced, the propulsion model was improved, treatment of elevon effects was removed, and the trajectory target was changed to an equatorial orbit. Results were evaluated to assess the kinds of information available from application of the analysis algorithm.

IV.B. Longer Term Research Objectives

The task statement of work identifies several investigation paths which are intended as directions for research under possible future efforts. These are summarized below:

IV.B.1. Treatment of Overlapping Air-Breathing/Rocket Propulsive Phases

The integrated analysis methodology includes features that permit determination of the optimal timing of discrete propulsive mode transitions (if explicitly modeled). With the inclusion of a rocket propulsion system in the vehicle model, the basis for its best application can be determined including possible overlapping operations with the air-breathing engine. The potential for significant HSV operational performance improvements could be explored using this algorithm feature.

IV.B.2. Treatment of Vehicle Thrust Direction and Pitch Moment Changes with Angle of Attack

The initial example HSV models included propulsion systems that represented thrust magnitude as independent of angle of attack and forced thrust direction to always be in the longitudinal body axis. More realistic vehicle models specify the thrust magnitude and direction as functions of angle of attack, which also implies associated longitudinal moment variations. This subtask would characterize the changes in HSV trajectory management and control strategies that result from explicit consideration of angle of attack effects on propulsion performance.

IV.B.3. Incorporation of Thermal Constraints into Trajectory Results

The integrated trajectory/control analysis methodology supports treatment of inequality constraints which are functionally dependent on both states and controls. However, the initial demonstration cases were restricted to studying the effects of dynamic pressure inequality constraints which are only state dependent. Treatment of thermal constraints would address an important physical performance limitation that has both state and control dependencies. This subtask would incorporate a vehicle stagnation point thermal flux constraint and assess its qualitative effects on mission performance and G&C strategies.

IV.B.4. HSV G&C Performance Robustness Studies

Uncertainty in the environment model and expected vehicle dynamics are important design considerations for HSV G&C systems. The atmosphere can experience significant density variations at the higher HSV air-breathing altitudes. The aerodynamic and propulsion performance of HSVs may not be accurately modelled before there is significant flight experience and may

vary between vehicles or for a given vehicle on different flights. The likelihood of successfully accomplishing specific mission objectives depends on understanding the effects of these uncertainties and designing a G&C system that is robust enough to handle them. This subtask would evaluate the performance of the near-fuel-optimal HSV trajectories and candidate closed-loop G&C systems in the presence of aerodynamic variations, propulsion modelling uncertainties, and atmospheric disturbances. These uncertainty effects would be evaluated for a range of applicable inequality constraint bounds.

V. Progress for April 1991 - March 1992

The phase II technical effort under this task was performed between April 1991 and March 1992. During this period the analysis methodology assessment using the example HSV model provided by the government during phase I was completed. Some issues regarding the model characteristics and the selection of control variables were identified. Also, some features of the vehicle model and orbit target states were found unessential to further algorithm assessment. An improved vehicle model was provided by the government, control vector changes were made, and new analysis simplifications were incorporated. Based on the new model and assumptions, additional algorithm assessment studies were accomplished. Details on these phase II studies follow.

V.A. Analysis with Phase I Vehicle Models

During phase I studies analysis of a near-fuel-optimal polar trajectory from horizontal takeoff to 20,000 ft/s relative air speed was achieved by combining several sequentially derived trajectory segments. The same vehicle model was used during phase II to perform an integrated trajectory/control analysis on a single segment spanning flight from Mach 2 to 25,000 ft/s relative air speed. (Reference 1 explains why Mach 2 was selected as an initial condition.) The following subsections detail the case run and results of subsequent analysis.

V.A.1. Summary of Case Run

An HSV model implemented during the phase I work represented a winged-cone configuration with elevon use required to maintain longitudinal moment trim. Aerodynamics were represented as a combination lift and drag contributions from the airframe and elevons with dependency on Mach number, angle of attack, and deflection angle of elevons. The air-breathing propulsion model represented specific impulse and thrust coefficient separately as functions of Mach number, dynamic pressure, and fuel/air equivalence ratio. Angle of attack and equivalence ratio were selected as time varying controls. An upper bound of 1000 psf was imposed on dynamic pressure. For the phase II study, the trajectory was based on horizontal takeoff from 28.5 deg latitude with a polar orbit target. Results of phase I studies were used to initialize the phase II analysis of a trajectory going from Mach 2 (1950 ft/s relative air speed) to 25,000 ft/s relative air speed.

V.A.2. Numerical Orbit Integration Issues Resulting from Polar Orbit Target

A significant numerical problem was encountered as a result of the polar orbit target. The selected trajectory went very close (within 0.8 deg) of the north pole at about 21,000 ft/s relative airspeed. In initial analysis efforts, the trajectory integration numerically diverged at the closest approach to the pole. The problem was traced to calculation of the flight azimuth angle, ψ, which is derived from the arc tangent function of the ratio of easterly airspeed to the northerly airspeed velocity (components 2 and 1 respectively in figure 1). The arc tangent function range of applicability is -90 deg to +90 deg. Calculations over this range asymptotically diverge at the north pole (+90 deg). Mathematical manipulation of the form of the dynamics equations to exclusively utilize inverse trigonometric functions applicable over a range from 0 deg to 180 deg (e.g. arc cotangent) resolved the problem.

V.A.3. Overview of Trajectory/Control Analysis Results

Various state, control, and effector variable histories were generated by the trajectory/control analysis algorithm. Data were generated for the flight segment from Mach 2 to 25,000 ft/s relative air speed. For completeness, when plots were generated for specific variables, the separately derived results for takeoff to Mach 2 were included. The flight from takeoff to Mach 2 took 92.2 seconds. Transients seen where the two flight segments merge at Mach 2 are discussed in reference 1.

Altitude, Mach Number, and Dynamic Pressure

Figures 2 and 3 plot altitude and Mach number vs time respectively. On the scale of the plot, both variables are seen to be virtually monotonic, with their rate of increase declining after the first 300 seconds of flight. The dynamic pressure, Q, is seen in figures 4 and 5 to reach the bound of 1000 psf within that rapid climb interval , around Mach 2. The dynamic pressure limit is closely tracked for the remainder of flight. A weakly divergent oscillatory instability in the dynamic pressure can be seen in figure 4 after the first 500 seconds of flight (discussed in more detail later).

Controls

The equivalence ratio control variable (phi), is plotted in figures 6 and 7, and the angle of attack control history is plotted in figures 8 and 9. Significant equivalence ratio peaks are seen in the low Mach regime and near Mach 6. The low Mach peak correlates to a reduced angle of attack while getting through the high drag transonic regime. The Mach 6 equivalence ratio peak correlates to steep changes in propulsion model data which demands corresponding sizeable, short duration changes in the angle of attack. Other sudden changes in equivalence ratio are seen at higher Mach numbers (with some associated angle of attack transients near Mach 8). During high Mach flight, the angle of attack declines relatively smoothly due to reduced lift requirements as orbital speed is approached. The discontinuous equivalence ratio is evidence of inadequacies in the phase I propulsion model which helped motivate a subsequent model change.

Elevon Deflection

The elevon deflection angle (delta), used to maintain vehicle longitudinal moment trim, is plotted in figures 10 and 11. The trim angle bottoms out above Mach 10 at a value near -17 deg. With a ±20 deg stop on the elevons, little attitude transient control capability remains. Also, sustained high elevon deflection introduces high drag penalties. The elevon deflection decreases near orbital speed as the angle of attack declines. The elevon deflection history suggests that alternate moment control strategies are required. This was an issue that was not pursued in phase II due to lack of resources.

Flight Path Angle

The flight path angle (gamma) is plotted against Mach number for the initial 500 seconds of flight in figure 12. The early peak is consistent with the rapid climb in flight shortly after takeoff. The very small flight path angle at high Mach numbers (gamma near 0) is consistent with the low rate of climb as orbital velocities are approached.

Acceleration

Figures 13 and 14 illustrate the inertial acceleration history of the phase I vehicle model. Significant, rapid changes are seen near specified propulsion model data points through Mach 8. Generally, acceleration levels off above about Mach 10.

Mass and Mass Flow

Figures 15-17 illustrate vehicle mass and mass flow histories. The mass history is nearly linear with time, unlike exponential decay curves for conventional rockets. The mass flow is highly variable, but consistent with the trends seen in vehicle acceleration, including a leveling off at high Mach.

Key Observations Using the Phase I Model

Completion of the analysis using the phase I model for a single flight segment from Mach 2 to 25,000 ft/s relative air speed leads to similar control concerns as discussed in reference 1.

- The elevon deflection angle history reflects large changes in vehicle trim characteristics due to Mach number dependent aerodynamic effects and vehicle mass changes. The combination of the vehicle design and control effector placement lead to high drag penalties and limited control authority over extended flight intervals.
- Some steep perturbations in the angle of attack can result from propulsion model variations (as seen below Mach 6). These effects put upper limits on attitude change response times.
- Significant problems exist in the phase I propulsion model which result in unrealistic equivalence ratio transients near propulsion model data points. An improved (more realistic) model should be used for subsequent studies.

V.A.4. Optimization Stability Problems Due to Use of Angle of Attack as a Control

The government supplied winged-cone vehicle model aerodynamic data base [Ref. 6] defines lift and drag coefficients as functions of Mach number and angle and angle of attack (as well as aerosurface deflections when their incremental contributions are considered). These dependencies make angle of attack a natural selection as a control variable. However, when the example analysis case was completed using the phase I vehicle model, the use of angle of attack was found to present significant problems.

Figure 18 plots dynamic pressure, Q, vs time starting 100 seconds after takeoff. Illustrated on a magnified scale, it can be seen that a weakly divergent oscillation with a period of about 200 seconds is propagated around the 1000 psf upper bound. The last cycle of the oscillation at the end of the trajectory shows evidence of going unstable. Figure 19 plots the altitude history starting 1000 seconds after takeoff. Also illustrated on a magnified scale, slight altitude fluctuations around an otherwise monotonic climb can be seen as the cause of the dynamic pressure oscillations. Similar instabilities were encountered by Langley representatives in in-house trajectory studies for hypersonic vehicles.

At least one previous study of air-breathing HSVs found similar problems with the use of angle of attack as a control [Ref. 7]. While the dynamics are very nonlinear, an approximate linearized eigenvalue analysis shows that perturbations to angle of attack control histories derived from an optimization algorithm can induce instability.

V.B. Algorithm and Model Improvements/Simplifications Due to Phase I Model Results

Upon completion of the example trajectory/control analysis case using the phase I vehicle model, a number of changes were made to improve and expedite subsequent phase II studies. Problems noted in the initial analysis were addressed. Additional simplifications were incorporated when warranted by results. The details of the major changes follow.

V.B.1. Change of Control Variable

In reference 7, a linearized analysis of the dynamics of an early HSV concept suggested that use of vehicle pitch attitude as a control instead of angle of attack could eliminate dynamic pressure/altitude instabilities. Recent in-house Langley studies of hypersonic vehicles also showed that use of pitch attitude relative to the local vertical as a control variable instead of angle of attack eliminates dynamic pressure/altitude instabilities. The vehicle control vector and the associated dynamics model (including all required partial derivatives) were reformulated to use a local vertical vehicle pitch angle the attitude control variable. This change is reflected in the updated model equations presented later in this report.

V.B.2. Replacement of Propulsion Model

The phase I vehicle propulsion model separated calculation of specific impulse and thrust coefficient. Its use in the example trajectory/control analysis case resulted in numerous jumps and/or transients in the equivalence ratio history which also affected the angle of attack profile. Careful analysis of the data base indicated some inconsistencies in the trends of the specific impulse and thrust coefficient data at each of the Mach regimes of concern. NASA/Langley representatives derived an improved propulsion model based on the actual functional relationship at specific impulse and thrust coefficient. For simplicity, the very weak dependence on dynamic pressure was also removed.

The phase II propulsion model is separated into two propulsive modes. The low speed model has a number of data points spanning Mach numbers from 0.3 to 2.0 and equivalence ratios from 0.5 to 2.0. The high speed model has a number of data points spanning Mach numbers from 2.0 to 25.0 and equivalence ratios from 0.25 to 5.0. As incorporated for further demonstration of the integrated trajectory/control algorithm, a discrete change is assumed to be made from the low speed model to the high speed model at Mach 2.

As was done for the aerodynamic data base and the phase I propulsion model during phase I studies, the phase II propulsion model implementation is processed through a cubic spline fit routine to assure continuous behavior of the relevant functions and their first derivatives. The smoothing of the data is performed to avoid trajectory/control optimization algorithm instabilities that could result from gradient calculations near data discontinuities. To illustrate the phase II propulsion model characteristics, outputs of the spline fitted data have been plotted for an array of Mach numbers and equivalence ratios. Figures 20-21 illustrate some cross sections of the thrust coefficient for the low speed and high speed phase respectively, and figures 22-23 illustrate similar cross sections of the phase II model's specific impulse. The spline data points were calculated at Mach number intervals of 0.5 which accounts for the segmented appearance of the plots. Data jumps actually occur in the propulsion model when the data base (the engine phase) changes discretely at Mach 2. The plotted data represents the low speed data at Mach 2, and the high speed data at Mach 2.5 with the entire set of plots drawn in a piecewise linear manner.

V.B.3. Elimination of Elevon Trim Calculations

Inclusion of elevon usage for longitudinal moment trim in the phase I vehicle model provided significant insight into pitch control authority restrictions and established upper bounds on required aerosurface response times. However, subsequent use of the example winged-cone vehicle for trajectory control/studies with the improved propulsion model was not expected to provide new insight into aerosurface control issues. Therefore, the longitudinal moment calculations and associated elevon trim deflection determination were removed for phase II model studies in order to reduce computational burden and complexity.

V.B.4. Change of Orbit Targets

Phase II integrated trajectory/control studies using phase I vehicle models aimed for polar flight paths with near orbital velocities. However, as work progressed, interest in polar orbit (once an objective of the NASP program) waned. Consideration instead of equatorial launch to equatorial orbit offered additional computational simplicity without compromising the qualitative algorithm evaluation objectives of phase II task studies. The new boundary conditions for studies using phase II vehicle models were defined as horizontal, equatorial takeoff with a target state at atmospheric exit on the way to low, circular, equatorial orbit. Equation formulation of these boundary conditions and associated derivatives are provided later in a section detailing the phase II model.

V.B.5. Updated Analysis Algorithm Formulation

The trajectory optimization algorithm uses a generalized steepest descent gradient two-point boundary value problem solution technique. The most general form of the Draper developed methodology is capable of solving simultaneously for vehicle configuration, trajectory, dynamic discontinuity times, and controls [Refs. 2-5]. It can accommodate equality and inequality constraints while optimizing with respect to a performance index of states, vehicle design parameters, controls, and time. In the phase II application, vehicle geometry is assumed fixed and propulsive continuities are not explicitly modeled, eliminating consideration of design parameters and discontinuity times. The optimization performance index J as applied to this problem has the form:

$$J(\tau) = \phi(x(\tau)) + \int_0^{\tau} L(x(t), u(t))dt \qquad \text{(Eq. 1)}$$

To reduce the state dimensionality for the phase II studies, rotation dynamics are not tracked. The resulting state vector is:

$$x = \begin{pmatrix} r \\ v \\ \mu \\ v_1 \\ v_2 \\ v_3 \\ m \end{pmatrix} \qquad \text{(Eq. 2)}$$

The applicable control vector for phase II only includes explicit treatment of air-breathing propulsion and vehicle pitch attitude:

$$u = \begin{pmatrix} u_1 \\ u_2 \end{pmatrix} = \begin{pmatrix} u_a \\ \theta \end{pmatrix} \qquad \text{(Eq. 3)}$$

The relationship between the first control vector element and the actual propulsion system throttle variable is:

$$\Phi_a = (u_a)^2 \qquad \text{(Eq. 4)}$$

A costate like function Λ is adjoined to the problem to explicitly treat a vector of applicable equality constraints functions called Ψ. The formulation for Λ is given in Eqs. 11-12. With the initial take-off conditions given, the equality constraints are needed to enforce the target orbit conditions at time τ. One smoothly varying target orbit state equality constraint is needed to determine τ. The target orbital velocity is used in this application and is therefore excluded from the adjoined function list. This trajectory integration cutoff function called Ω helps determine boundary conditions on the costate function λ, while the remaining equality constraints determine boundary conditions used in the adjoined function Λ. The formulation for λ is given in Eqs. 8-9.

The vehicle state equation is defined as follows:

$$\frac{dx}{dt} = f(x, u) \qquad \text{(Eq. 5)}$$

A forward integration cutoff condition is defined (e.g. target orbital velocity):

$$\Omega(x(\tau)) = 0 \qquad \text{(Eq. 6)}$$

A Hamiltonian is constructed after defining a costate vector λ which is determined by backwards integration:

$$H = L + \lambda^T f \qquad \text{(Eq. 7)}$$

where:

$$\frac{d\lambda}{dt} = -f_x^T \lambda - L_x^T \qquad \text{(Eq. 8)}$$

and where the backwards integration boundary condition is evaluated at the forward integration cutoff time τ:

$$\lambda^T(\tau) = \left(\phi_x - \left(\frac{\phi_x f + L}{\Omega_x f} \right) \Omega_x \right) |_{x(\tau), u(\tau)} \qquad \text{(Eq. 9)}$$

An equality constraint vector is constructed to accommodate the terminal state boundary conditions defined at the forward integration cutoff time τ:

$$\Psi(x(\tau)) = 0 \qquad \text{(Eq. 10)}$$

An additional adjoint variable, also determined by backwards integration, is defined to factor in the equality constraint functions (boundary conditions) at the terminal time:

$$\frac{d\Lambda}{dt} = -f_x^T \Lambda \qquad \text{(Eq. 11)}$$

where the backwards integration boundary condition is evaluated at the forward integration cutoff time τ:

$$\Lambda^T(\tau) = \left(\Psi_x - \frac{\Psi_x f \Omega_x}{\Omega_x f} \right) |_{x(\tau), u(\tau)} \qquad \text{(Eq. 12)}$$

It is helpful to introduce the following variables for subsequent notational simplicity where U is a diagonal matrix of coefficients used to weight the relative size of perturbations to the controls:

$$I_{\Psi\Psi} = \int_0^\tau \Lambda^T f_u U f_u^T \Lambda \, dt \qquad \text{(Eq. 13)}$$

$$I_{\Psi J} = \int_0^\tau \Lambda^T f_u U H_u^T dt \qquad \text{(Eq. 14)}$$

$$I_{JJ} = \int_0^\tau H_u U H_u^T dt \qquad \text{(Eq. 15)}$$

The resulting algorithm variational equation for the control vector u is:

$$\delta u = -U(f_u^T \Lambda I_{\Psi\Psi}^{-1} C_\Psi \Psi + C_J(H_u^T - f_u^T \Lambda I_{\Psi\Psi}^{-1} I_{\Psi J})) \qquad \text{(Eq. 16)}$$

where:

$$C_J = -\frac{dJ_s + (I_{\Psi J}^T I_{\Psi\Psi}^{-1} + g^T V M^T I_{\Psi\Psi}^{-1}) C_\Psi \Psi}{I_{JJ} - I_{\Psi J}^T I_{\Psi\Psi}^{-1} I_{\Psi J}} \qquad \text{(Eq. 17)}$$

With specification of dJ_s and C_Ψ, the variational equations can be used to perturb the desired control history on successive iterations through use of Eq. 19 to eventually achieve vehicle performance optimality while satisfying all applicable constraints. The scalar dJ_s reflects the specified cost improvement sought on each optimization algorithm iteration. The diagonal matrix C_Ψ weights the relative size of equality constraint improvements on each optimization algorithm iteration. Proper selection of these weightings as well as U is critical to the numerical stability and convergence rate of the optimization process.

There are several types of constraints applicable to HSV trajectory optimization. As is true for any two-point boundary value problem, it is necessary to apply equality constraints at the trajectory final target condition. These are treated by adjoining the variable Λ, thereby incorporating the influence of the boundary conditions.

There are constraints on some of the controls. An example would be a lower bound (fuel flow off) on throttle setting. Often such constraints can be treated by nonlinear mapping into a control space without bounds. Care must be taken when using nonlinear mapping to avoid initial solution guesses that specify mapped control values in insensitive regions of the actual control space.

Inequality constraints need to be applied as a result of physical design constraints such as dynamic pressure and thermal limits. For this methodology, penalty functions are introduced through the integral performance index L. This approach requires periodic adjustment of penalty function gains as the optimal solution is approached.

As is generally true when two-point boundary problem optimization algorithms are used, some application specific considerations are required to assure good algorithm performance for the HSV problem. These include the careful choice of the integration cutoff condition as well as special approaches to balancing the perturbations to boundary value constraint violations against perturbations to controls needed to improve performance. Failure to carefully treat these issues can prevent acceptable algorithm numerical behavior.

Unlike a rocket ascent to orbit, HSVs are more likely to follow a trajectory at low Mach numbers akin to supersonic fighter aircraft minimum time to climb profiles. Often this results in a "zoom maneuver" in the transonic range, where the vehicle uses already acquired potential energy (altitude), combined with thrust, to quickly transit the maximum drag environment near Mach 1 [Ref. 8]. The resulting ascent can involve a negative vertical velocity component for a short interval. The nonmonotonic behavior of this velocity component makes it an unacceptable parameter for algorithm integration cutoff. Either horizontal velocity or orbital energy state provides much greater likelihood of achieving acceptable state conditions at integration cutoff.

Successful convergence of the optimization algorithm to the desired minimum cost solution requires that the effort to drive the violation of the boundary conditions to zero be balanced against the effort to find an optimal control history. Each parameter requiring perturbation must be separately weighted, with the emphasis that each receives chosen to stress those variables that currently promise the most improvement without numerically destabilizing the algorithm. (Bad choices could induce highly nonlinear steps.) As the interim trajectory solution approaches

optimality, the relative sensitivity of the perturbed parameters change. Techniques must be applied to determine current sensitivity and modify the weightings as the algorithm progresses. In some instances, this may require acceptance of perturbations that do not uniformly improve all boundary value violations. A composite measure of proposed algorithm step acceptability can be constructed that takes precedence over individual variation effects, as discussed in ref. [Ref. 5].

Given an initial control history, the algorithm iteratively computes perturbations to the controls to improve the specified performance index while maintaining boundary conditions. Additive perturbation contributions are derived to improve the cost as well as to drive down violations of the equality constraints. Weighting functions balance the relative contributions of each additive perturbation term.

V.B.6. Updates to Model Equations Required for Algorithm Analysis

Changes were made in the example vehicle model during phase II studies to improve the quality of the propulsion system representation and to eliminate consideration of elevon use for longitudinal moment trim. In addition, when the new vehicle representation was applied, the algorithm demonstration case boundary conditions were updated from those used previously. The motivation for these changes was discussed in previous sections. The formulation details follow.

V.B.6.a. Vehicle State Dynamics Models

A seven state vehicle dynamics model can be written as follows in state equation form consistent with the frame of reference given in figure 1:

$$f = \begin{pmatrix} -x_6 \\ \dfrac{x_5}{x_1 \cos x_3} \\ \dfrac{x_4}{x_1} \\ \dfrac{x_4 x_6 - (x_5)^2 \tan x_3}{x_1} - 2\omega_e x_5 \sin x_3 - x_1 (\omega_e)^2 \sin x_3 \cos x_3 + \dfrac{F_1}{x_7} \\ x_5 \dfrac{(x_6 + x_4 \tan x_3)}{x_1} + 2\omega_e (x_4 \sin x_3 + x_6 \cos x_3) + \dfrac{F_2}{x_7} \\ \dfrac{-((x_4)^2 + (x_5)^2)}{x_1} - 2\omega_e x_5 \cos x_3 - x_1 (\omega_e \cos x_3)^2 + \dfrac{F_3}{x_7} \\ \dfrac{1}{g_0}\left(\dfrac{QC_T}{I_{sp_a}}\right) \end{pmatrix} \qquad \text{(Eq. 18)}$$

Using an assumption of constant zero bank angle, the following force equations in the vehicle LVLH frame result assuming an arc tangent definition over the range from -90 deg to +90 deg:

$$F = \begin{pmatrix} F_1 \\ F_2 \\ F_3 \end{pmatrix} = \begin{pmatrix} sign(v_1)\cos\psi(F_T \cos\gamma + F_N \sin\gamma) \\ sign(v_1)\sin\psi(F_T \cos\gamma + F_N \sin\gamma) \\ -F_T \sin\gamma + F_N \cos\gamma + F_g \end{pmatrix} \qquad \text{(Eq. 19)}$$

where $sign(v_1)$ has a value of 1 for $v_1 \geq 0$, and a value of -1 for $v_1 < 0$. Also note that only two force components remain in the body frame (no side force):

$$F_T = T\cos\alpha - D \qquad \text{(Eq. 20)}$$

$$F_N = -(T\sin\alpha + L) \qquad \text{(Eq. 21)}$$

Also, the following equations are used to relate flight angles to states:

$$\gamma = \tan^{-1}\left(\frac{-x_6}{\sqrt{(x_4)^2 + (x_5)^2}}\right) \qquad \text{(Eq. 22)}$$

$$\psi = \tan^{-1}\left(\frac{x_5}{x_4}\right) \qquad \text{(Eq. 23)}$$

The lift, drag, and engine thrust can be written in the following form involving coefficient functions specified in the example vehicle model data tables:

$$L = C_L Q S_{ref} \qquad \text{(Eq. 24)}$$

$$D = C_D Q S_{ref} \qquad \text{(Eq. 25)}$$

$$T = Q C_T \qquad \text{(Eq. 26)}$$

where:

$$v_f = \sqrt{(v_1)^2 + (v_2)^2 + (v_3)^2} \qquad \text{(Eq. 27)}$$

When using the example vehicle model data base, M_f and α are required, where v_f is used along with r in an atmosphere model to compute M_f. A determination of the value of α is made from the following relationship:

$$\alpha = \theta - \gamma \qquad \text{(Eq. 28)}$$

The gravity force acting on the vehicle can be written in the following form:

$$F_g = \frac{\mu_e x_7}{(x_1)^2} \qquad \text{(Eq. 29)}$$

Finally, the following equation is used to transform the throttle control on the propulsion to an unbounded control vector component. It is based on the assumption that $\Phi_a \geq 0$.

$$\Phi_a = (u_a)^2 \qquad \text{(Eq. 30)}$$

V.B.6.b. The Boundary Conditions

Initial Conditions: The initial conditions assumed for the example vehicle in the analysis demonstration are set immediately after horizontal takeoff. They correspond to due east launch from an equatorial location. Note that initial longitude (ν_0) has no effect on the problem and is therefore arbitrarily set at 0 deg.

$$x_0 = \begin{pmatrix} r_0 \\ \nu_0 \\ \mu_0 \\ v_{1_0} \\ v_{2_0} \\ v_{3_0} \\ m_0 \end{pmatrix} = \begin{pmatrix} 20,909,723\,ft \\ 0\,deg \\ 0\,deg \\ 0\,ft/s \\ 446.473\,ft/s \\ -6.46676\,ft/s \\ 297,382\,lb \end{pmatrix} \qquad \text{(Eq. 31)}$$

Target Atmospheric Exit Conditions: The target condition corresponds to atmospheric exit at 400,000 ft altitude (h) for a transfer orbit that has an apogee altitude of 100 NM and a perigee altitude of sea level. Assuming a near impulsive orbit change, a rocket burn of 184 ft/s is required at apogee to circularize the orbit. With an equatorial circular orbit as the objective, latitude and longitude are unconstrained at the target condition. Also, since equatorial launch to equatorial orbit is to be computed, the northerly velocity component (v_1) remains zero without application of a boundary condition. A target transfer orbit velocity is not a suitable forward integration cutoff condition since the air-breathing engine power drop that results from the decline in Q late in ascent combines with drag and gravity loss effects to produce a non-monotonic vehicle velocity history. Therefore the trajectory cutoff condition is specified in terms of an atmospheric exit altitude that will only be crossed once on the way to orbital apogee. This results in a forward integration cutoff represented as:

$$\Omega(\tau) = r - r_{targ} \qquad \text{(Eq. 32)}$$

The two remaining terminal time state boundary condition constraints are atmospheric exit target velocity and the radial component of the velocity.

$$\Psi = \begin{pmatrix} (v_2)^2 + (v_3)^2 - (v_D)^2 \\ v_3 - v_{3_D} \end{pmatrix} \qquad \text{(Eq. 33)}$$

The orbital parameters at atmospheric exit (assumed to be at $h = 400,000\,ft$ altitude) result in an inertial exit velocity of 25,645 ft/s and a heading angle (flight path angle in an inertial frame) of 0.958 deg (based on formulas found in Refs. 9-10). Horizontal and vertical velocity components are derived and the horizontal component is converted to a free stream value by including Earth rotation (ω_e) effects. The results are the following values of the atmospheric exit target conditions:

$$\begin{pmatrix} r_{targ} \\ v_D \\ v_{3_D} \end{pmatrix} = \begin{pmatrix} 21,309,723\,ft \\ 24,091.6\,ft/s \\ -429.1\,ft/s \end{pmatrix} \quad \text{(Eq. 34)}$$

V.B.6.c. Cost Function Specification

The terminal cost term ϕ is used to minimize the consumed fuel mass.

$$\phi = m_0 - m(\tau) \quad \text{(Eq. 35)}$$

The integral function L treats inequality constraints. In this application where dynamic pressure is constrained, L is a function only of states since dynamic pressure is a function of velocity states and density, and density is a function of r when using a standard atmosphere model.

$$\mathrm{L} = C_Q(Q - Q_D)^2 u_0[Q - Q_D] \quad \text{(Eq. 36)}$$

where:

$$Q = \frac{\rho(v_f)^2}{2} \quad \text{(Eq. 37)}$$

and where $u_0[Q - Q_D]$ is a unit step function that changes from zero to one at $Q = Q_D$.

V.B.6.d. Relevant Partial Derivatives

Boundary Condition Derivatives: The following equations are the required derivatives of the boundary condition functions.

$$\Omega_x = (1 \quad 0 \quad 0 \quad 0 \quad 0 \quad 0 \quad 0) \quad \text{(Eq. 38)}$$

$$\Psi_x = \begin{pmatrix} 0 & 0 & 0 & 0 & 2v_2 & 2v_3 & 0 \\ 0 & 0 & 0 & 0 & 0 & 1 & 0 \end{pmatrix} \quad \text{(Eq. 39)}$$

Cost Function Derivatives: The following equations are the derivatives of the cost functions J that are required:

$$\phi_x = (0 \quad 0 \quad 0 \quad 0 \quad 0 \quad 0 \quad -1) \quad \text{(Eq. 40)}$$

$\mathrm{L}_x = 0$ if $Q < Q_D$, and when $Q \geq Q_D$:

$$\mathrm{L}_x = 2K_Q(Q - Q_D)\frac{\partial Q}{\partial x} \quad \text{(Eq. 41)}$$

The Hamiltonian derivative with respect to controls can be expressed by the relationship $\mathrm{H}_u = \mathrm{L}_u + \lambda^T f_u$ which requires a partial of the integral cost function with respect to the control vector. For the functions of L selected in the example here, L_u has zero value.

State Equation Derivatives: The partials of the vehicle dynamics equation f are required. Because of the complexity of its specification, details are given in the Appendix A.

The partials of the dynamics equation f with respect to controls are required. Because of the complexity of its specification, details are given in Appendix B.

V.C. Analysis Demonstration Results with Phase II Model

The integrated trajectory/control analysis algorithm was further demonstrated using the phase II vehicle model. Incorporating the changes discussed previously, the example case spanned the entire atmospheric flight phase for a single-stage-to-orbit HSV. Details of the demonstration case that was accomplished and conclusions from resulting analysis follow.

V.C.1. Summary of Case Run

A near-fuel-optimal trajectory was determined for the phase II HSV model which spanned horizontal, equatorial takeoff to atmospheric exit (400,000 ft altitude) on the way to a 100 NM circular equatorial orbit. At atmospheric exit, apogee was set at 100 NM and perigee at sea level. Air breathing propulsion was active throughout flight, with its fuel/air equivalence ratio setting and the vehicle local vertical pitch attitude time histories determined by the trajectory/control optimization algorithm. The thrust coefficient and the functionally related specific impulse were calculated as functions of Mach number and equivalence ratio. Lift and drag forces of the airframe were calculated as functions of Mach number and angle of attack. Dynamic pressure was constrained to be near, or below 1000 psf.

V.C.2. Overview of Trajectory/Control Analysis Results

As was done for the previous analysis algorithm demonstration example, data for a number of variables were output for the case run using the phase II vehicle model. Included were all relevant state and control variables.

Altitude, Mach Number, and Dynamic Pressure

Figures 24 and 25 plot altitude and Mach number respectively. The altitude profile is monotonic, with a rapid climb at low speed, a much slower climb while accelerating through high Mach numbers, and finally a atmospheric pull out maneuver (starting around 2000 seconds) to go to the target orbit. The Mach number profile follows the trend of the altitude profile throughout atmospheric acceleration. However, due to temperature variations in the atmosphere model at extreme altitudes, the Mach profile peaks and then drops during atmospheric climb out. The dynamic pressure Q, is seen in figures 24 and 25 to reach the bound of 1000 psf within the rapid climb interval, around Mach 1.2. While the dynamic pressure bound is effective for the remainder of atmospheric acceleration, the change in propulsion system model at Mach 2 causes some transients in the dynamic pressure history around the bound for about 200 seconds (a period consistent with the dynamic pressure oscillation frequency seen in the phase I model analysis case). Finally, the dynamic pressure drops rapidly during atmospheric climb out of the vehicle.

Controls and Angle of Attack

The equivalence ratio control variable (phi) is plotted in figures 28 and 29, the local horizontal pitch attitude control variable (theta) is plotted in figures 30 and 31, and the resulting angle of attack (alpha - not a control variable in this case) is plotted in figures 32 and 32. Equivalence ratio undergoes rapid variations at low speed. It drops well below unity during subsonic acceleration after takeoff, then climbs to a peak near 1.9 during transonic acceleration. During high speed acceleration it gradually declines to near unity at Mach 5, and then very slowly declines to slightly below unity for the remainder of flight. The pitch angle has a sharp peak during the rapid low speed climb seen in figure 24. It then rapidly drops to about 5 degrees followed by a slow decline during high Mach number acceleration. It necessarily increases during atmospheric climb out to provide the aerodynamic lift necessary for the maneuver. The angle of attack starts at a

high value to get the lift necessary for takeoff, drops to a local minimum during transonic flight (keeping drag low when the drag coefficient is high), rises during early high Mach flight (up to Mach 10) and the declines as orbital speed is approached (since required lift drops to zero at orbital speed). The rate of decline in angle of attack is drastically decreased, however, as the aerodynamic climb out maneuver is initiated.

Flight Path Angle

Figures 34-36 plot the flight path angle (gamma) on various scales to illustrate a range of trends. A very sharp peak (45 deg) is seen to result from the low speed climb with the angle subsequently dropping off to a very small value (about 0.1 deg) above Mach 5 for the remainder of high Mach number acceleration. The flight path angle necessarily increases back to about 1 degree to provide the rapid altitude rise achieved during atmospheric climb out as seen in figure 24.

Acceleration, Thrust, and Velocity

Inertial acceleration is plotted in figures 37 and 38, air-breathing engine thrust is plotted in figures 39 and 40, and inertial velocity is plotted in figure 41. Acceleration drops in subsonic flight during takeoff, and climbs through the transonic region, with a jump at Mach 2 to a peak of 45 ft/sec^2 when the propulsion model is changed. A decline to about 10 ft/sec^2 occurs by Mach 10 which is then sustained until atmospheric climb out. While the thrust shows no real decline in the subsonic flight regime, it follows the trends in the acceleration profile in all other respects. The differences in the acceleration and thrust trends during subsonic flight can be attributed to the varying drag effects due to the angle of attack profile seen in figure 33 (drag is a function of Mach number and angle of attack). Inertial velocity climbs quickly during the high acceleration at low Mach numbers, climbs more slowly during the lower acceleration experienced at high Mach numbers, and experiences a gradual drop during atmospheric climb out due to an exchange of kinetic energy (speed) for potential energy (altitude).

Mass and Mass Flow

Figures 42-44 illustrate the mass and mass flow histories. During air-breathing acceleration, the mass follows a nearly linear decline (relatively constant mass flow) except at low speed when a peak in mass flow (and acceleration) occurs. A small jump in mass flow is seen at Mach 2 when the engine model changes.

V.C.3. Effects of Propulsion Model Discontinuity at Mach 2

The phase II vehicle model has two separate propulsion data bases. There is a low speed model applicable from takeoff to Mach 2 and a high speed model applicable from Mach 2 to orbital velocity. The transition between models results in a discontinuity in thrust coefficient and specific impulse at Mach 2. This in turn causes discontinuities in acceleration (figure 38), thrust force (figure 40), and mass flow (figure 44) at Mach 2.

The treatment of the propulsion system in the phase II vehicle model does not accommodate an analysis feature available in the integrated analysis algorithm (as documented in reference 1). That feature permits explicit treatment of the timing of propulsive discontinuities as performance optimization variables. However, the performance of the alternative engine modes must be modelled for overlapping operational ranges so that the optimum propulsive mode transition time and state can be determined as a function of those models and the vehicle aerodynamics (all the sources of vehicle forces). By contrast, the phase II vehicle model predetermines the transition as a particular state value (Mach 2 - a function of velocity and temperature).

Some transient effects appear in the near-fuel-optimal trajectory/control solution when using the phase II propulsion model. Angle of attack reverses its decline at Mach 2 and undergoes a small jump in desired value. The equivalence ratio starts a decline from the transonic peak at Mach 2. Also, the dynamic pressure magnitude passes through a cusp a Mach 2. Between Mach 1.5 and 2 the dynamic pressure declines from a local maximum slightly above 1000 psf. Between Mach 2 and 6 (spanning a flight time of about 200 seconds) the dynamic pressure undergoes

an erratic transient initiated with a sudden change in gradient at Mach 2. During the 200 second interval, dynamic pressure values remain a little below the 1000 psf bound. The correlation of the time of the dynamic pressure transient initiated at Mach 2 and the period of subsequent dynamic pressure oscillations at high Mach numbers is probably not coincidental.

V.C.4. A Look at Dynamic Pressure History Stability

An weakly divergent instability in the dynamic pressure was observed in the demonstration example using the phase I model, as plotted in figure 18. This behavior motivated a change in the defined control variable for the phase II vehicle model from angle of attack to local vertical pitch angle. Figure 45 provides a plot of the dynamic pressure history for the phase II model demonstration example that is on scales similar to figure 18. An oscillation still exists in the phase II model example, with a period remaining close 200 seconds (though somewhat variable). In the phase II example the oscillation seems to be near neutral stability rather than divergent. However, the presence of any significant oscillation adversely affects the convergence of the analysis algorithm to a near-fuel-optimal trajectory/control solution. The change of control variable made for the phase II model was helpful, but not fully effective at eliminating the undesired behavior. Future studies ought to consider alternatives to simple vehicle pitch orientation variables as controls in order to fully remove dynamic pressure oscillation effects.

V.C.5. Sensitivity of Solution Trajectories to the Propulsion Model

The character of HSV near-fuel-optimal trajectory solutions at hypersonic Mach numbers is sensitive to details of the vehicle propulsion model implementation. Close inspection of the second example vehicle propulsion model data suggests that small modeling differences such as alternative data interpolation strategies may be capable of causing substantial change in the high Mach number control history and flight profile while causing relatively small perturbation to the overall solution performance. Variations in the air-breathing propulsion throttle settings that in turn affect total time spent accelerating to orbital velocities are possible. Features peculiar to HSV dynamics models are at the root of these sensitivities. HSV acceleration in the high Mach regime results from the application of a thrust which is larger, but of the same order, as net vehicle drag. However, typically HSV models represent the propulsion system characteristics with sparsely populated data tables. The tables must be curve fit, and the resulting propulsion approximations must be differenced with the aerodynamics to produce a net force for the dynamics model.

Figure 23 plots specific impulse vs Mach number for a range of phi as curve fit for the second example vehicle model when operating in the high speed propulsion phase. Scrutiny of the plot near Mach 6 shows that comparatively little specific impulse is lost by increasing the equivalence ratio above 1.0, while comparatively large improvements in specific impulse are possible for the equivalence ratio below 1.0 at Mach numbers above 7. However, flying at low phi in the high Mach regime reduces acceleration, increases flight times, and results in higher cumulative drag losses. As a result, small disparities in the curve fit for thrust and drag model characteristics can have a much amplified relative impact on total performance gradients that determine near-fuel-optimal trajectories and control histories. If different curve fit approximations cause further reduction of specific impulse variation in the Mach 6 regime, then desired equivalence ratio will be increased. Also, slightly larger residuals of differenced thrust and drag estimates due to alternative curve fits will encourage lower phi and longer flight times in the high Mach regime.

V.D. Analysis Observations Affecting G&C Design

The demonstration cases of the integrated trajectory/control analysis methodology illustrate its power to identify important issues affecting HSV G&C system design. Some specific examples follow.

- Significant oscillation in the dynamic pressure profile can result from the use of vehicle longitudinal orientation angle related control variables. In the first demonstration case, use of angle of attack led to a slowly divergent oscillation in dynamic pressure and altitude as seen in figures 18 and 19. In the second demonstration case, the use of local horizontal pitch attitude as a control variable, instead of angle of attack, reduced the instability to persistent, somewhat chaotic oscillations as seen in figure 45. While the behavioral change in the second case was an improvement, it indicates that the appropriate control variable choice needs further consideration.
- The inclusion of elevon deflection histories in the first demonstration case highlights the limits on real control authority that may apply to these effectors. Figure 10 shows that for hundreds of seconds, nearly 17 degrees of elevon deflection is needed for vehicle longitudinal moment trim. Given that these effectors have a typical deflection limit of 20 degrees, very little authority remains for actual vehicle attitude control. Furthermore, large deflections of aerosurfaces over extended intervals can have significant adverse impact on vehicle payload capacity due to incremental drag effects.
- Significant rapid changes in vehicle angle of attack may be essential to efficient vehicle trajectory management. In both demonstration cases such variations in desired angle of attack are apparent. They appear between Mach 5 and 8 for the first case (see figure 9) and near Mach 5 in the second case (see figure 33). These desired variations set a lower bound on control system response times. A real vehicle design would also have to be responsive to disturbances due to wind effects and other atmospheric disturbances.

V.E. Progress Toward AIPS Requirements Specification

The HSV integrated trajectory and control analysis methodology developed under this task provides information that is essential to development of closed-loop G&C system design requirements. The demonstration winged-cone vehicle results provide enough trajectory management strategy and performance sensitivity information (as reviewed in this report and reference 1) to initiate development of a strawman G&C requirements specification. A complete G&C specification would permit characterization of a closed-loop G&C algorithm, including input/output processing rates and redundancy requirements. Completion of all these steps, to accommodate assessment of expected overall G&C related throughput and computational processing rates, is a mandatory part of the AIPS requirements specification [11].

VI. Conclusions

Air-breathing hypersonic vehicle designs demand complex integration of airframes and propulsion systems. As a result, there is a strong dependence between vehicle configuration details, the feasible mission performance, and trajectory management and control strategies. To assure that an overall vehicle design has a high probability of achieving mission objectives, it is essential to have a means to perform an early assessment of how specific vehicle designs and their guidance and control system characteristics interact.

A generic methodology to permit integrated trajectory/control analysis, including the effects of physically derived constraints, has been applied to the analysis of example air-breathing single-stage-to-orbit hypersonic vehicles. The resulting algorithm includes features that allow an assessment of the relative performance of alternative vehicles and/or subsystem technologies with respect to a single mathematically valid measure. Also, since the available vehicle models used to represent aerodynamics and propulsion characteristics exist as multidimensional tabulated data bases, a cubic spline data smoothing routine has been included in the software package to process the information. The splines assure good numerical behavior of the analysis algorithm.

The methodology has been demonstrated using two vehicle dynamics models. The cases were selected to evaluate the power of the algorithm to derive information of critical importance to developers of guidance and control systems. Based on a winged-cone vehicle concept both models were combined with the algorithm including representations of all relevant partial derivatives. Use of the trajectory/control tools with the vehicle models produced near-minimum-fuel trajectories and desired control strategies from takeoff to near-orbit targets. Throttle setting limits and a dynamic pressure inequality constraint of 1000 psf were explicitly included in the demonstrations. The first case, using an early propulsion model, considered flight on a polar orbit track up to 25,000 ft/s relative air speed. It included the aerodynamic effects of using elevons to maintain longitudinal trim throughout flight. The second case, using an improved propulsion model but removing the elevon aerodynamics, aimed for a atmospheric exit at 400,000 ft on track to a 100 NM circular orbit. The following list summarizes some of the most significant conclusions:

- The selection of control variables can significantly affect the stability and performance of the analysis algorithm. Use of angle of attack can induce dynamic pressure/altitude instability during convergence to a desired reference trajectory. Replacement of angle of attack with vehicle local vertical pitch attitude eliminates the instability, but retains some undesired oscillations in the dynamic pressure profile. Additional investigation of suitable control variables is warranted.
- Small inconsistencies in propulsion model features and/or discontinuities in the propulsion models that are not explicitly treated as optimization parameters can introduce transients in the vehicle dynamics that adversely affect analysis algorithm performance.
- Aerosurface effectors can have significant impact on vehicle drag losses and limited actual control authority after accounting for deflection required to trim vehicle moments. As a result, design and placement of aerosurfaces needed for vehicle attitude control cannot be separated from the overall hypersonic vehicle design integration problem.
- A characteristic of all air-breathing hypersonic vehicle models is a large vehicle drag term as compared to thrust throughout hypersonic flight. This phenomenon was considered in combination with a close inspection of the curve fitted second example vehicle model propulsion data. The results suggest that small model changes, such as those resulting from alternative curve fit strategies for sparse tabulated model data, may induce significant differences in analysis algorithm solutions.

The demonstration cases provided much information about the analysis methodology capabilities and limitations as well as insight into key guidance and control system design issues. If existing extensions of the analysis methodology are applied, important physical effects not considered in the demonstration cases can be treated, such as accommodating thermal constraints and determining efficient propulsive mode phasing. These extensions would provide additional important input into air-breathing hypersonic vehicle guidance and control design requirements.

VII. References

[1] Philip D. Hattis and Harvey L. Malchow, "Air-Breathing Hypersonic Vehicle Guidance and Control Studies; An Integrated Trajectory/Control Analysis Methodology: Phase I", NASA Contractor Report 187623, September 1991.

[2] Hattis, Philip D., "An Optimal Design Methodology for a Class of Air-Breathing Launch Vehicles", Doctor of Philosophy Thesis, Massachusetts Institute of Technology, June 1980.

[3] Hattis, Philip D., "Optimal Air-Breathing Launch Vehicle Design", **Journal of Guidance and Control**, Vol. 4, No. 5, Sept. - Oct. 1981, pp. 543-550.

[4] National Aerospace Plane Configuration and Trajectory Assessment, C. S. Draper Laboratory Fiscal Year 89 IR&D Technical Plan, Report CSDL-R-2087, Project Number 236.

[5] Adams, Neil J. and Philip D. Hattis, "An Integrated Configuration and Control Analysis Technique for Hypersonic Vehicles", presented at the 1989 American Control Conference, Pittsburgh, Pennsylvania, June 21-23, 1989, pp. 1105-1110 of the proceedings.

[6] John E. Shaughnessy, S. Zane Pinckney, John D. McMinn, Christopher I. Cruz, and Marie-Louise Kelley, "Hypersonic Vehicle Simulation Model: Winged-Cone Configuration", NASA TM 102610, November 1990.

[7] Lawrence H. Stein, Malcolm L. Matthews, and Joel W. Frenk, "STOP - A Computer Program for Supersonic Transport Trajectory Optimization", Final Report, Boeing Aerospace Group, Seattle, Washington, January 1967.

[8] A.E. Bryson and W.F. Denham, "A Steepest-Ascent Method for Solving Optimum Programming Problems", **Journal of Applied Mechanics**, June 1962, pp. 247-257.

[9] Richard H. Battin, "An Introduction to the Mathematics and Methods of Astrodynamics", American Institute of Aeronautics and Astronautics, Inc., New York, 1987.

[10] William Tyrrell Thomson, "Introduction to Space Dynamics", John Wiley & Sons, New York, 1961.

[11] J.H. Lala, R.E. Harper, K.R. Jaskowiak, G. Rosch, L.S. Alger, A.L. Schor, "Advanced Information Processing System for Advanced Launch System: Avionics Architecture Synthesis", NASA CR-187554, 1991.

Appendix A
Partial Derivatives for the Example Model with Respect to States

The matrix f_x for the example application is too large to print as a single equation, so it is specified here on a column by column basis. The equations for f_x are simplified by the knowledge that the following derivatives have zero value: $\frac{\partial Q}{\partial v}; \frac{\partial M_f}{\partial v}; \frac{\partial Q}{\partial \mu}; \frac{\partial M_f}{\partial \mu}; \frac{\partial Q}{\partial m}; \frac{\partial M_f}{\partial m}$. Simplifications are also made by utilizing the knowledge that M_f is a function only of r and v_f.

$$\frac{\partial f}{\partial x_1} = \frac{\partial f}{\partial r} = \begin{pmatrix} 0 \\ \frac{-x_5}{(x_1)^2 \cos x_3} \\ \frac{-x_4}{(x_1)^2} \\ \frac{(x_5)^2 \tan x_3 - x_4 x_6}{(x_1)^2} - \frac{(\omega_e)^2 \sin 2x_3}{2} + \frac{1}{x_7}\frac{\partial F_1}{\partial x_1} \\ \frac{-x_5(x_6 + x_4 \tan x_3)}{(x_1)^2} + \frac{1}{x_7}\frac{\partial F_2}{\partial x_1} \\ \frac{(x_4)^2 + (x_5)^2}{(x_1)^2} - (\omega_e \cos x_3)^2 + \frac{1}{x_7}\frac{\partial F_3}{\partial x_1} \\ \frac{1}{g_0}\left(\frac{C_T}{I_{sp_a}}\frac{\partial Q}{\partial x_1} + \left(\frac{Q}{I_{sp_a}}\frac{\partial C_T}{\partial M_f} - \frac{QC_T}{(I_{sp_a})^2}\frac{\partial I_{sp_a}}{\partial M_f} \right)\frac{\partial M_f}{\partial x_1} \right) \end{pmatrix} \quad \text{(Eq. A.1)}$$

$$\frac{\partial f}{\partial x_2} = \frac{\partial f}{\partial v} = \begin{pmatrix} 0 \\ 0 \\ 0 \\ \frac{1}{x_7}\frac{\partial F_1}{\partial x_2} \\ \frac{1}{x_7}\frac{\partial F_2}{\partial x_2} \\ \frac{1}{x_7}\frac{\partial F_3}{\partial x_2} \\ 0 \end{pmatrix} \quad \text{(Eq. A.2)}$$

$$\frac{\partial f}{\partial x_3} = \frac{\partial f}{\partial \mu} = \begin{pmatrix} 0 \\ \dfrac{x_5 \sin x_3}{x_1 (\cos x_3)^2} \\ 0 \\ \dfrac{-(x_5)^2}{x_1 (\cos x_3)^2} - 2\omega_e x_5 \cos x_3 - x_1 (\omega_e)^2 \cos 2x_3 + \dfrac{1}{x_7}\dfrac{\partial F_1}{\partial x_3} \\ \dfrac{x_5 x_4}{x_1 (\cos x_3)^2} + 2\omega_e (x_4 \cos x_3 - x_6 \sin x_3) + \dfrac{1}{x_7}\dfrac{\partial F_2}{\partial x_3} \\ 2\omega_e x_5 \sin x_3 + x_1 (\omega_e)^2 \sin 2x_3 + \dfrac{1}{x_7}\dfrac{\partial F_3}{\partial x_3} \\ 0 \end{pmatrix} \qquad \text{(Eq. A.3)}$$

$$\frac{\partial f}{\partial x_4} = \frac{\partial f}{\partial v_1} = \begin{pmatrix} 0 \\ 0 \\ \dfrac{1}{x_1} \\ \dfrac{x_6}{x_1} + \dfrac{1}{x_7}\dfrac{\partial F_1}{\partial x_4} \\ \dfrac{x_5 \tan x_3}{x_1} + 2\omega_e \sin x_3 + \dfrac{1}{x_7}\dfrac{\partial F_2}{\partial x_4} \\ -\dfrac{2x_4}{x_1} + \dfrac{1}{x_7}\dfrac{\partial F_3}{\partial x_4} \\ \dfrac{1}{g_0}\left(\dfrac{C_T}{I_{sp_a}}\dfrac{\partial Q}{\partial x_4} + \left(\dfrac{Q}{I_{sp_a}}\dfrac{\partial C_T}{\partial M_f} - \dfrac{QC_T}{(I_{sp_a})^2}\dfrac{\partial I_{sp_a}}{\partial M_f} \right)\dfrac{\partial M_f}{\partial x_4} \right) \end{pmatrix} \qquad \text{(Eq. A.4)}$$

$$\frac{\partial f}{\partial x_5} = \frac{\partial f}{\partial v_2} = \begin{pmatrix} 0 \\ \dfrac{1}{x_1 \cos x_3} \\ 0 \\ -\dfrac{2x_5 \tan x_3}{x_1} - 2\omega_e \sin x_3 + \dfrac{1}{x_7}\dfrac{\partial F_1}{\partial x_5} \\ \dfrac{x_6 + x_4 \tan x_3}{x_1} + \dfrac{1}{x_7}\dfrac{\partial F_2}{\partial x_5} \\ -\dfrac{2x_5}{x_1} - 2\omega_e \cos x_3 + \dfrac{1}{x_7}\dfrac{\partial F_3}{\partial x_5} \\ \dfrac{1}{g_0}\left(\dfrac{C_T}{I_{sp_a}}\dfrac{\partial Q}{\partial x_5} + \left(\dfrac{Q}{I_{sp_a}}\dfrac{\partial C_T}{\partial M_f} - \dfrac{QC_T}{(I_{sp_a})^2}\dfrac{\partial I_{sp_a}}{\partial M_f} \right)\dfrac{\partial M_f}{\partial x_5} \right) \end{pmatrix} \qquad \text{(Eq. A.5)}$$

$$\frac{\partial f}{\partial x_6} = \frac{\partial f}{\partial v_3} = \begin{pmatrix} -1 \\ 0 \\ 0 \\ \dfrac{x_4}{x_1} + \dfrac{1}{x_7}\dfrac{\partial F_1}{\partial x_6} \\ \dfrac{x_5}{x_1} + 2\omega_e \cos x_3 + \dfrac{1}{x_7}\dfrac{\partial F_2}{\partial x_6} \\ \dfrac{1}{x_7}\dfrac{\partial F_3}{\partial x_6} \\ \dfrac{1}{g_0}\left(\dfrac{C_T}{I_{sp_a}}\dfrac{\partial Q}{\partial x_6} + \left(\dfrac{Q}{I_{sp_a}}\dfrac{\partial C_T}{\partial M_f} - \dfrac{QC_T}{(I_{sp_a})^2}\dfrac{\partial I_{sp_a}}{\partial M_f}\right)\dfrac{\partial M_f}{\partial x_6}\right) \end{pmatrix} \qquad \text{(Eq. A.6)}$$

$$\frac{\partial f}{\partial x_7} = \frac{\partial f}{\partial m} = \begin{pmatrix} 0 \\ 0 \\ 0 \\ \dfrac{1}{x_7}\dfrac{\partial F_1}{\partial x_7} - \dfrac{F_1}{(x_7)^2} \\ \dfrac{1}{x_7}\dfrac{\partial F_2}{\partial x_7} - \dfrac{F_2}{(x_7)^2} \\ \dfrac{1}{x_7}\dfrac{\partial F_3}{\partial x_7} - \dfrac{F_3}{(x_7)^2} \\ 0 \end{pmatrix} \qquad \text{(Eq. A.7)}$$

where:

$$\frac{\partial F_1}{\partial x} = sign\psi[-\sin\psi(F_T\cos\gamma + F_N\sin\gamma)\frac{\partial\psi}{\partial x} + \cos\psi\left(\frac{\partial F_T}{\partial x}\cos\gamma + \frac{\partial F_N}{\partial x}\sin\gamma\right) + \cos\psi\frac{\partial\gamma}{\partial x}(-F_T\sin\gamma + F_N\cos\gamma)] \qquad \text{(Eq. A.8)}$$

$$\frac{\partial F_2}{\partial x} = sign\psi[\cos\psi(F_T\cos\gamma + F_N\sin\gamma)\frac{\partial\psi}{\partial x} + \sin\psi\left(\frac{\partial F_T}{\partial x}\cos\gamma + \frac{\partial F_N}{\partial x}\sin\gamma\right) + \sin\psi\frac{\partial\gamma}{\partial x}(-F_T\sin\gamma + F_N\cos\gamma)] \qquad \text{(Eq. A.9)}$$

$$\frac{\partial F_3}{\partial x} = -\frac{\partial F_T}{\partial x}\sin\gamma + \frac{\partial F_N}{\partial x}\cos\gamma + \frac{\partial F_G}{\partial x} - \frac{\partial\gamma}{\partial x}(F_T\cos\gamma + F_N\sin\gamma) \qquad \text{(Eq. A.10)}$$

$$\frac{\partial\psi}{\partial x} = \begin{pmatrix} 0 & 0 & 0 & \dfrac{-x_5}{(x_4)^2 + (x_5)^2} & \dfrac{x_4}{(x_4)^2 + (x_5)^2} & 0 & 0 \end{pmatrix} \qquad \text{(Eq. A.11)}$$

$$\frac{\partial F_T}{\partial x} = \frac{\partial T}{\partial x}\cos\alpha - (T\sin\alpha)\frac{\partial \alpha}{\partial x} - \frac{\partial D}{\partial x} \quad \text{(Eq. A.12)}$$

$$\frac{\partial F_N}{\partial x} = -\frac{\partial T}{\partial x}\sin\alpha - (T\cos\alpha)\frac{\partial \alpha}{\partial x} - \frac{\partial L}{\partial x} \quad \text{(Eq. A.13)}$$

$$\left(\frac{\partial \gamma}{\partial x}\right)^T = \begin{pmatrix} 0 \\ 0 \\ 0 \\ \dfrac{x_4 x_6}{(v_f)^2\sqrt{(x_4)^2+(x_5)^2}} \\ \dfrac{x_5 x_6}{(v_f)^2\sqrt{(x_4)^2+(x_5)^2}} \\ \dfrac{-\sqrt{(x_4)^2+(x_5)^2}}{(v_f)^2} \\ 0 \end{pmatrix} \quad \text{(Eq. A.14)}$$

$$\frac{\partial F_g}{\partial x} = \begin{pmatrix} \dfrac{-2\mu_e x_7}{(x_1)^3} & 0 & 0 & 0 & 0 & 0 & \dfrac{\mu_e}{(x_1)^2} \end{pmatrix} \quad \text{(Eq. A.15)}$$

$$\frac{\partial D}{\partial x} = QS_{ref}\frac{\partial C_D}{\partial x} + C_D S_{ref}\frac{\partial Q}{\partial x} \quad \text{(Eq. A.16)}$$

$$\frac{\partial L}{\partial x} = QS_{ref}\frac{\partial C_L}{\partial x} + C_L S_{ref}\frac{\partial Q}{\partial x} \quad \text{(Eq. A.17)}$$

$$\frac{\partial T}{\partial x} = Q\frac{\partial C_T}{\partial x} + C_T\frac{\partial Q}{\partial x} \quad \text{(Eq. A.18)}$$

$$\frac{\partial \alpha}{\partial x} = -\left(\frac{\partial \gamma}{\partial x}\right) \quad \text{(Eq. A.19)}$$

$$\frac{\partial C_D}{\partial x} = \frac{\partial C_D}{\partial M_f}\frac{\partial M_f}{\partial x} + \frac{\partial C_D}{\partial \alpha}\frac{\partial \alpha}{\partial x} \quad \text{(Eq. A.20)}$$

$$\frac{\partial C_L}{\partial x} = \frac{\partial C_L}{\partial M_f}\frac{\partial M_f}{\partial x} + \frac{\partial C_L}{\partial \alpha}\frac{\partial \alpha}{\partial x} \quad \text{(Eq. A.21)}$$

$$\frac{\partial C_T}{\partial x} = \frac{\partial C_T}{\partial M_f}\frac{\partial M_f}{\partial x} \qquad \text{(Eq. A.22)}$$

$$M_f = \frac{v_f}{a} \qquad \text{(Eq. A.23)}$$

$$\frac{\partial M_f}{\partial x} = \left(\frac{-v_f}{a^2}\frac{\partial a}{\partial r} \quad 0 \quad 0 \quad \frac{v_1}{a v_f} \quad \frac{v_2}{a v_f} \quad \frac{v_3}{a v_f} \quad 0 \right) \qquad \text{(Eq. A.24)}$$

To complete the evaluation of f_x, the following partial derivatives are derived from the example vehicle model data tables: $\frac{\partial C_D}{\partial M_f}; \frac{\partial C_D}{\partial \alpha}; \frac{\partial C_L}{\partial M_f}; \frac{\partial C_L}{\partial \alpha}; \frac{\partial C_T}{\partial M_f}; \frac{\partial I_{sp_a}}{\partial M_f}$. Also a and $\frac{\partial a}{\partial r}$ are derived from a standard atmosphere model.

Appendix B
Partial Derivatives for the Example Model with Respect to Controls

All the equations required to compute the matrix f_u for the example application are derived below.

$$f_u = \begin{pmatrix} 0 & 0 \\ 0 & 0 \\ 0 & 0 \\ \frac{1}{x_7}\left(\frac{\partial F_1}{\partial u_1}\right) & \frac{1}{x_7}\left(\frac{\partial F_1}{\partial u_2}\right) \\ \frac{1}{x_7}\left(\frac{\partial F_2}{\partial u_1}\right) & \frac{1}{x_7}\left(\frac{\partial F_2}{\partial u_2}\right) \\ \frac{1}{x_7}\left(\frac{\partial F_3}{\partial u_1}\right) & \frac{1}{x_7}\left(\frac{\partial F_3}{\partial u_2}\right) \\ \frac{Q}{g_0}\frac{\partial}{\partial u_1}\left(\frac{C_T}{I_{sp_a}}\right) & 0 \end{pmatrix} \quad \text{(Eq. B.1)}$$

where:

$$\frac{\partial F_1}{\partial u_i} = sign\,\psi \cos\psi \left(\frac{\partial F_T}{\partial u_i}\cos\gamma + \frac{\partial F_N}{\partial u_i}\sin\gamma\right) \quad \text{(Eq. B.2)}$$

$$\frac{\partial F_2}{\partial u_i} = sign\,\psi \sin\psi \left(\frac{\partial F_T}{\partial u_i}\cos\gamma + \frac{\partial F_N}{\partial u_i}\sin\gamma\right) \quad \text{(Eq. B.3)}$$

$$\frac{\partial F_3}{\partial u_i} = -\frac{\partial F_T}{\partial u_i}\sin\gamma + \frac{\partial F_N}{\partial u_i}\cos\gamma \quad \text{(Eq. B.4)}$$

$$\frac{\partial}{\partial u_1}\left(\frac{C_T}{I_{sp_a}}\right) = \frac{2u_a}{I_{sp_a}}\left(\frac{\partial C_T}{\partial \Phi_a} - \frac{C_T}{I_{sp_a}}\frac{\partial I_{sp_a}}{\partial \Phi_a}\right) \quad \text{(Eq. B.5)}$$

$$\frac{\partial F_T}{\partial u_i} = \frac{\partial T}{\partial u_i}\cos\alpha - T\sin\alpha\frac{\partial \alpha}{\partial u_i} - \frac{\partial D}{\partial u_i} \quad \text{(Eq. B.6)}$$

$$\frac{\partial F_N}{\partial u_i} = -\left(\frac{\partial T}{\partial u_i}\sin\alpha + T\cos\alpha\frac{\partial \alpha}{\partial u_i} + \frac{\partial L}{\partial u_i}\right) \quad \text{(Eq. B.7)}$$

$$\frac{\partial \alpha}{\partial u} = (0 \quad 1) \qquad \text{(Eq. B.8)}$$

$$\frac{\partial D}{\partial u} = \left(0 \quad QS_{ref}\frac{\partial C_D}{\partial u_2}\right) \qquad \text{(Eq. B.9)}$$

$$\frac{\partial L}{\partial u} = \left(0 \quad QS_{ref}\frac{\partial C_L}{\partial u_2}\right) \qquad \text{(Eq. B.10)}$$

$$\frac{\partial T}{\partial u} = \left(2Qu_1\frac{\partial C_T}{\partial \Phi_a} \quad 0\right) \qquad \text{(Eq. B.11)}$$

Also:

$$\frac{\partial C_D}{\partial u_2} = \frac{\partial C_D}{\partial \alpha}\frac{\partial \alpha}{\partial u_2} \qquad \text{(Eq. B.12)}$$

$$\frac{\partial C_L}{\partial u_2} = \frac{\partial C_L}{\partial \alpha}\frac{\partial \alpha}{\partial u_2} \qquad \text{(Eq. B.13)}$$

To complete the evaluation of f_u, the following partial derivatives are derived from the example vehicle model data tables: $\frac{\partial C_T}{\partial \Phi_a}; \frac{\partial I_{sp_a}}{\partial \Phi_a}; \frac{\partial C_D}{\partial \alpha}; \frac{\partial C_L}{\partial \alpha}$.

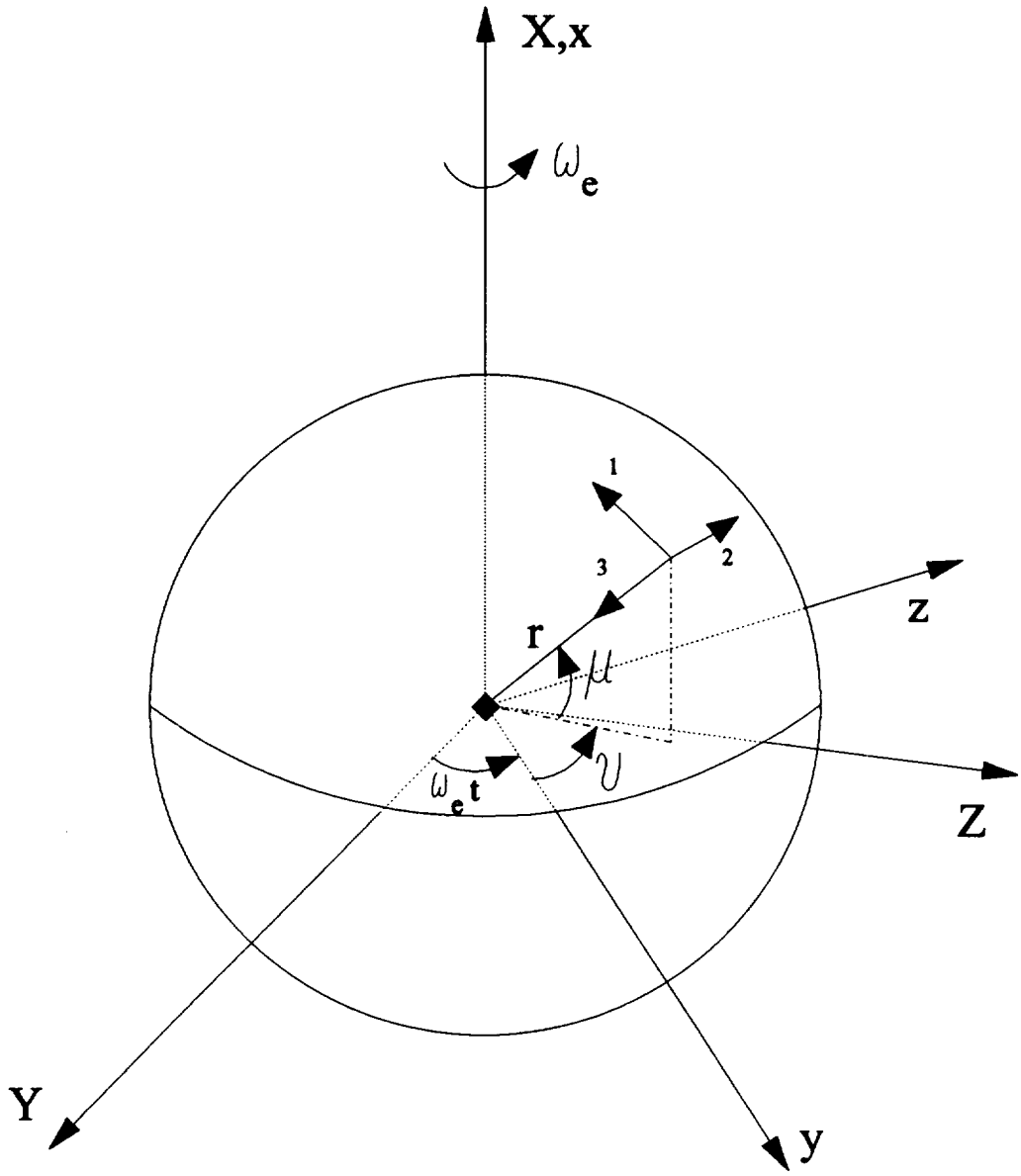

X-Y-Z:	Earth centered inertial frame
x-y-z:	Earth fixed frame (rotates with Earth)
1-2-3:	Vehicle fixed LVLH frame

Figure 1. Coordinate systems for dynamics equations

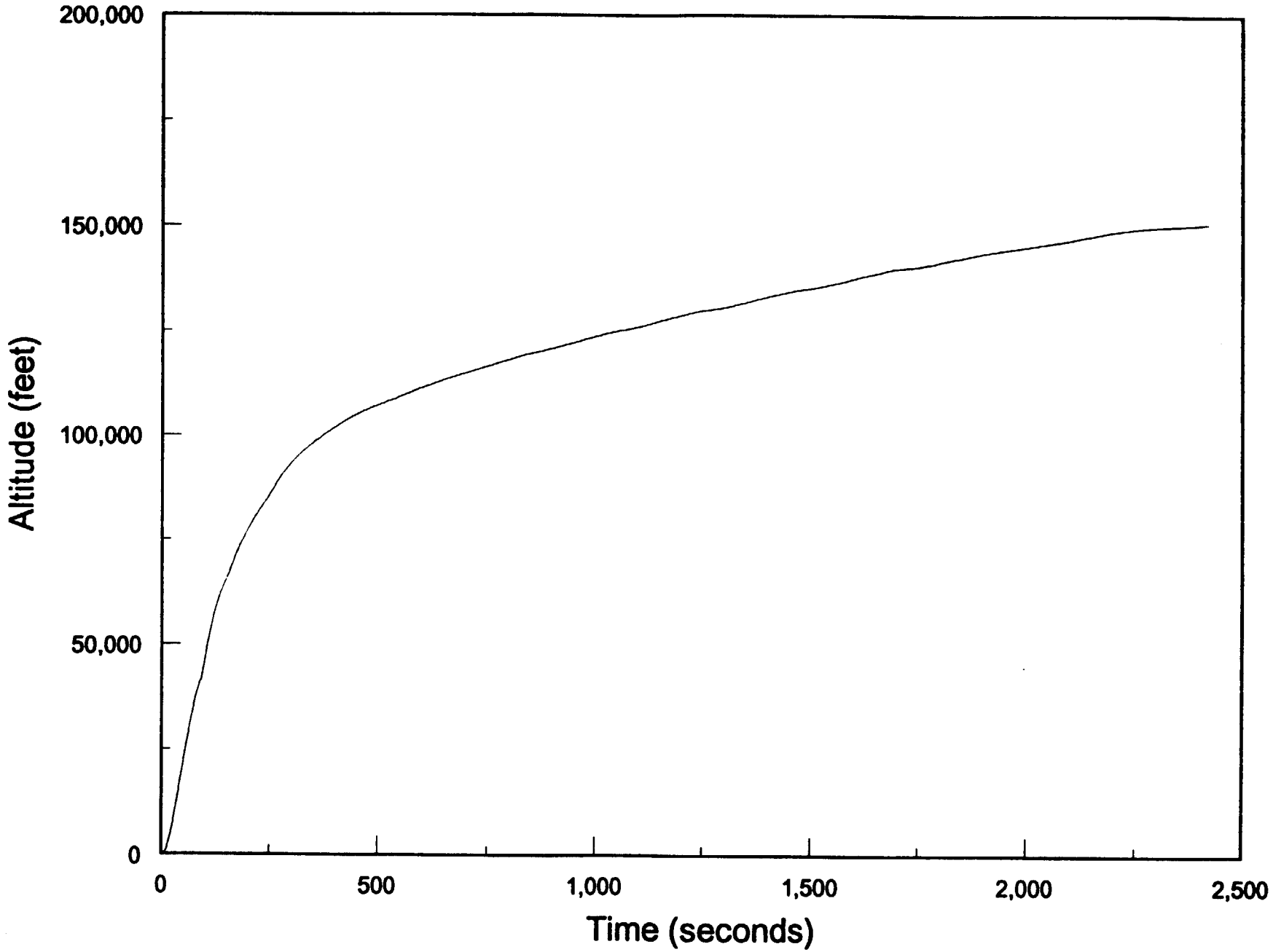

Figure 2. Altitude vs time - phase I model

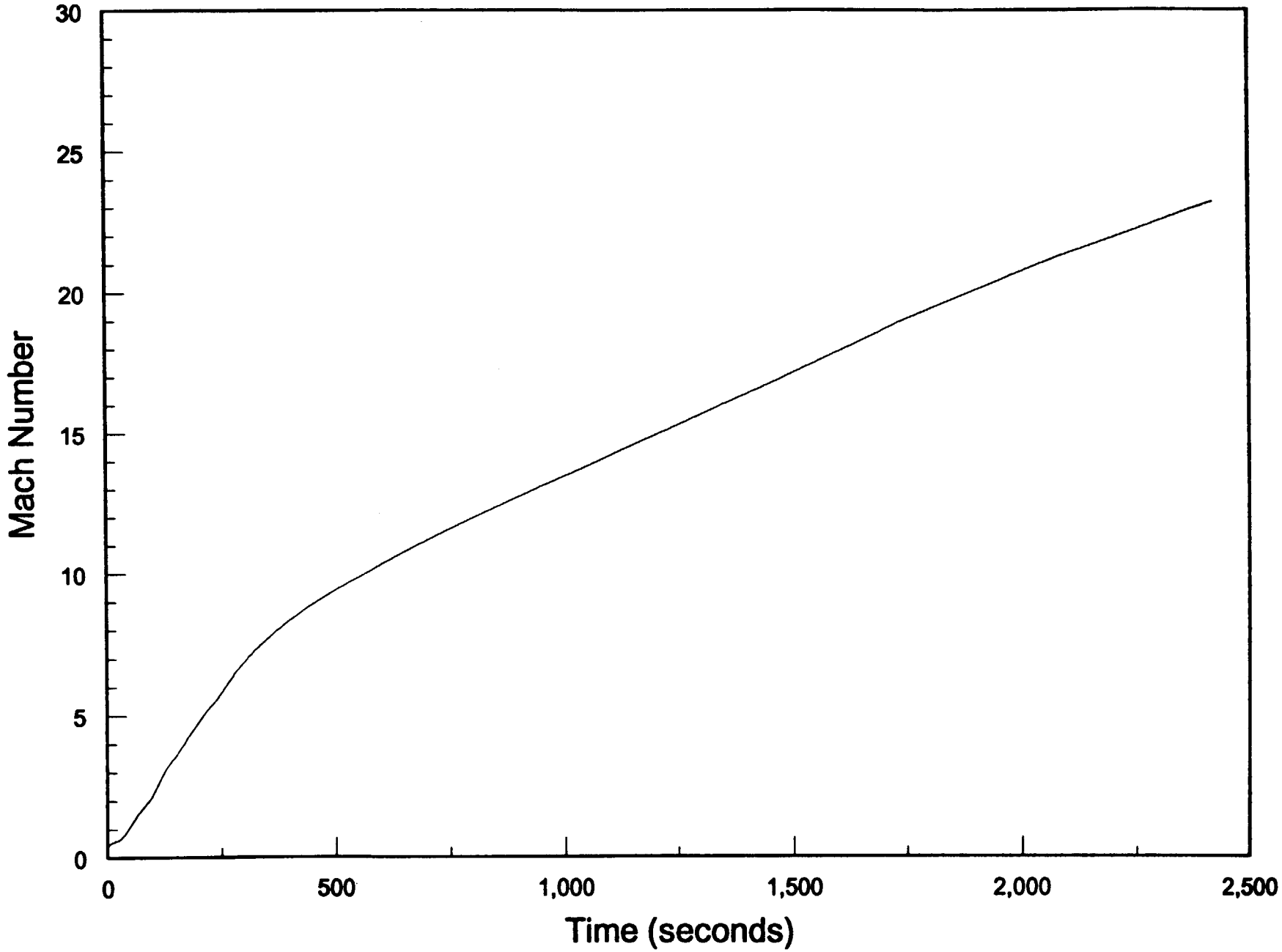

Figure 3. Mach number vs time - phase I model

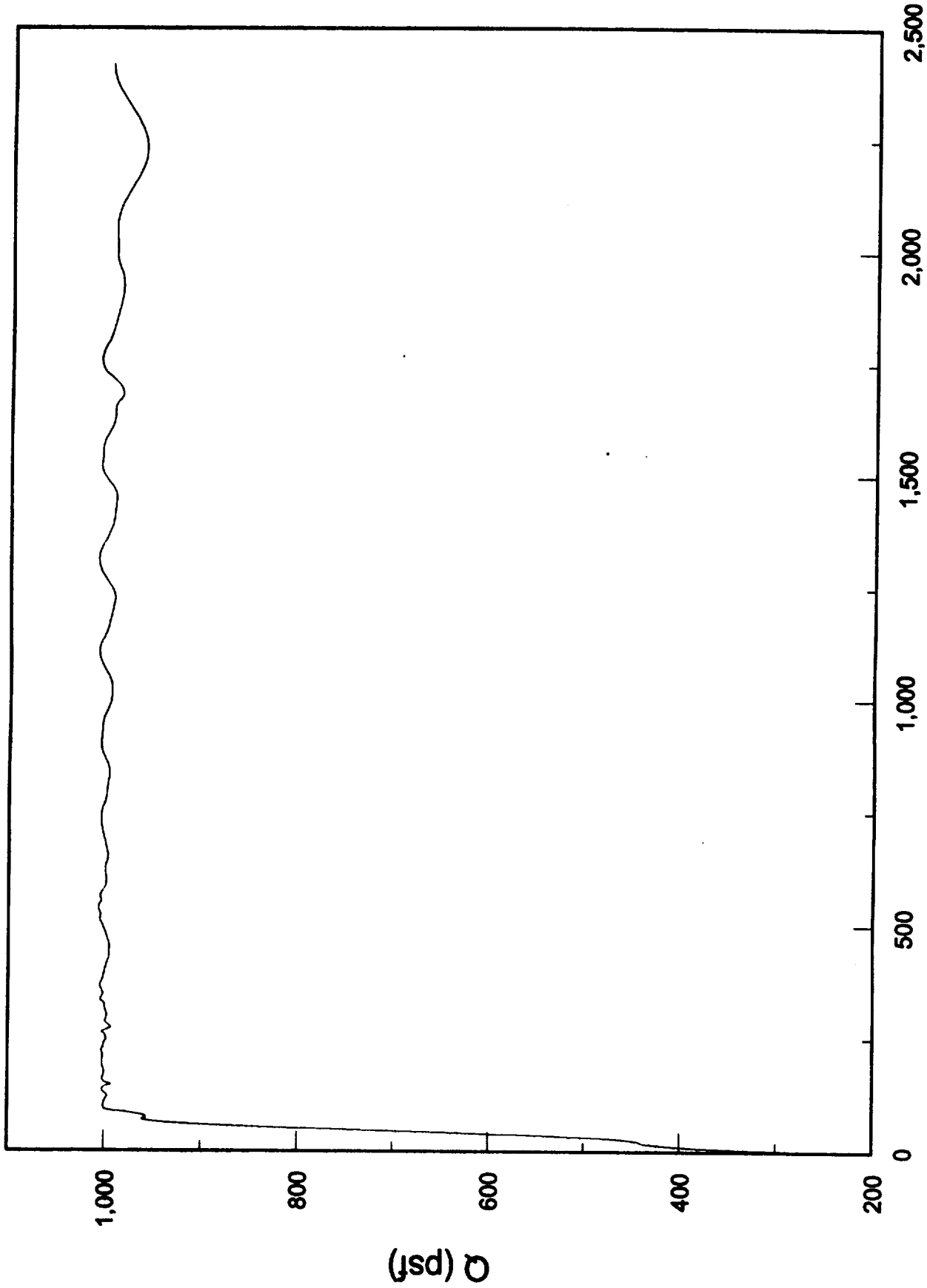

Figure 4. Q vs time - phase I model

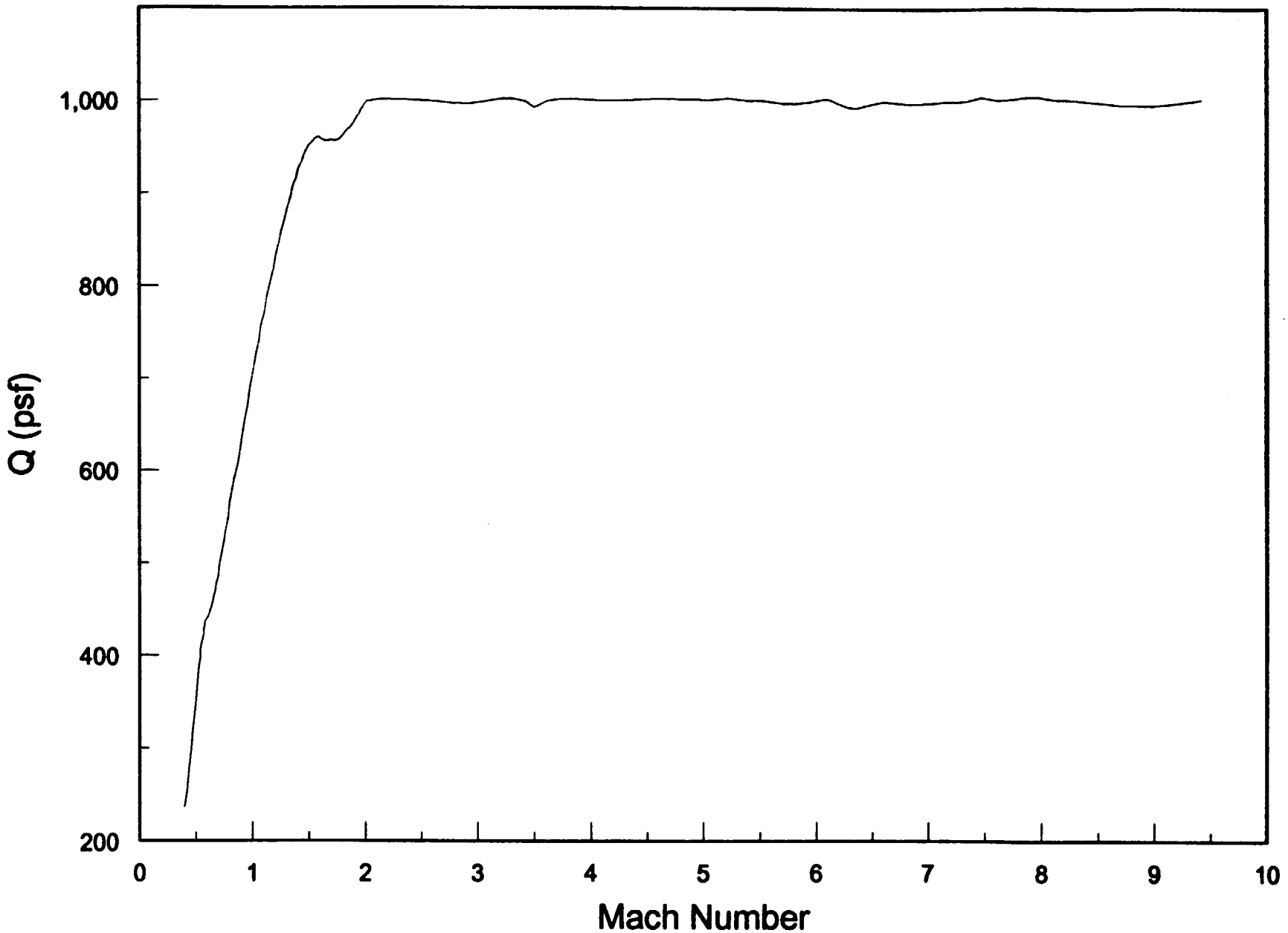

Figure 5. Q vs Mach number - phase I model
First 500 seconds of flight

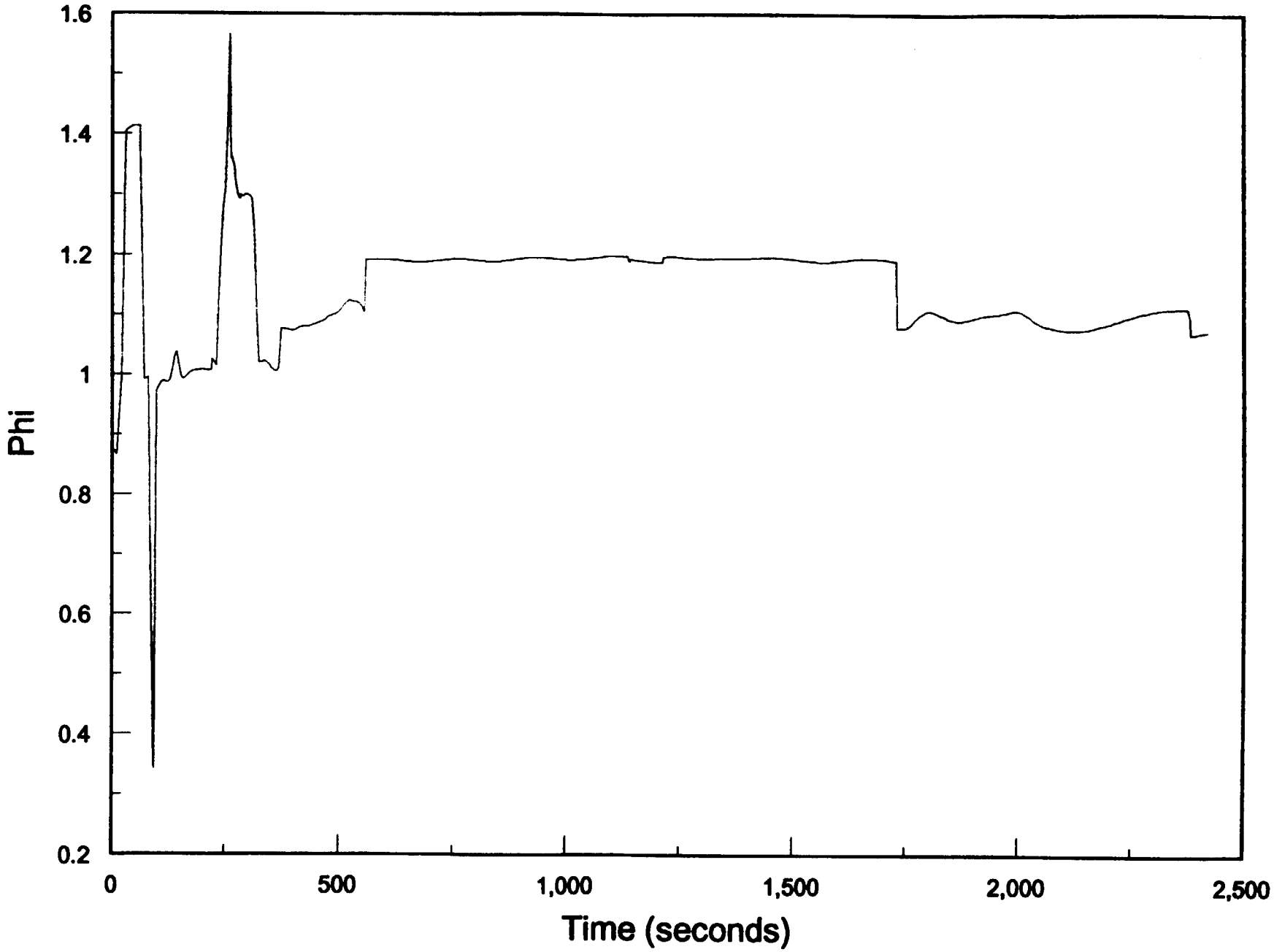

Figure 6. Phi vs time - phase I model

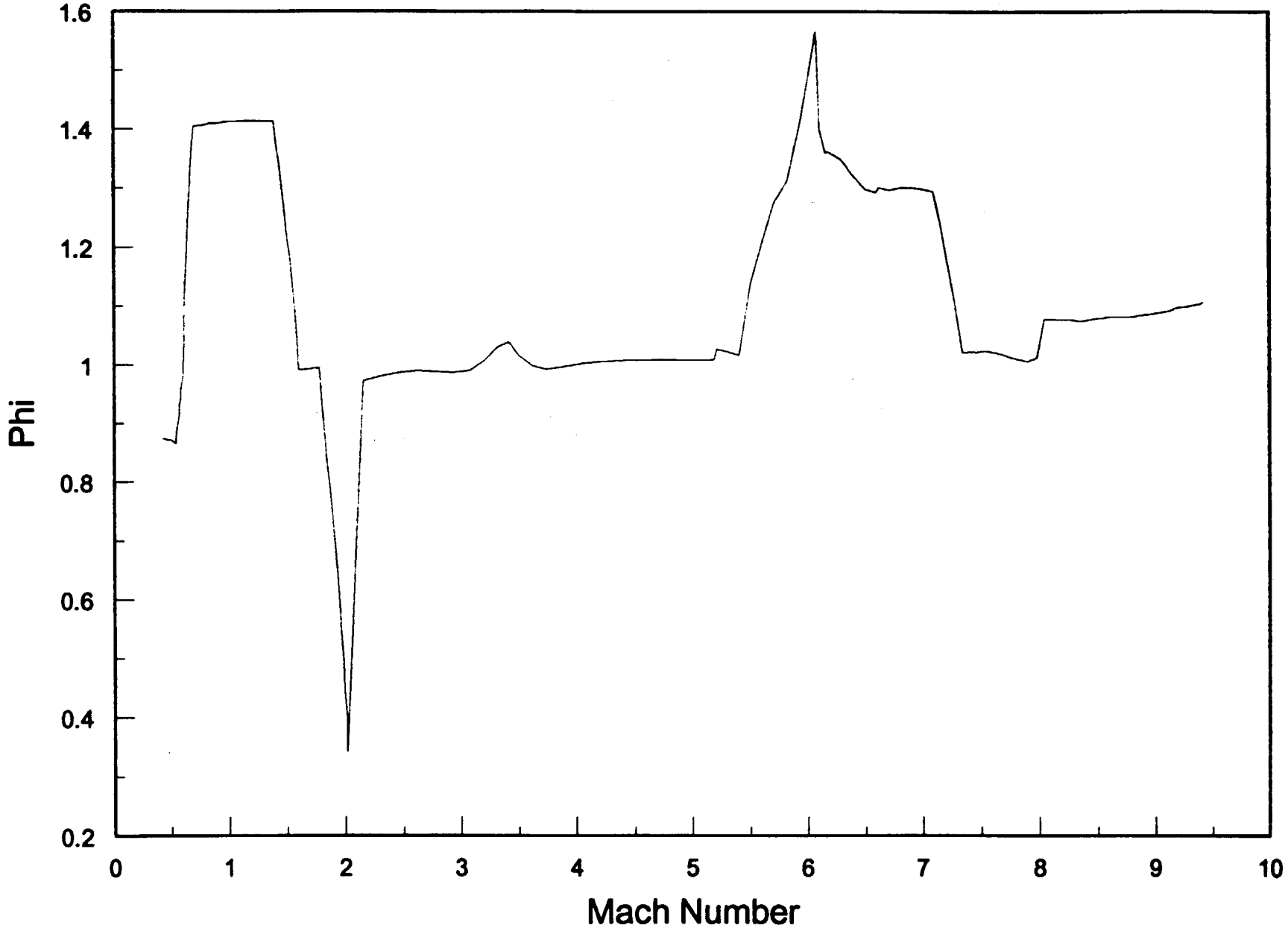

Figure 7. Phi vs Mach number - phase I model
First 500 seconds of flight

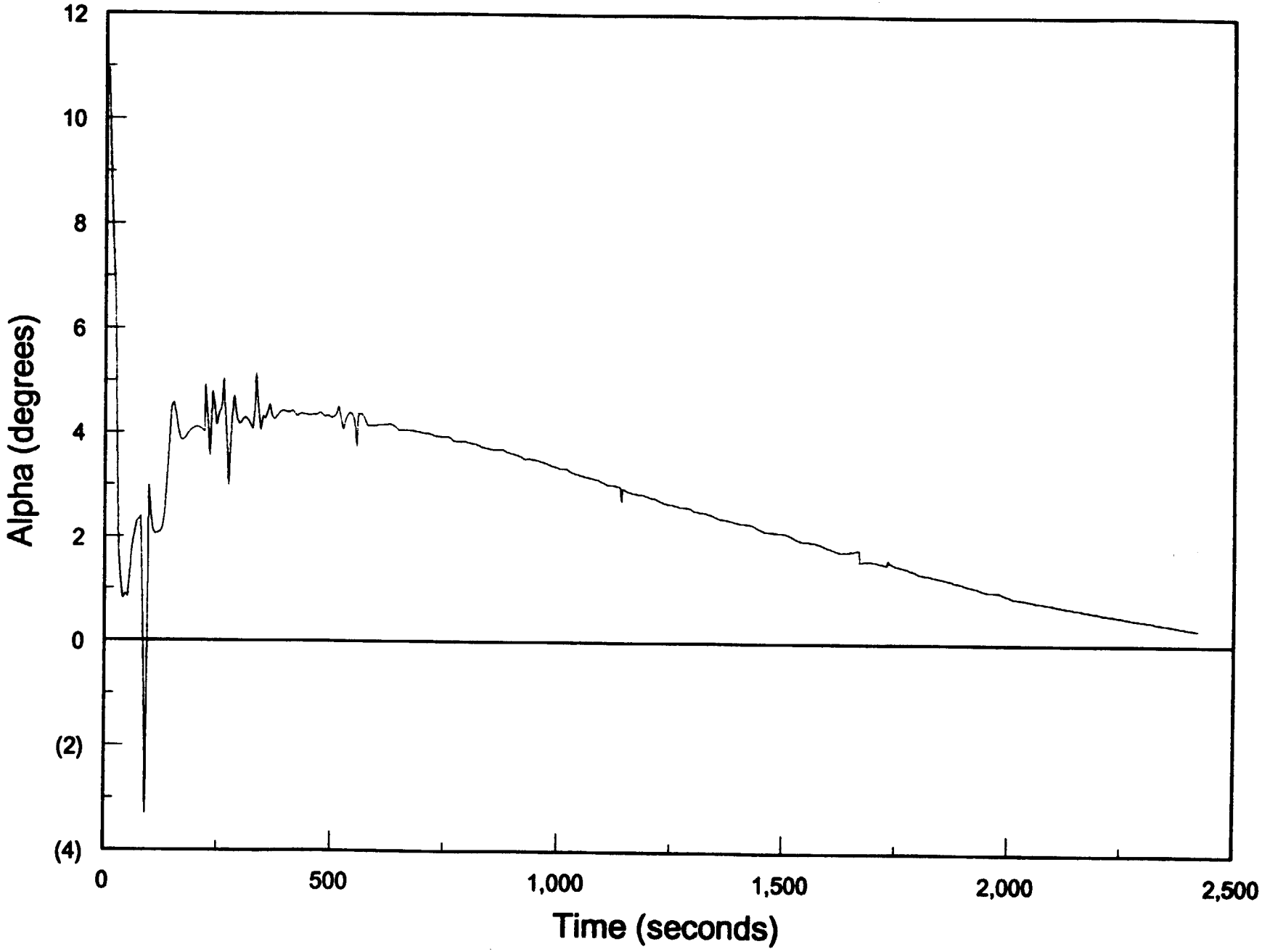

Figure 8. Alpha vs time - phase I model

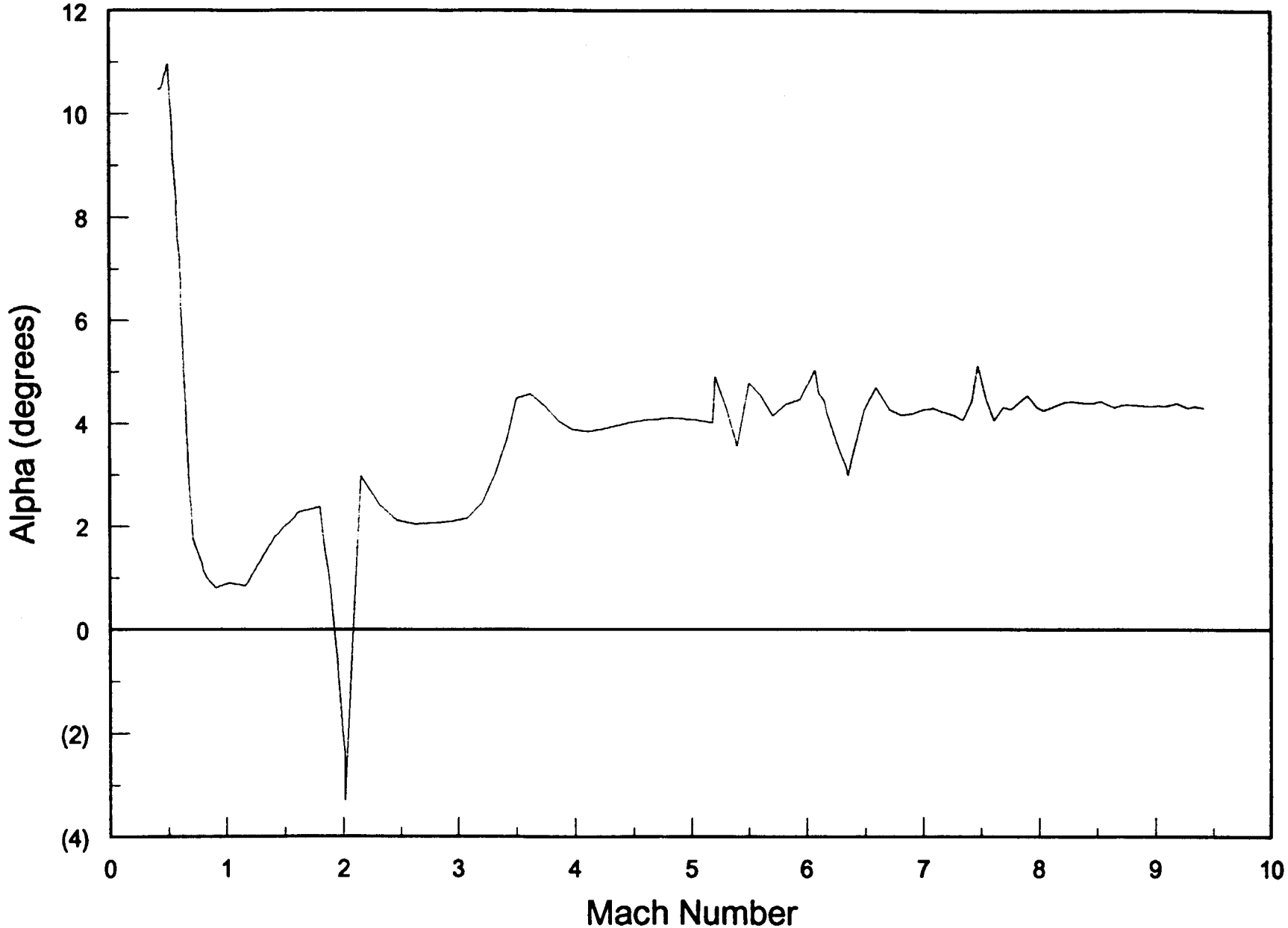

Figure 9. Alpha vs Mach - phase I model

First 500 seconds of flight

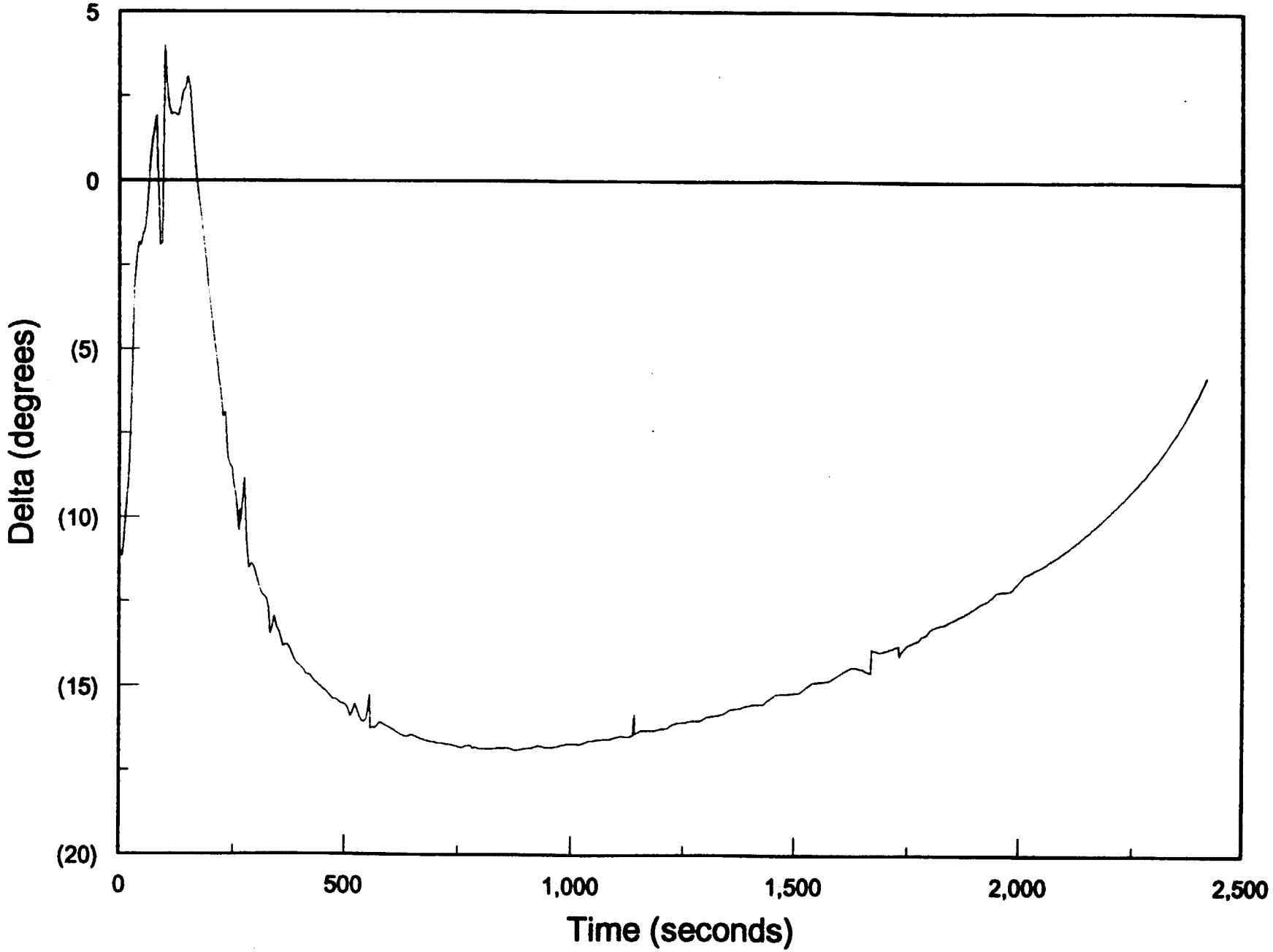

Figure 10. Delta vs time - phase I model

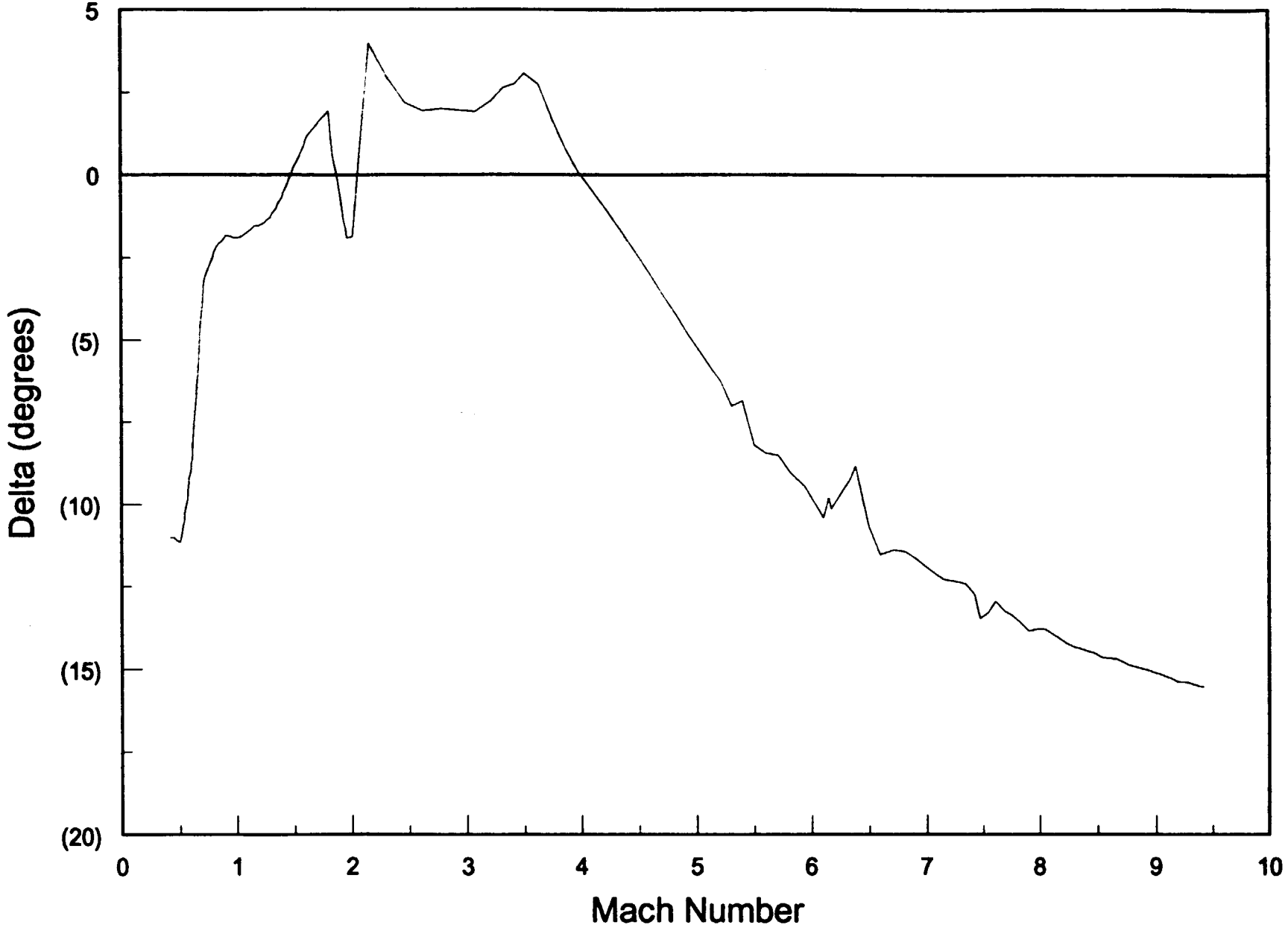

Figure 11. Delta vs Mach number - phase I model
First 500 seconds of flight

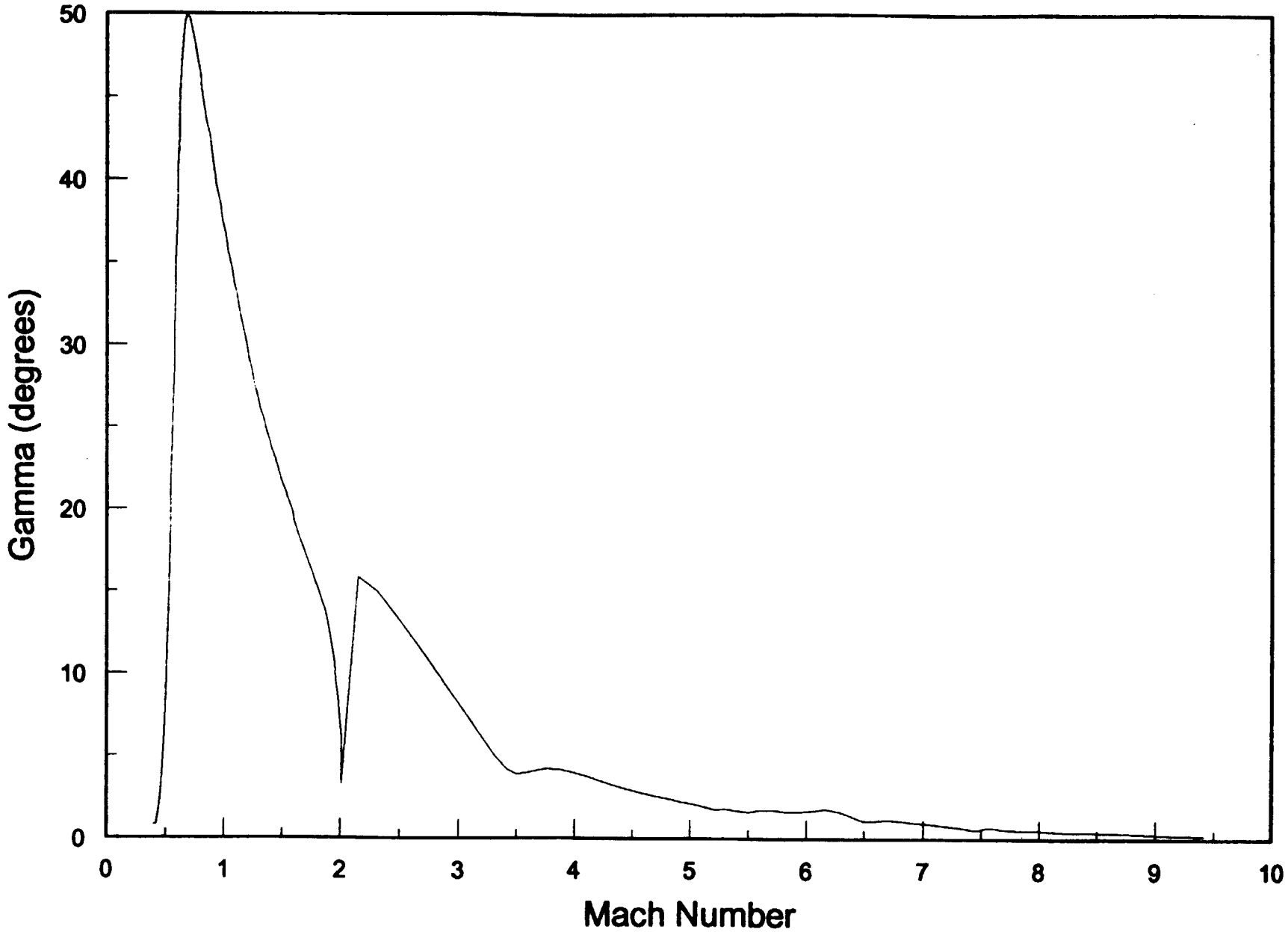

Figure 12. Gamma vs Mach number - phase I model
First 500 seconds of flight

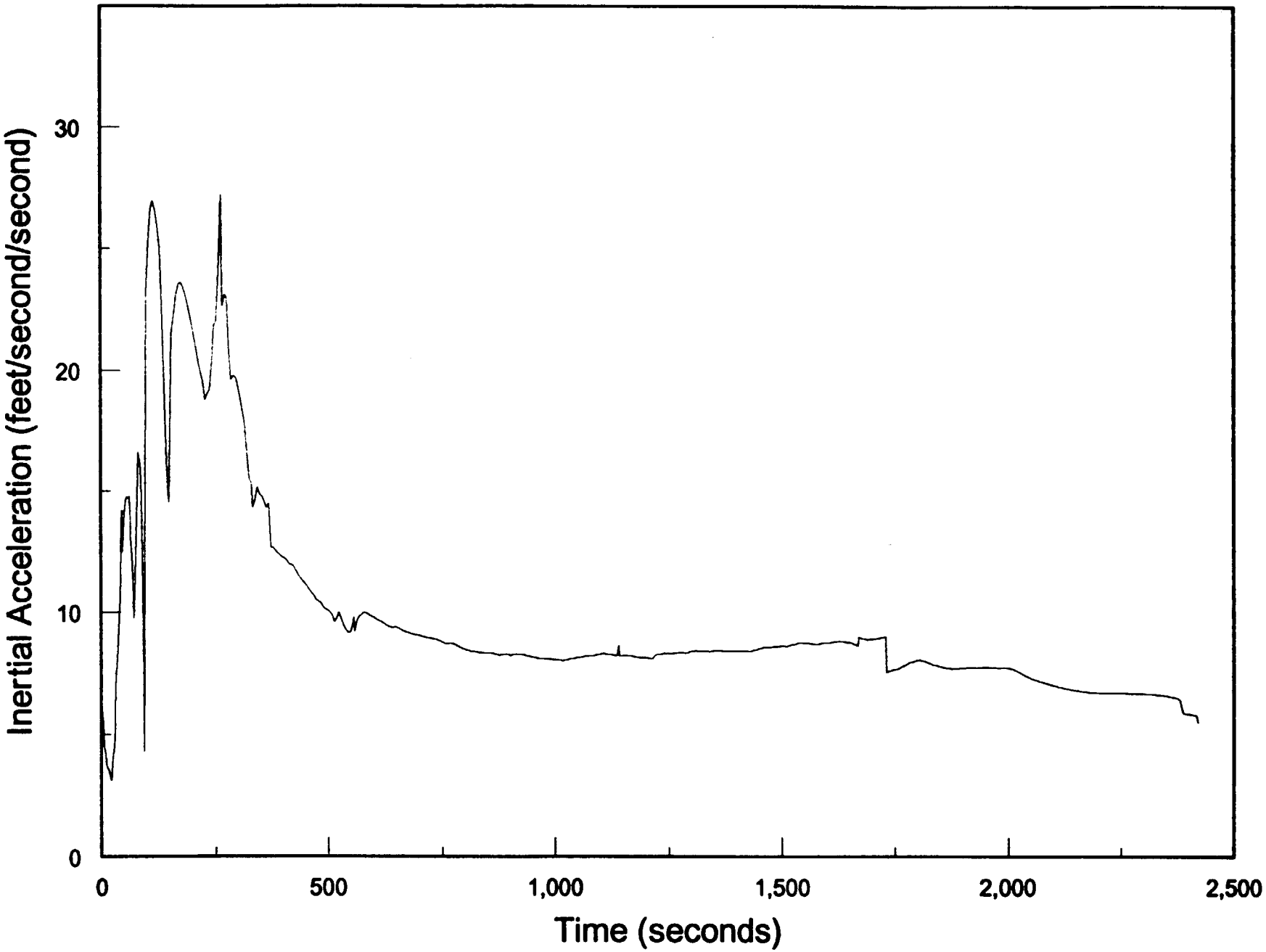

Figure 13. Accel. vs time - phase I model

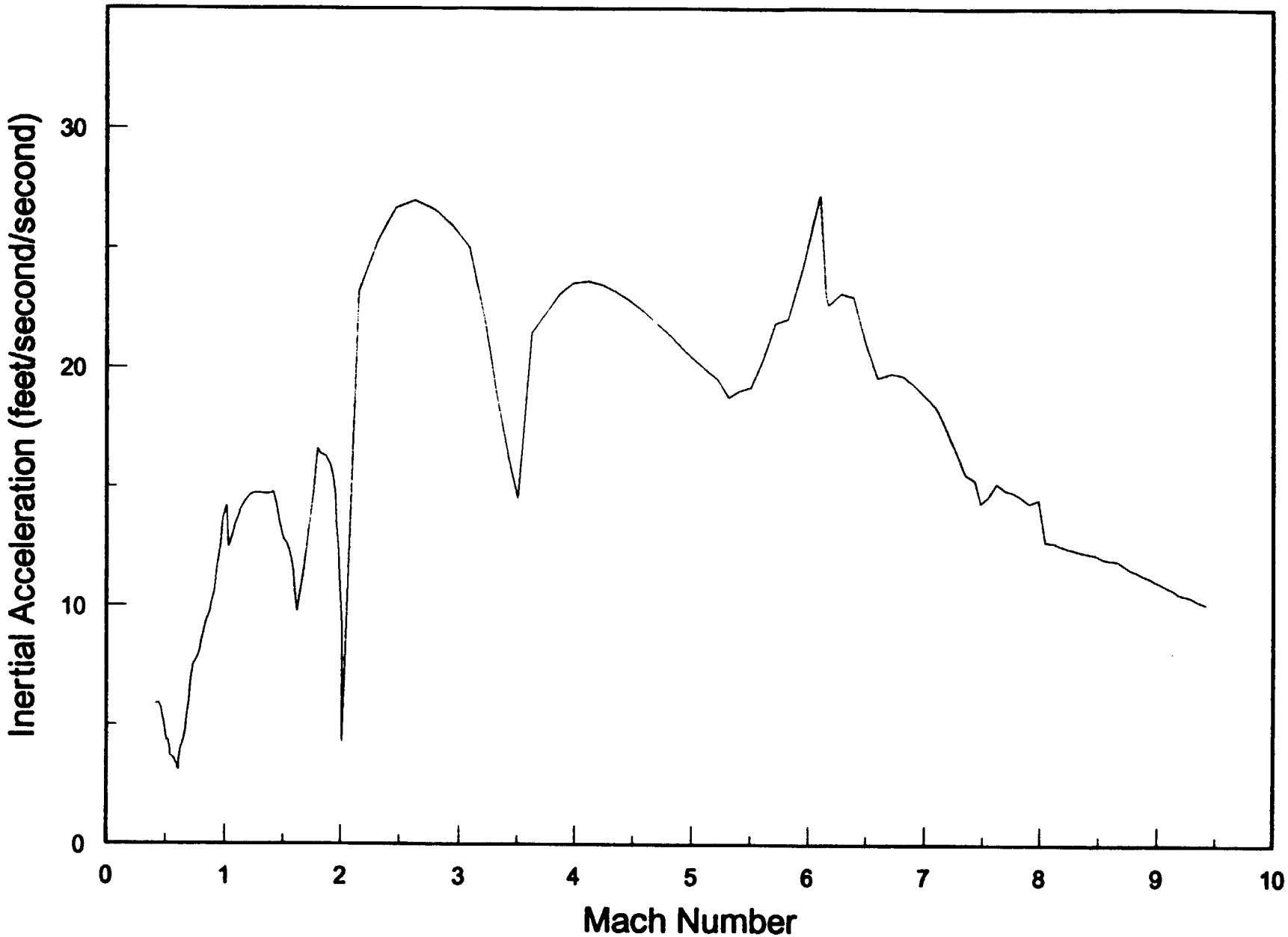

Figure 14. Accel. vs Mach Number - phase I model
First 500 seconds of flight

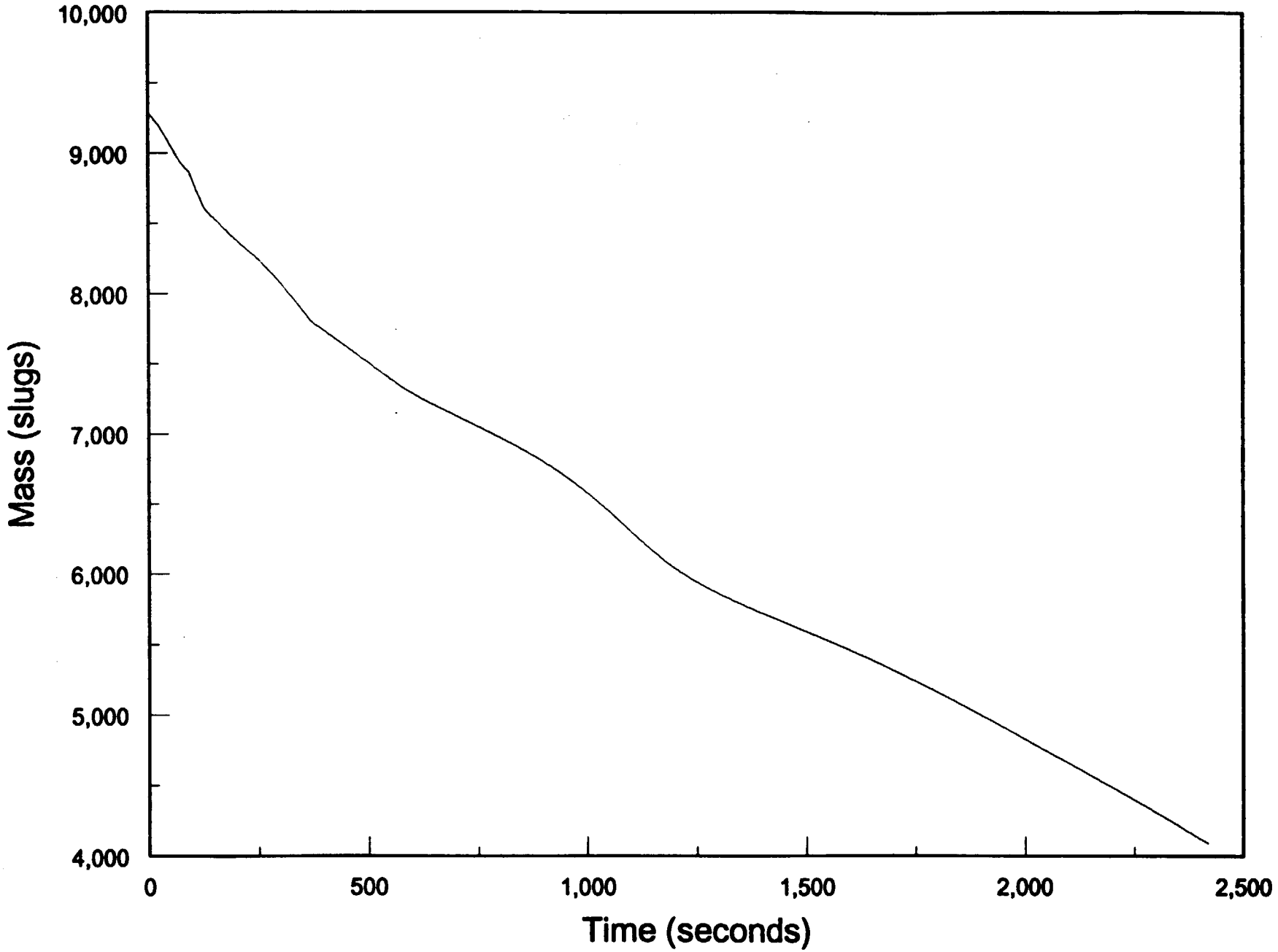

Figure 15. Mass vs time - phase I model

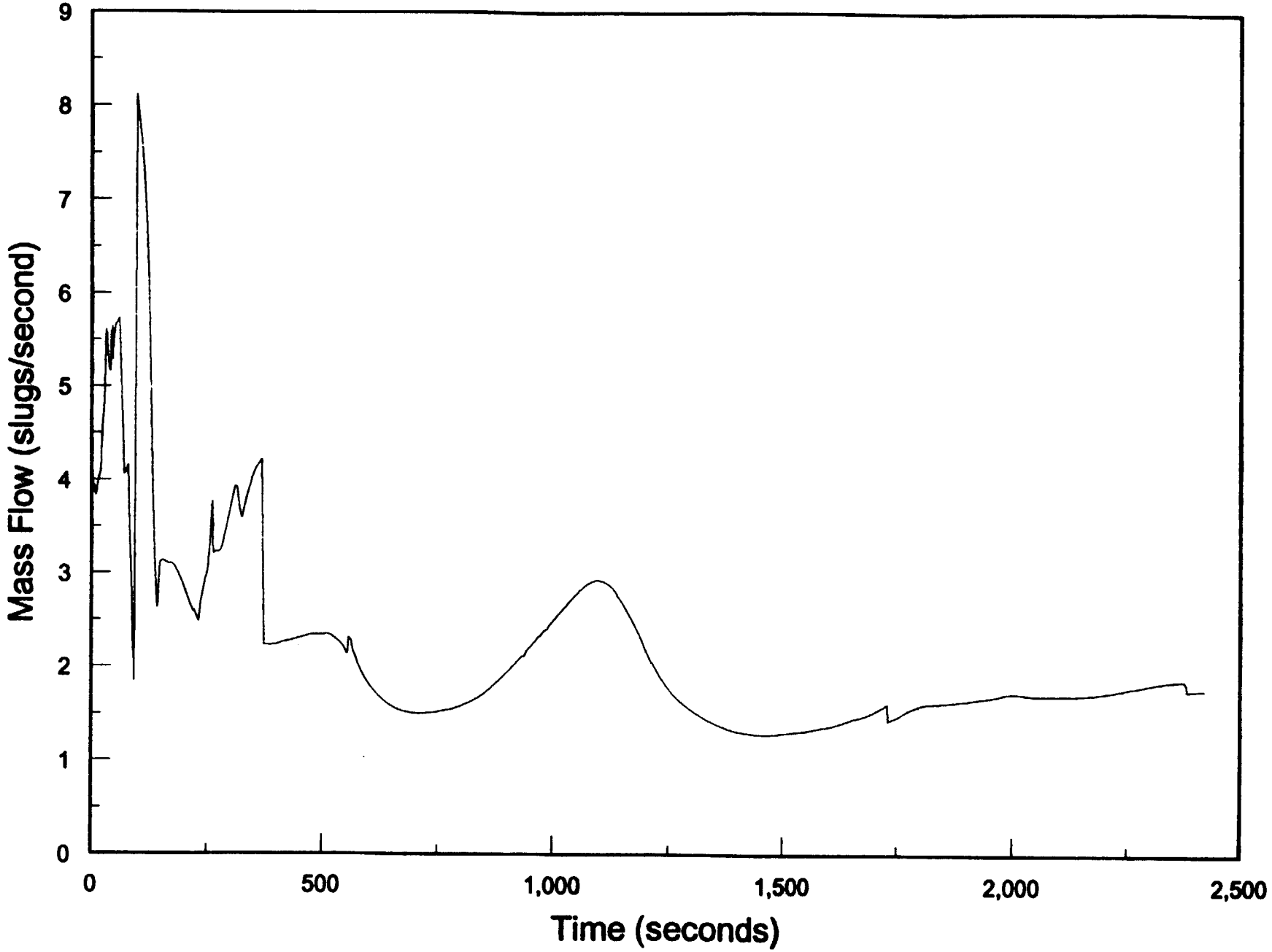

Figure 16. Mass flow vs time - phase I model

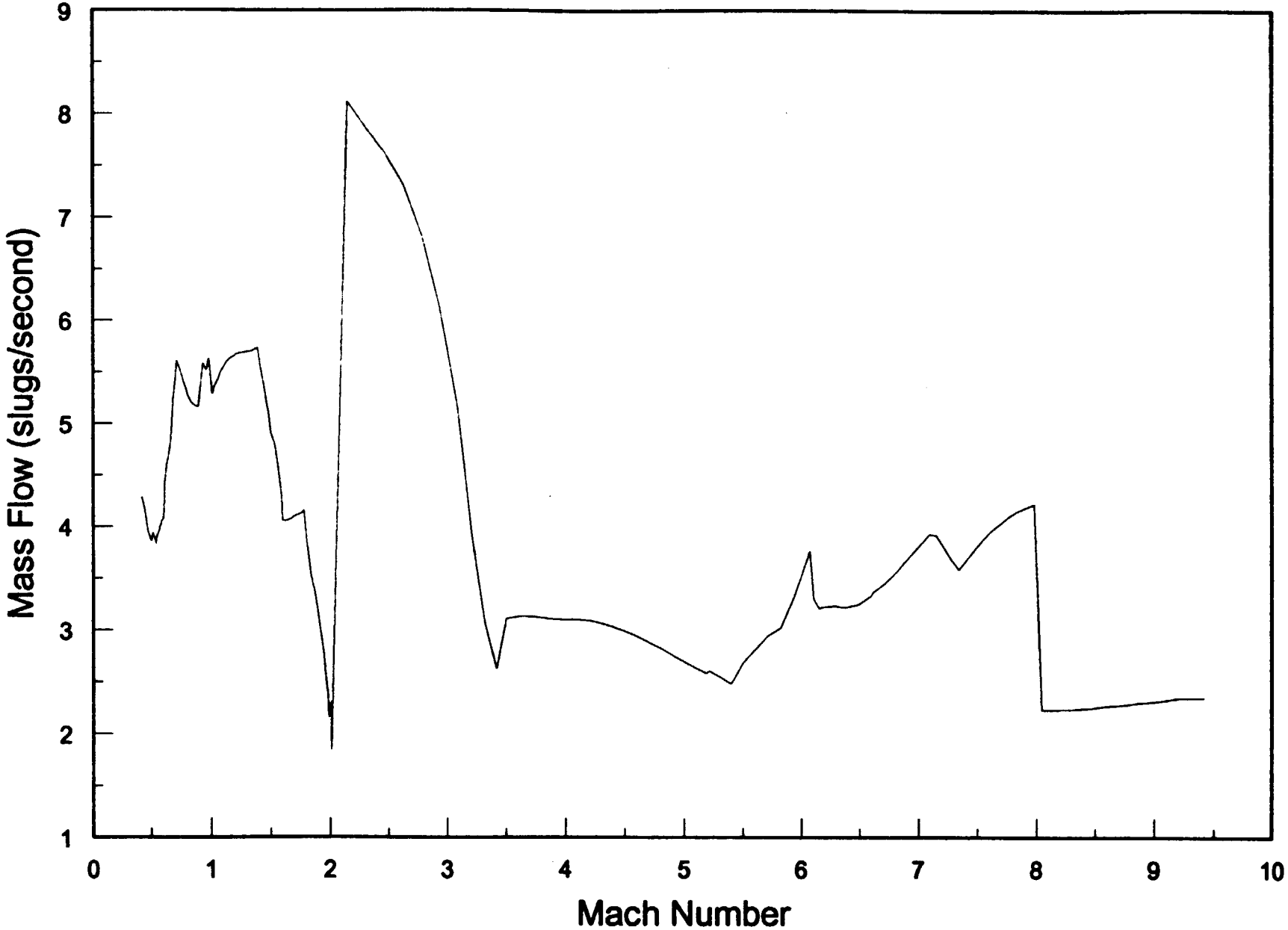

Figure 17. Mass Flow vs Mach - phase I model
First 500 seconds of flight

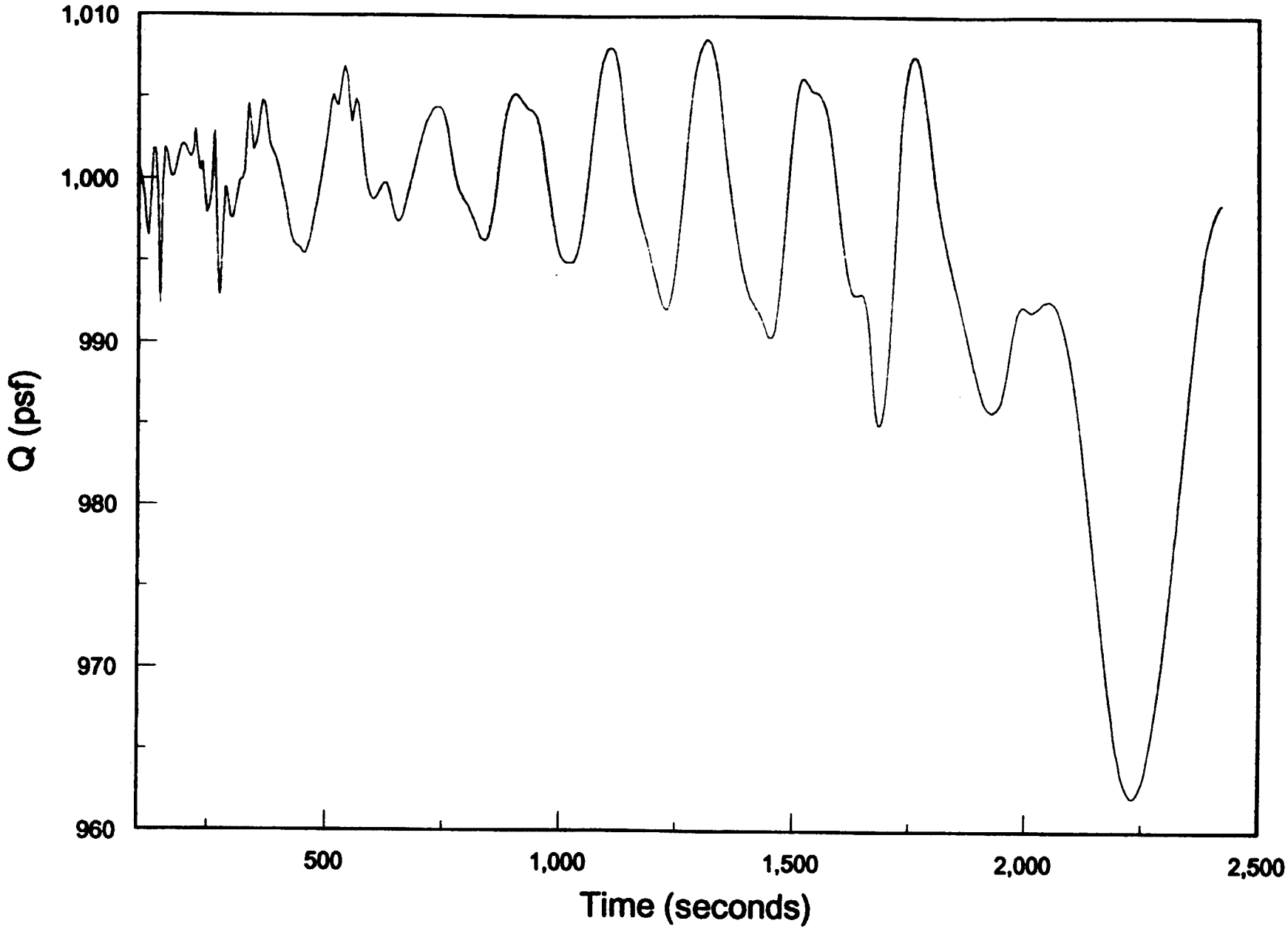

Figure 18. Q vs time - phase I model
Starting 100 seconds after takeoff

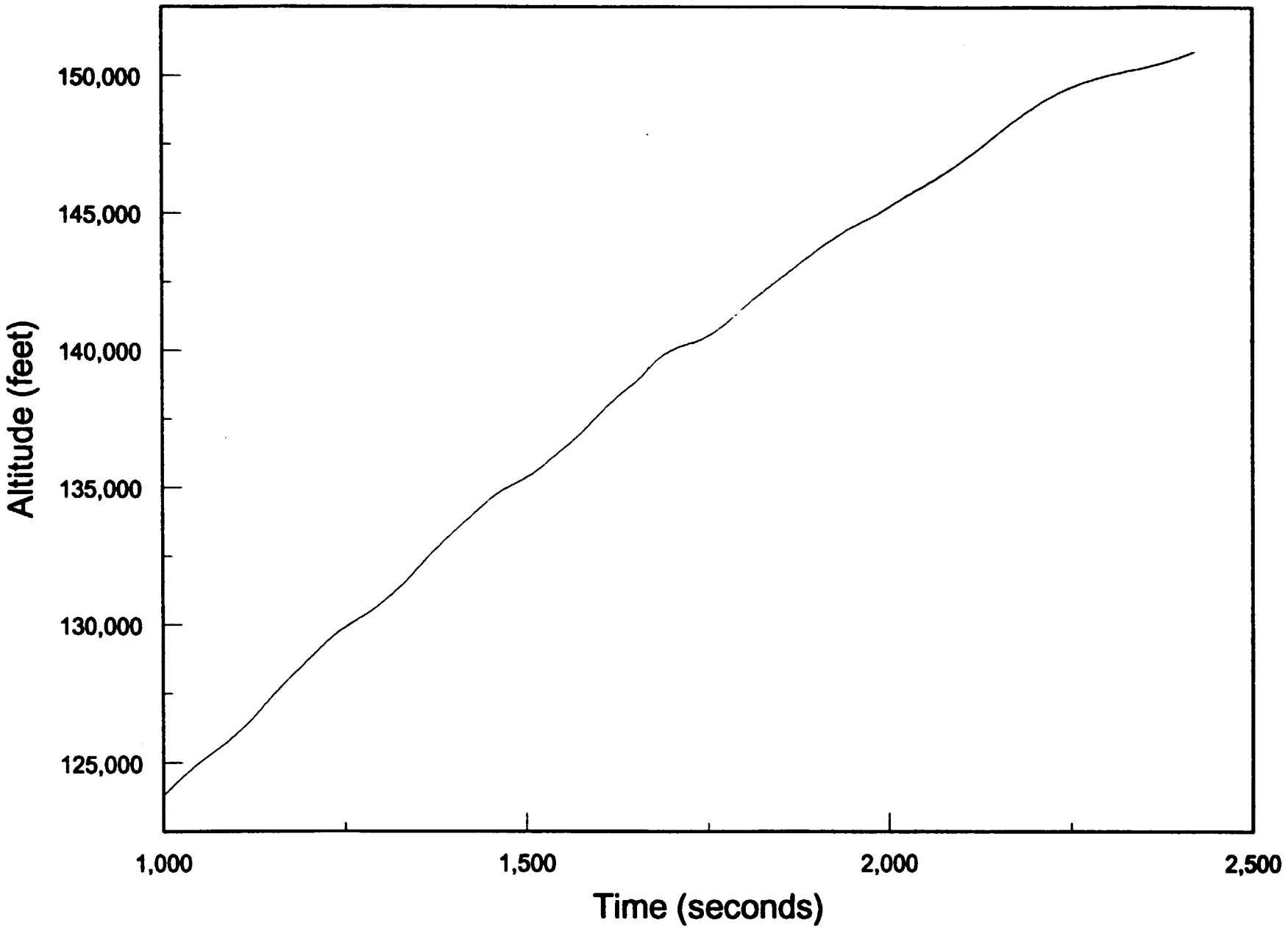

Figure 19. Altitude vs time - phase I model
Starting 1000 seconds after takeoff

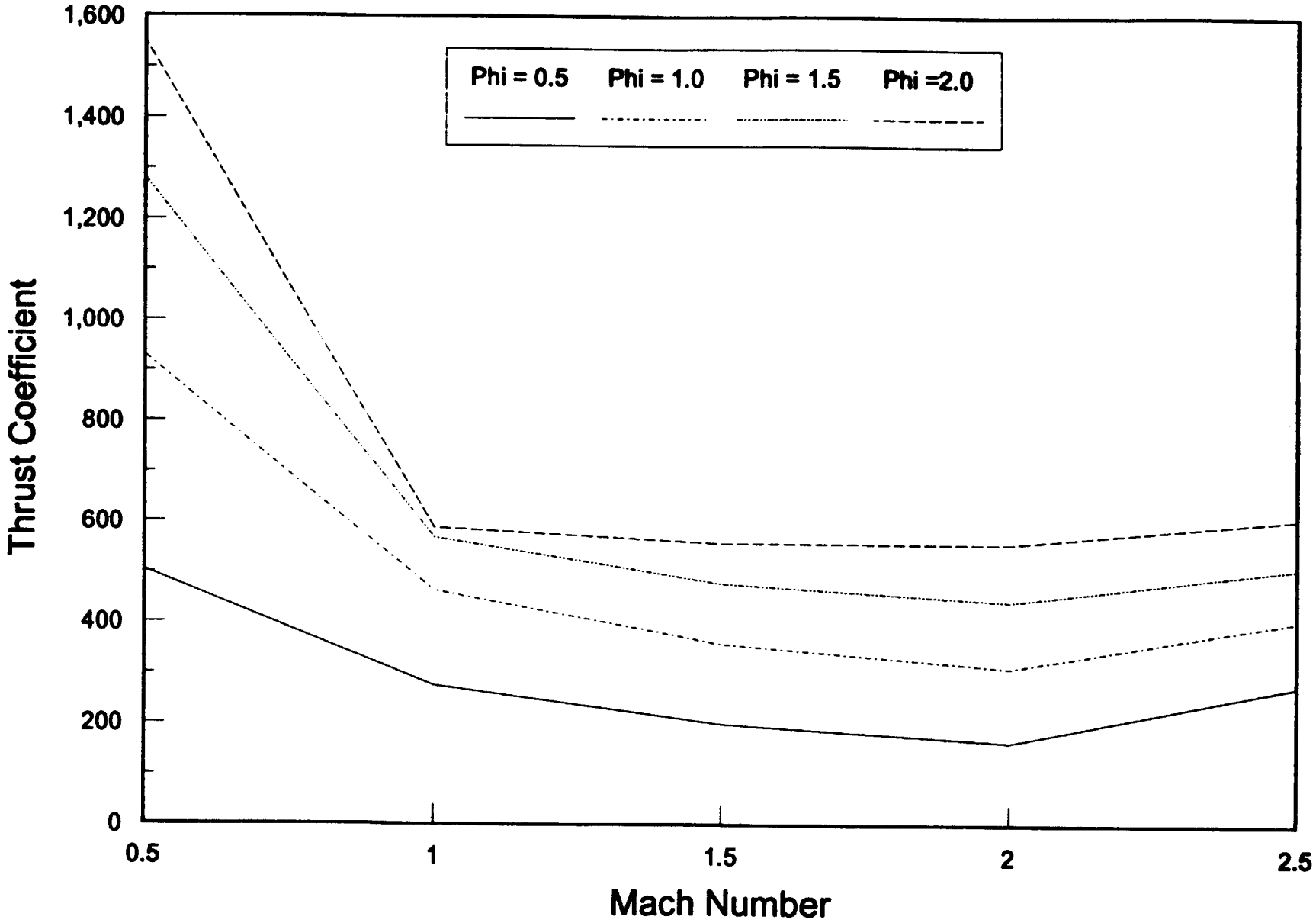

Figure 20. Propulsion model spline data output

Thrust coefficient vs Mach number

Low speed phase

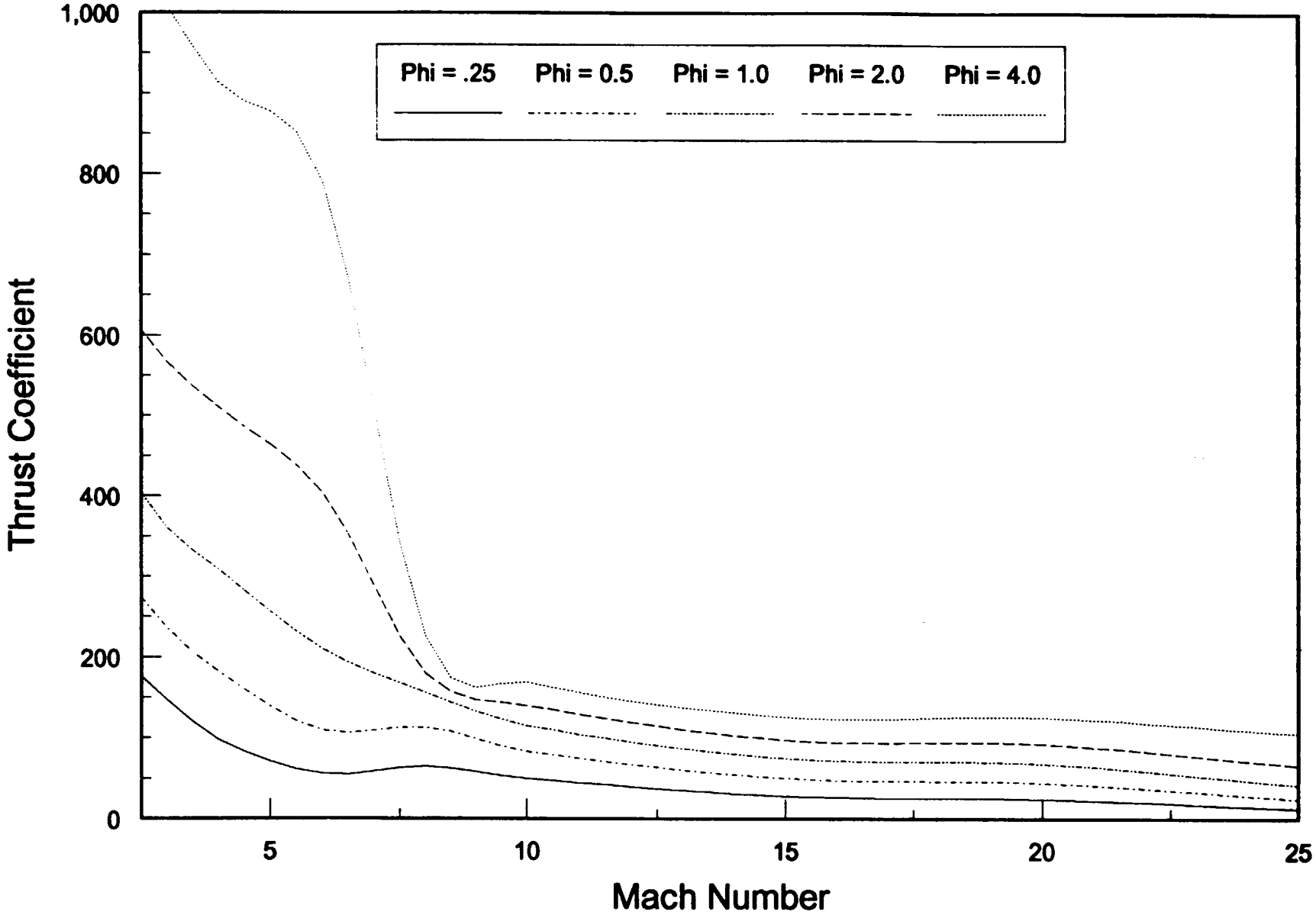

Figure 21. Propulsion model spline data output
Thrust coefficient vs Mach number
High speed phase

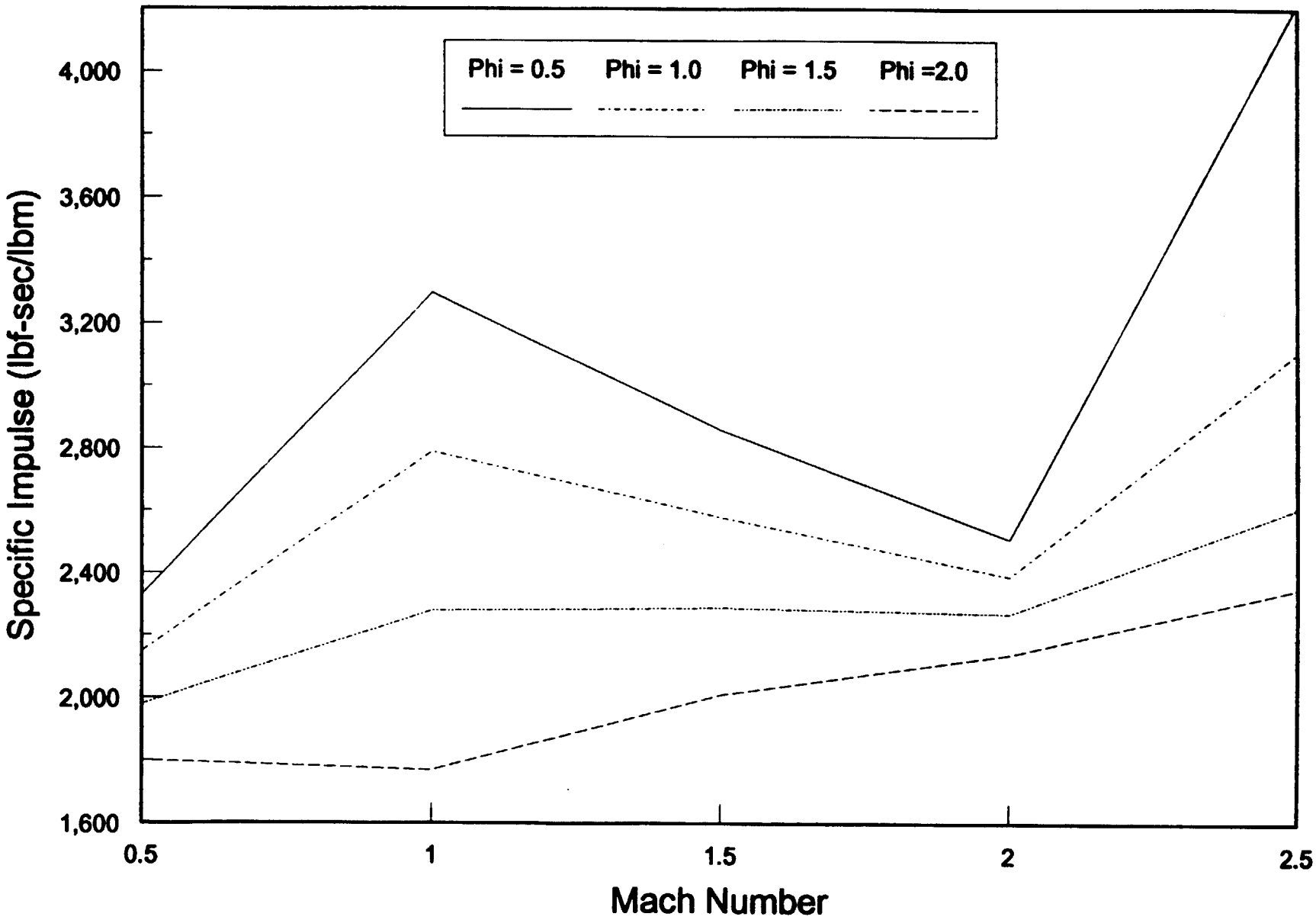

Figure 22. Propulsion model spline data output

Specific impulse vs Mach number

Low speed phase

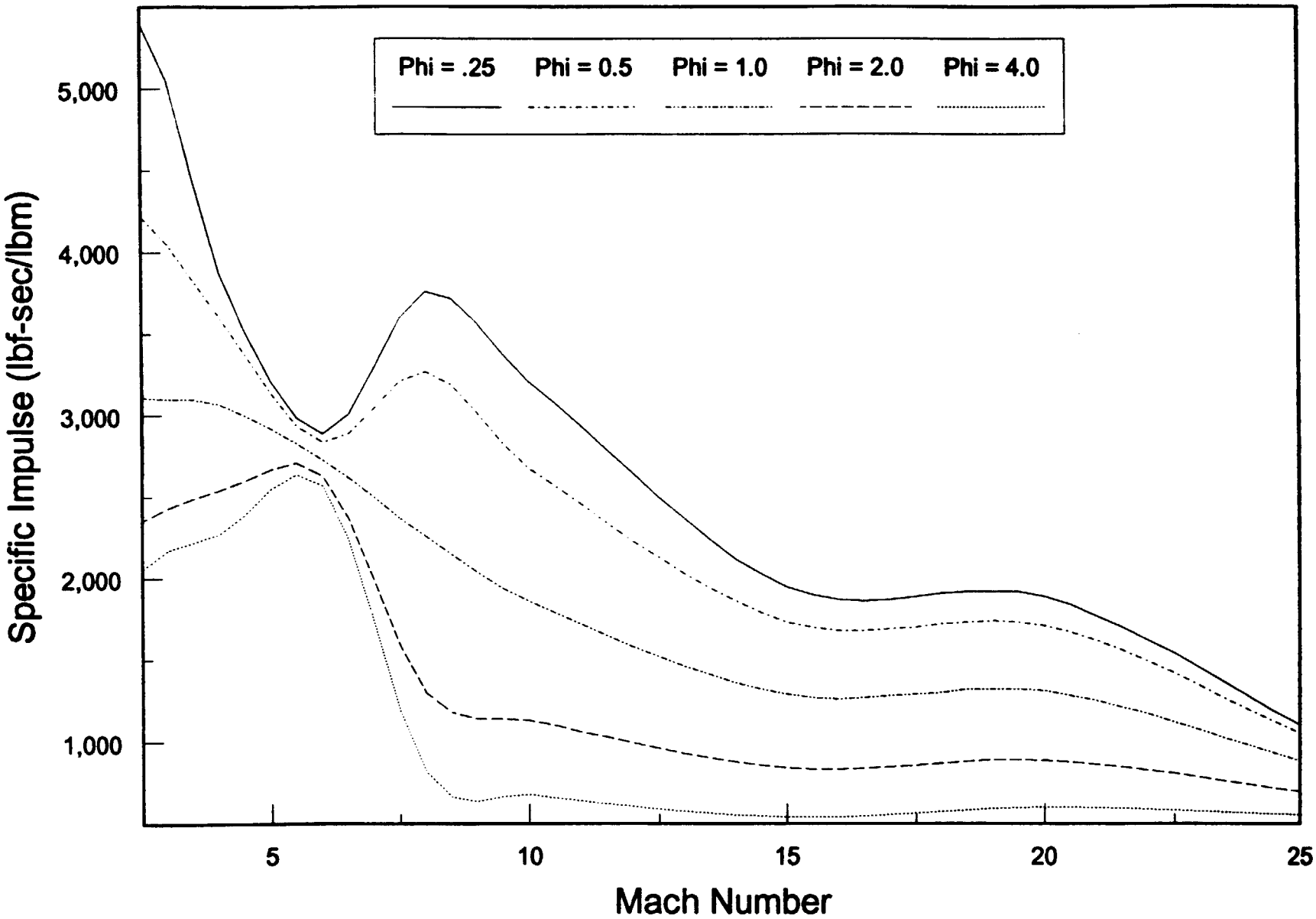

Figure 23. Propulsion model spline data output

Specific impulse vs Mach number

High speed phase

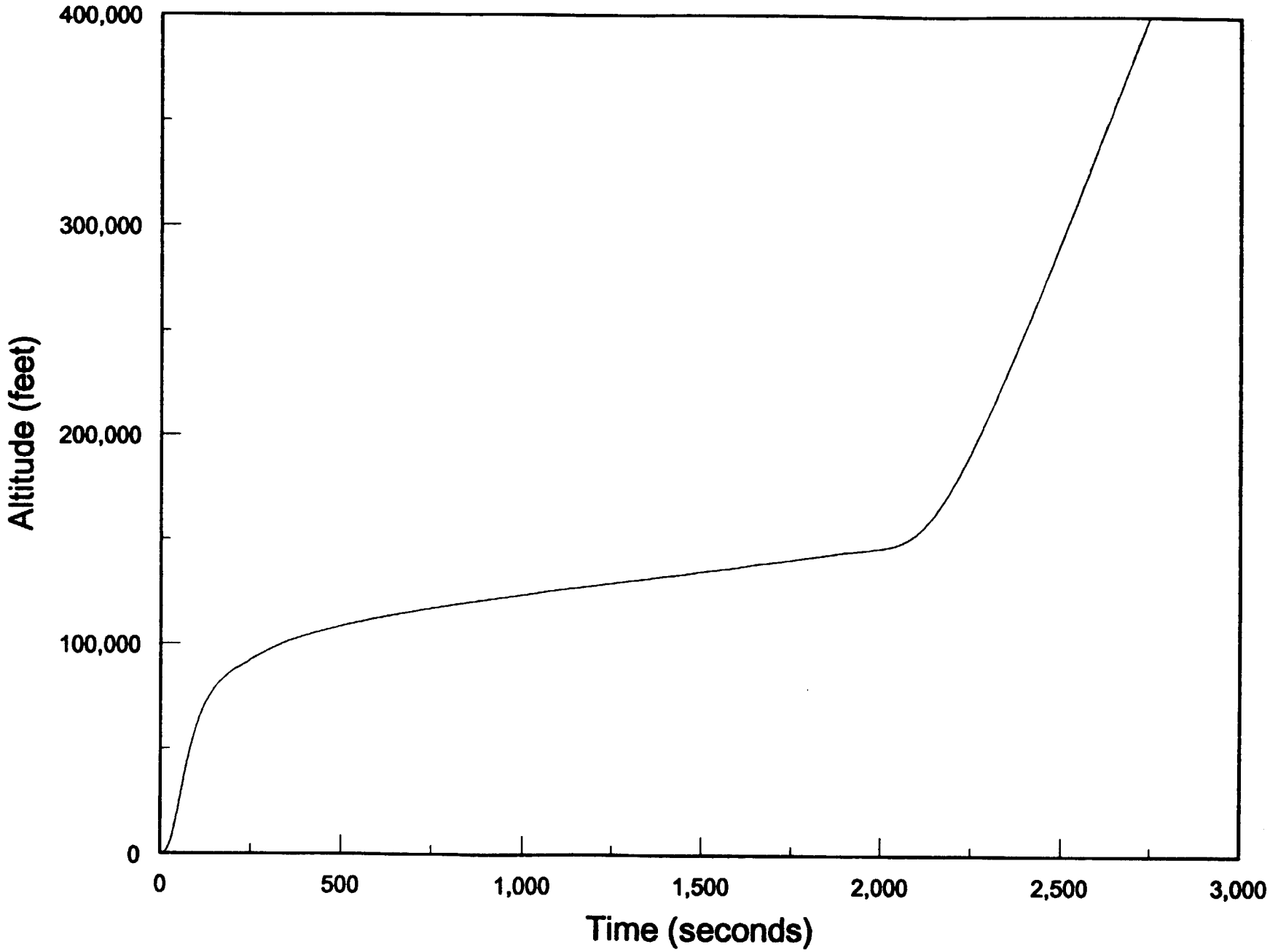

Figure 24. Altitude vs time - phase II model

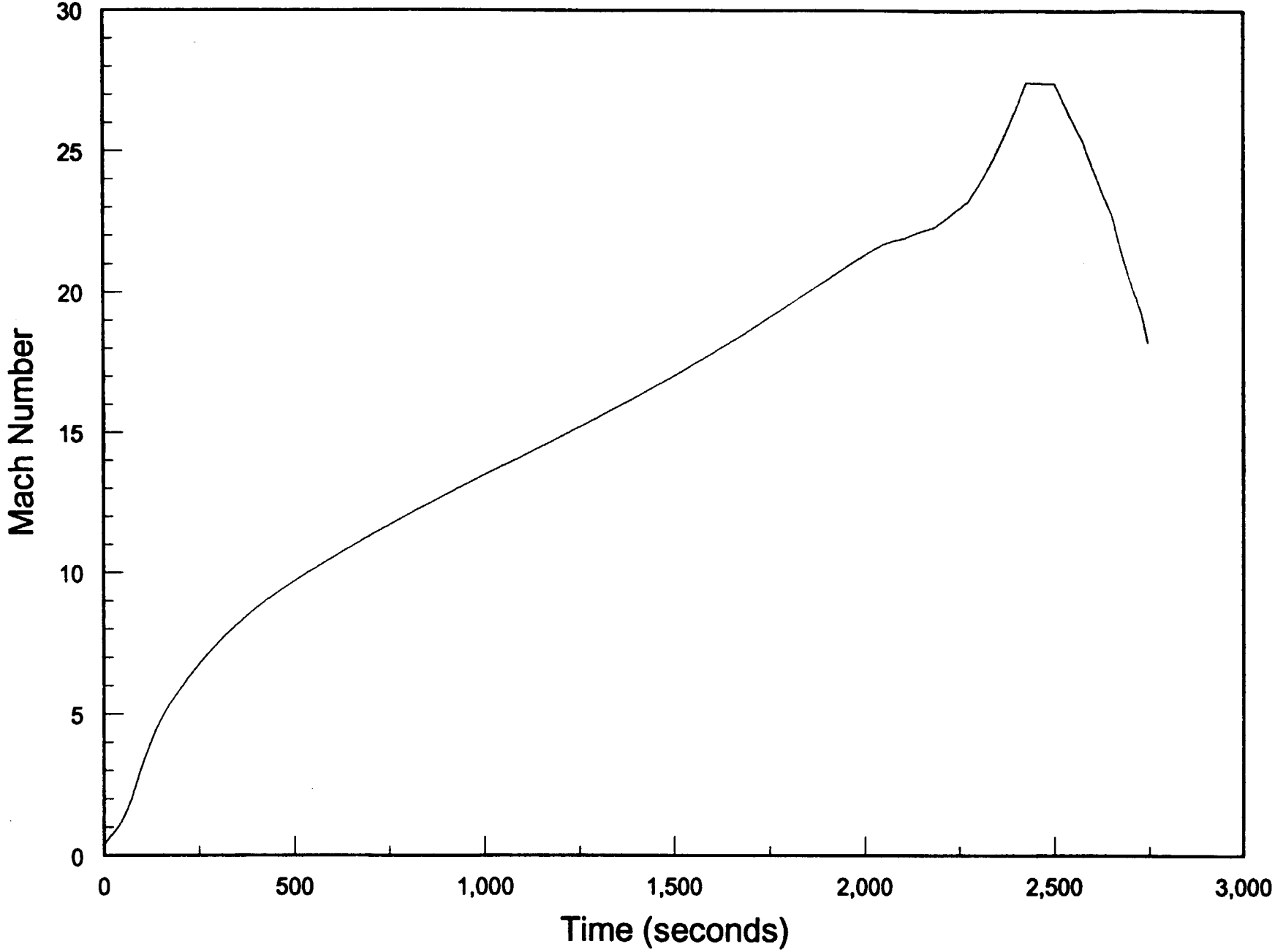

Figure 25. Mach number vs time - phase II model

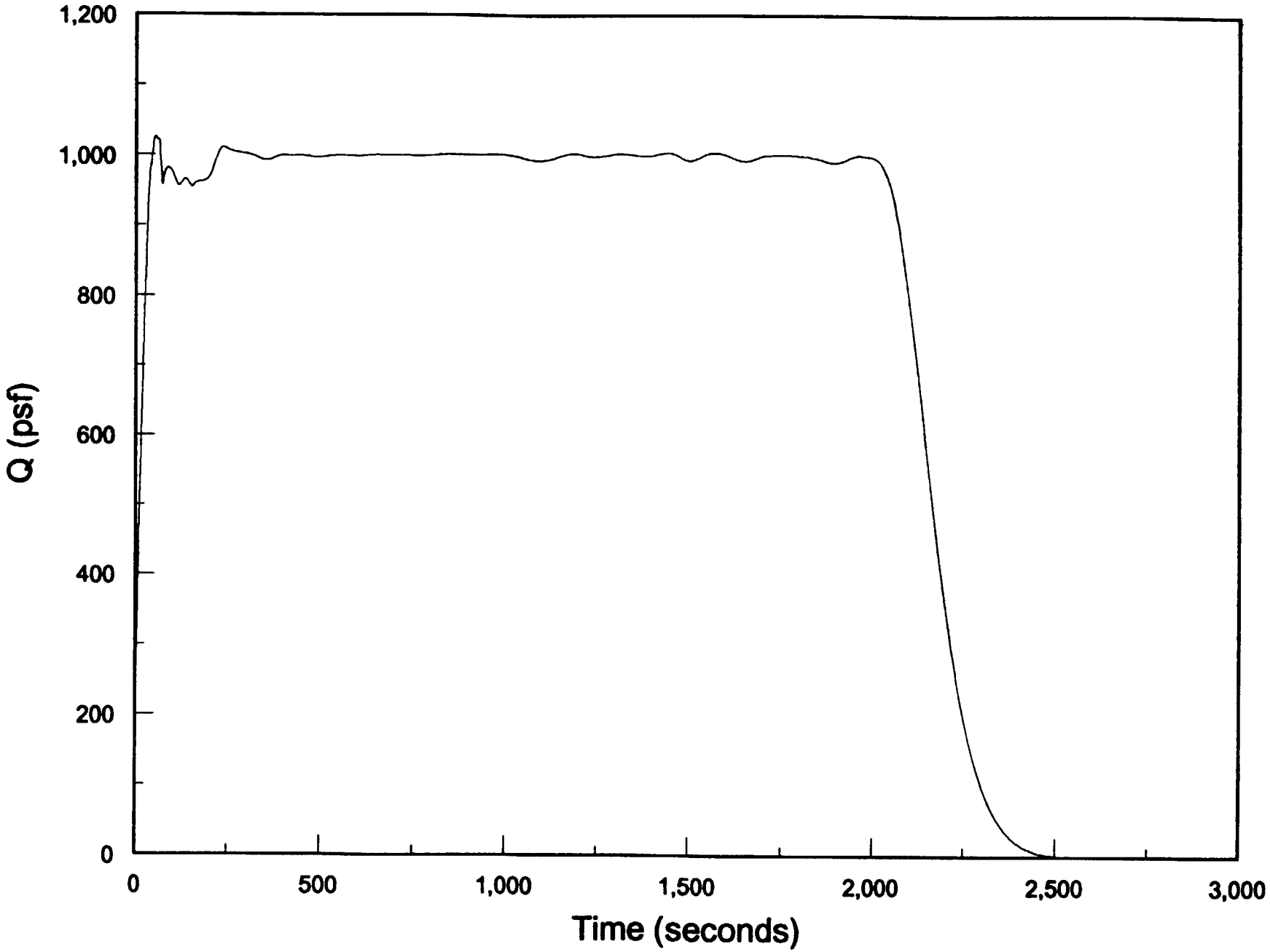

Figure 26. Q vs time - phase II model

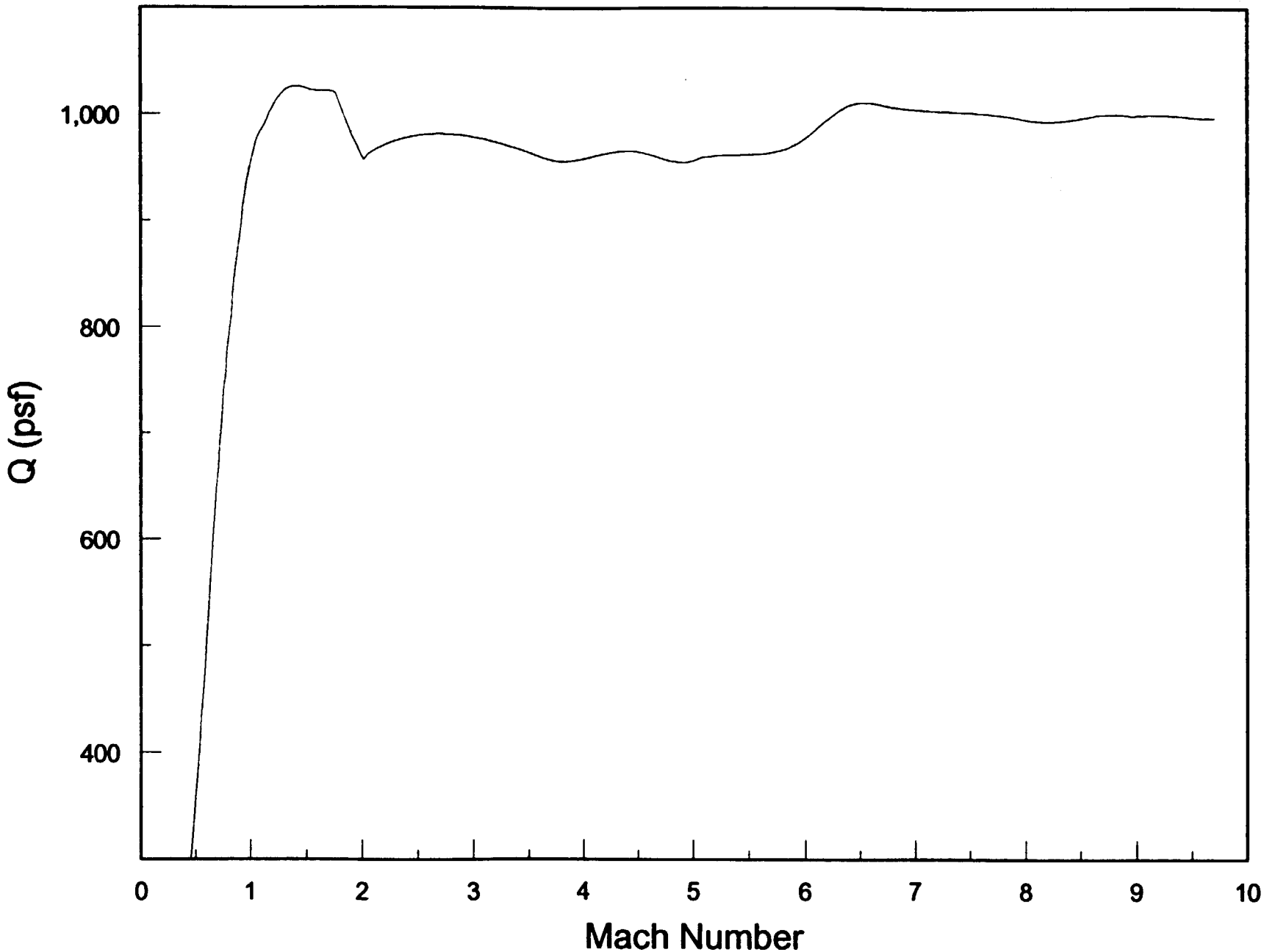

Figure 27. Q vs Mach number - phase II model

First 500 seconds of flight

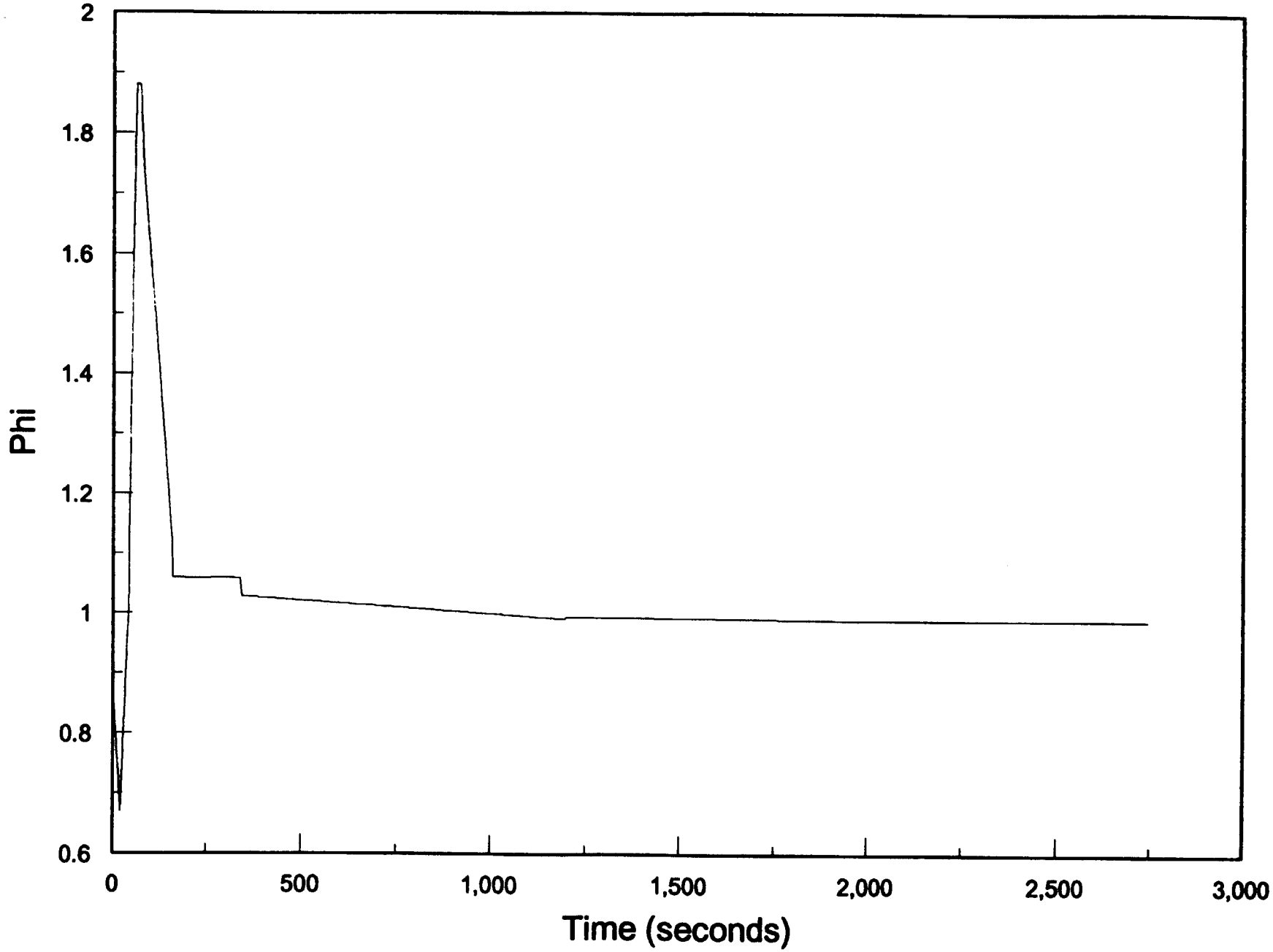

Figure 28. Phi vs time - phase II model

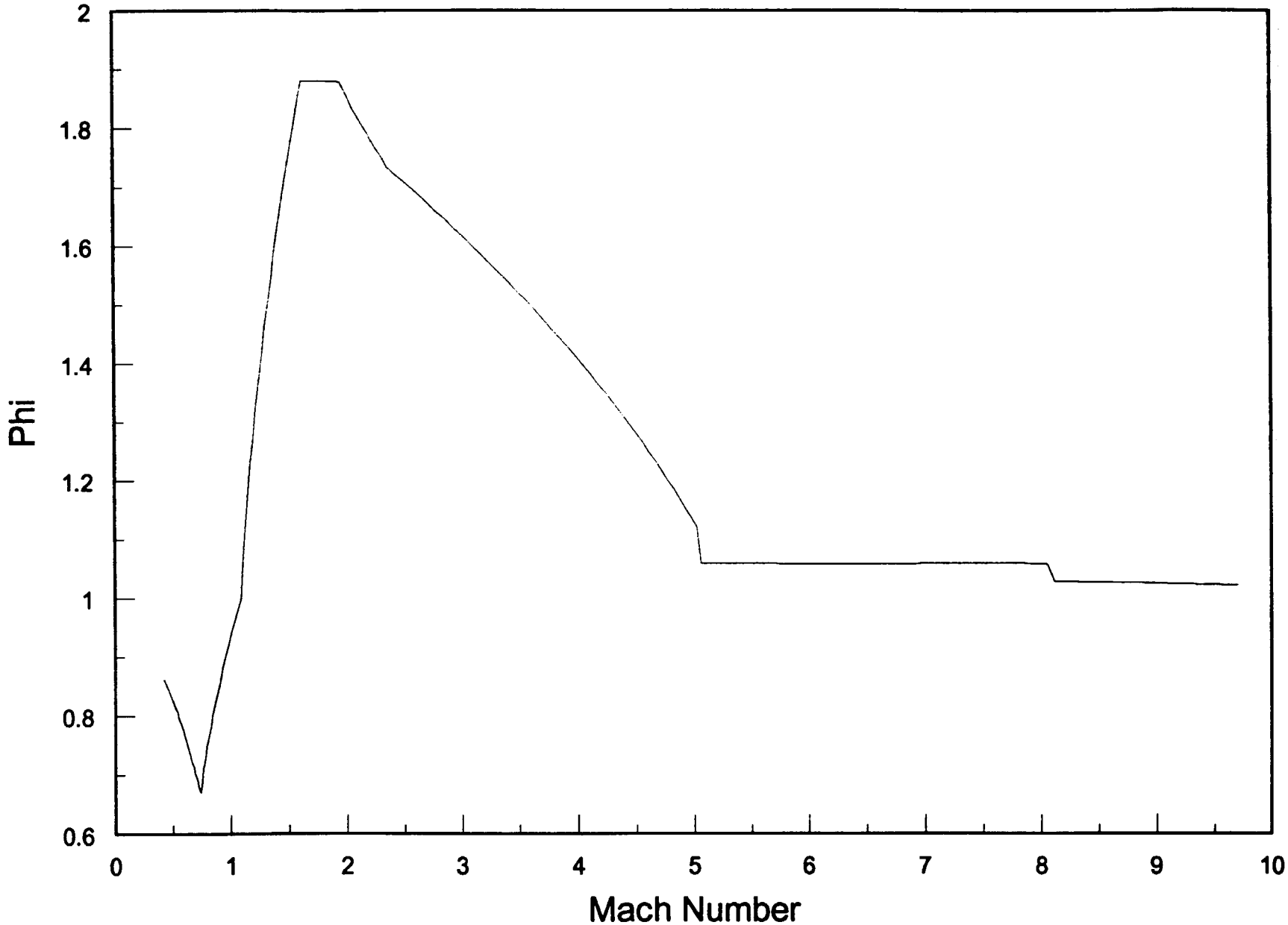

Figure 29. Phi vs Mach number - phase II model

First 500 seconds of flight

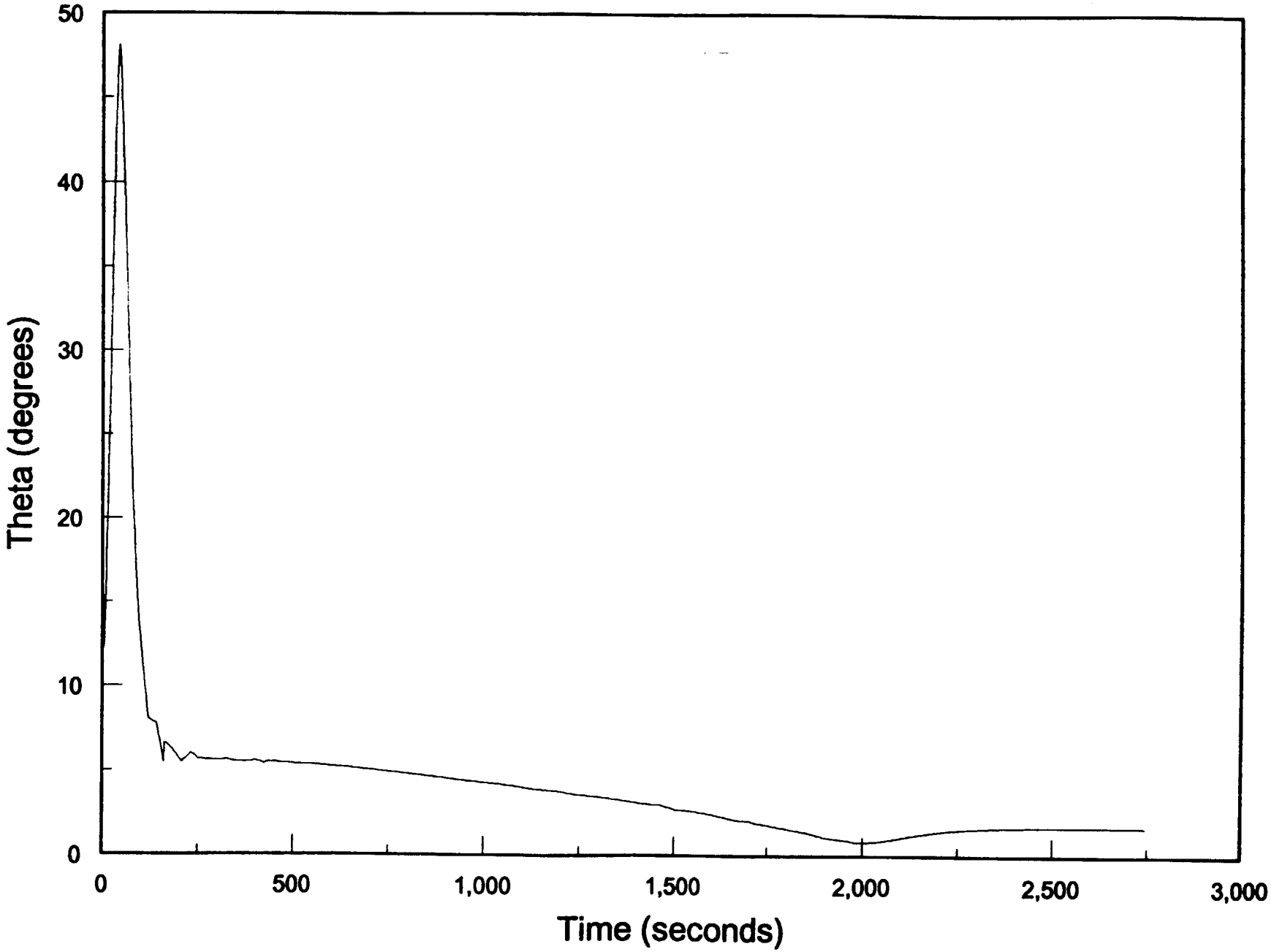

Figure 30. Theta vs time - phase II model

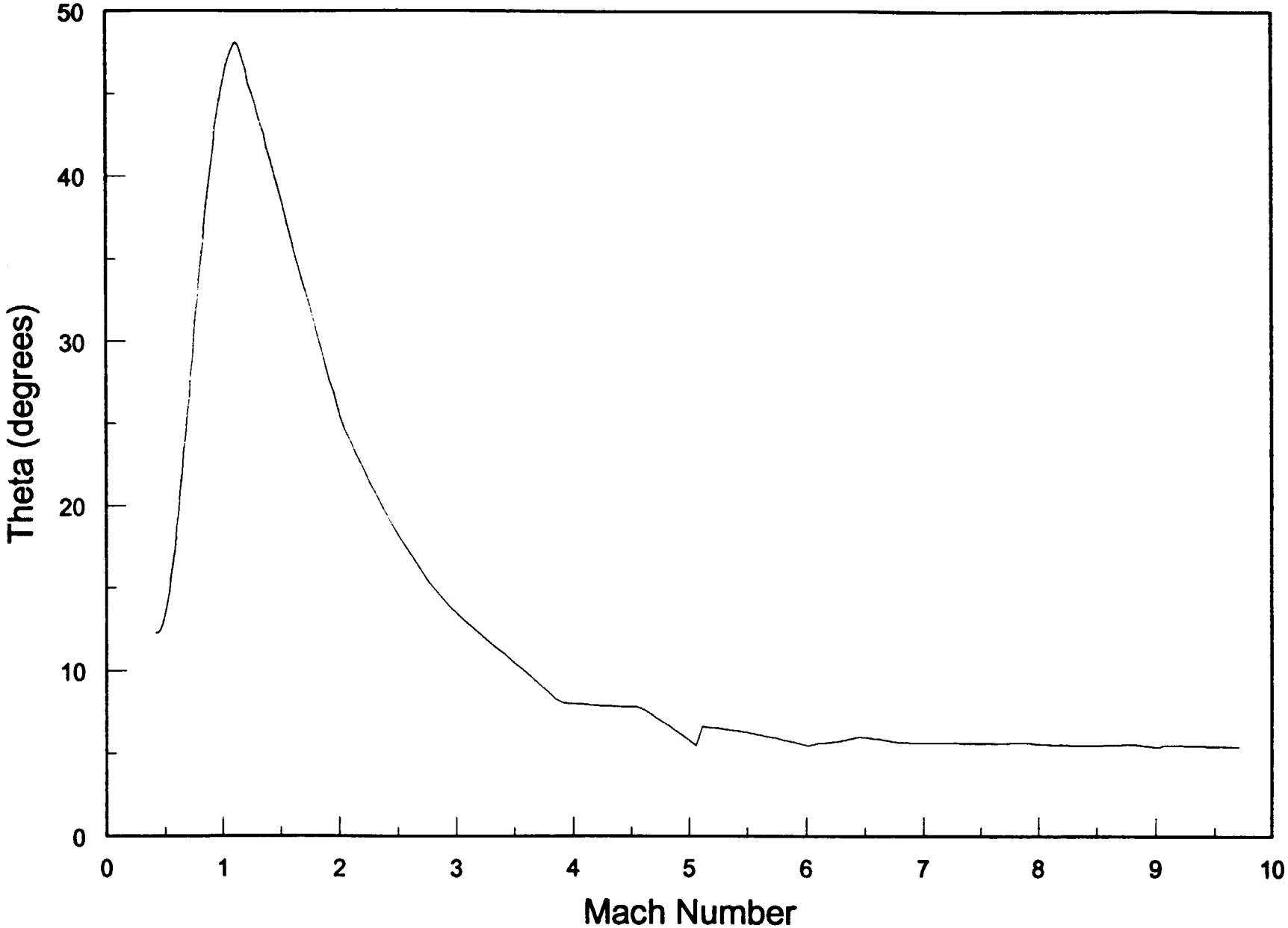

Figure 31. Theta vs Mach number - phase II model
First 500 seconds of flight

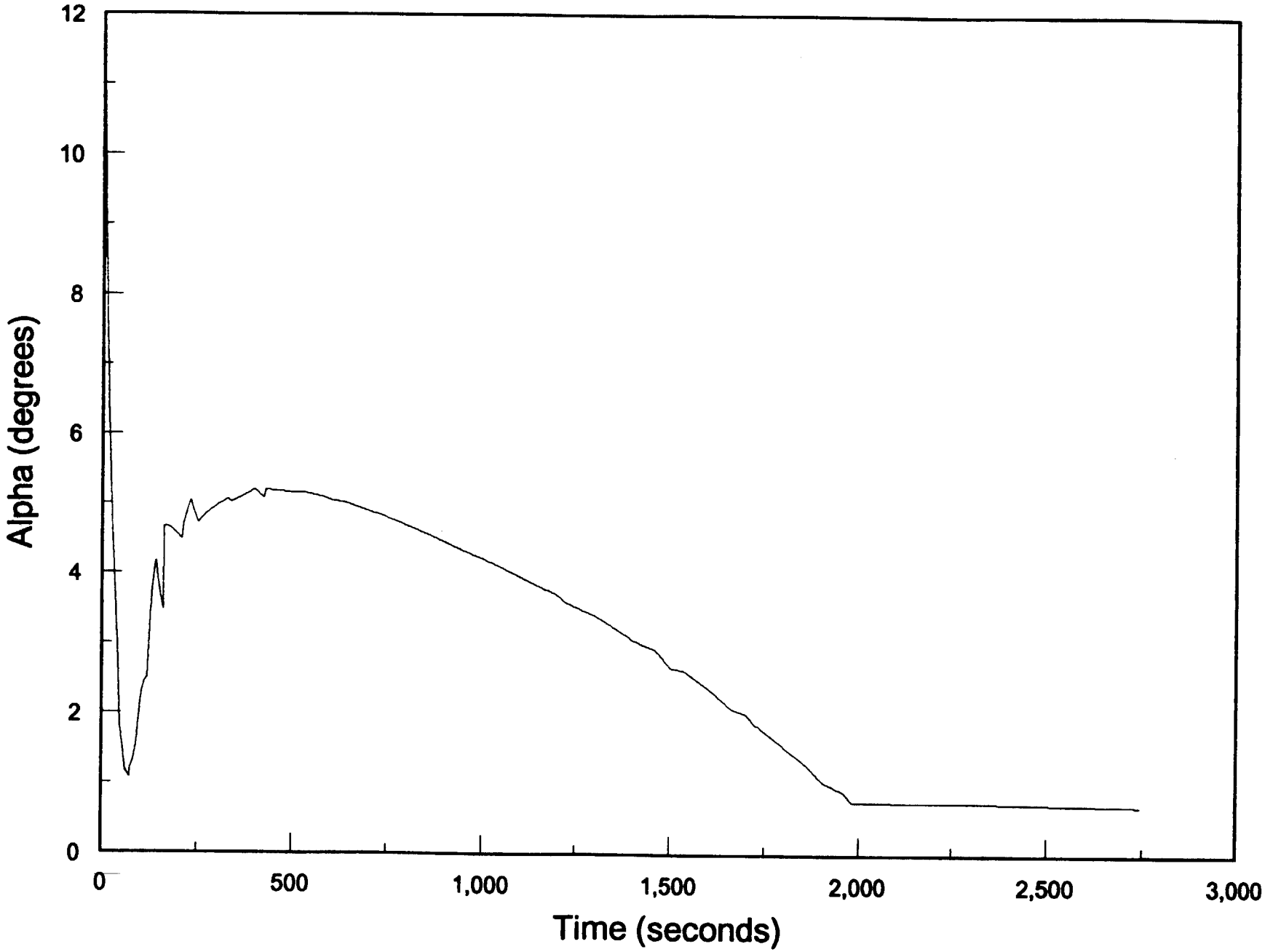

Figure 32. Alpha vs time - phase II model

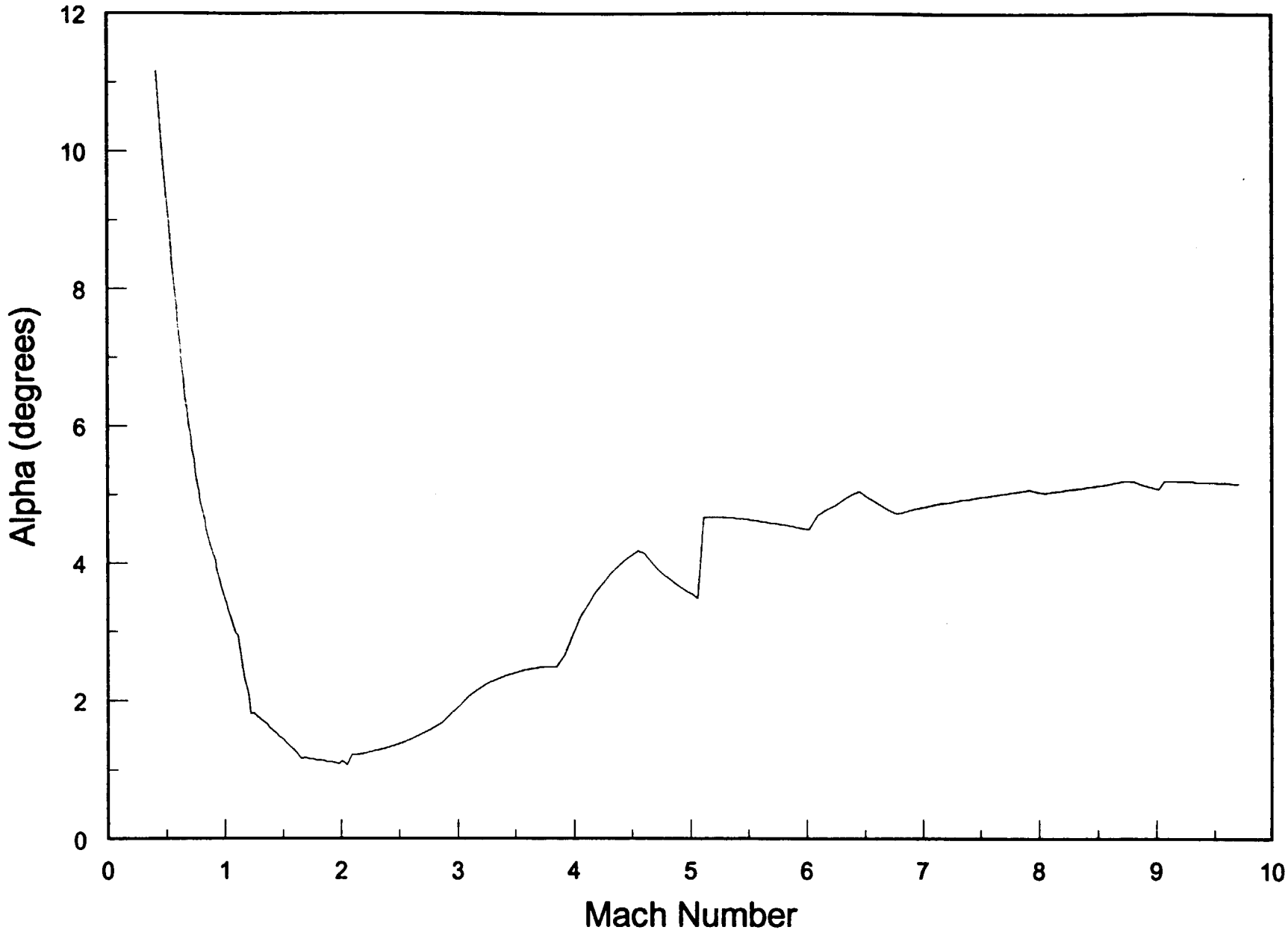

Figure 33. Alpha vs Mach number - phase II model
First 500 seconds of flight

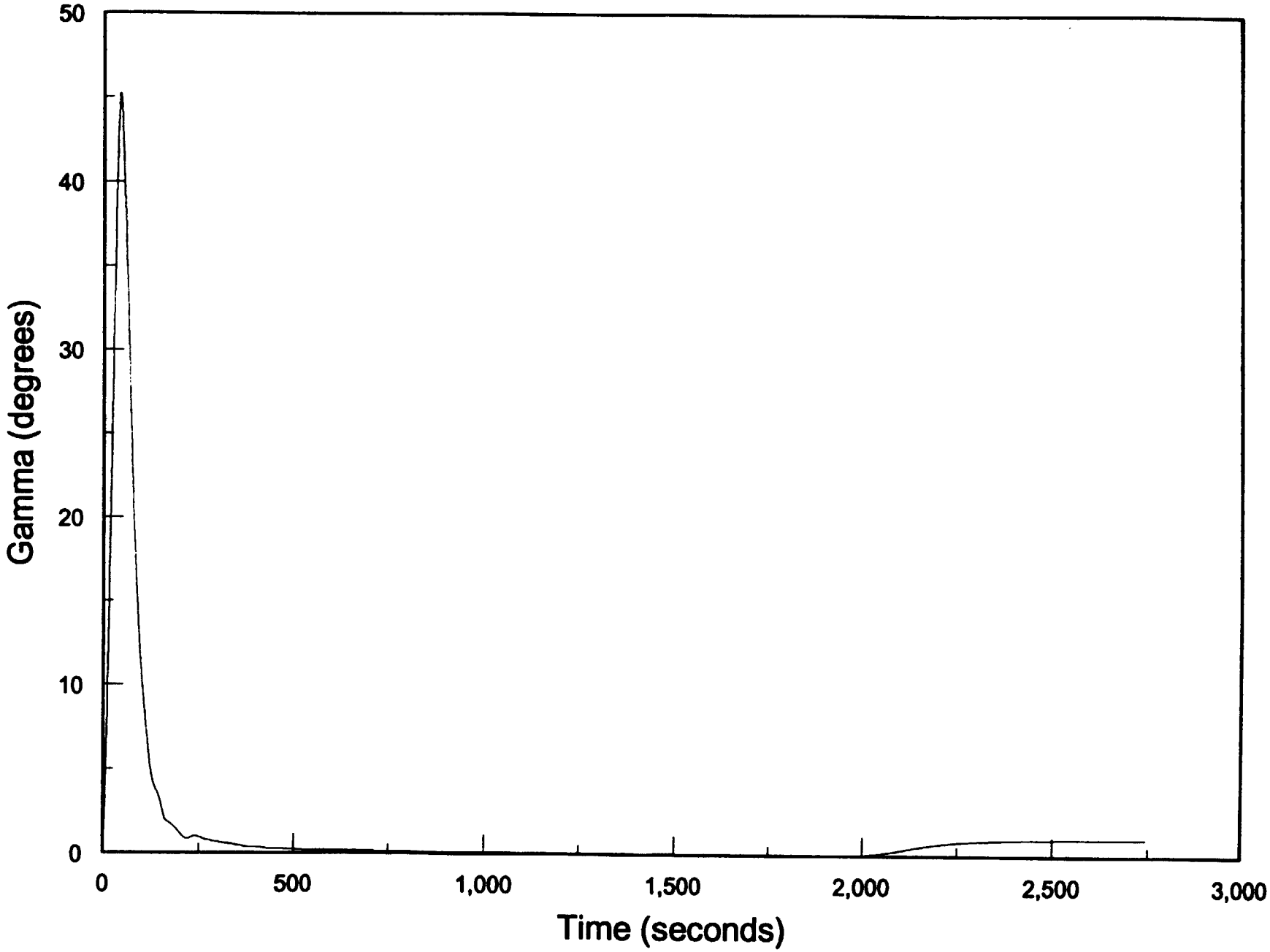

Figure 34. Gamma vs time - phase II model

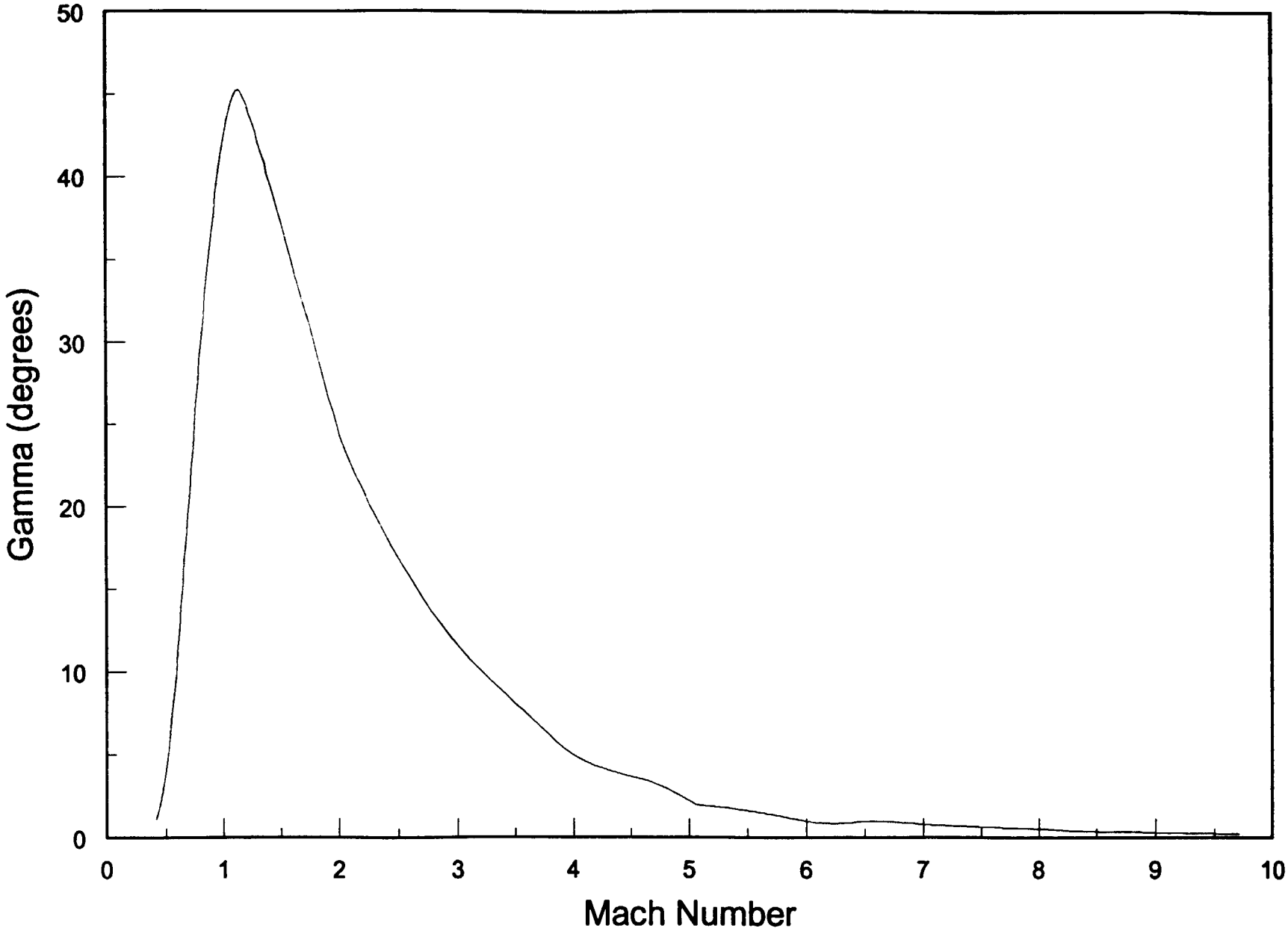

Figure 35. Gamma vs Mach number - phase II model
First 500 seconds of flight

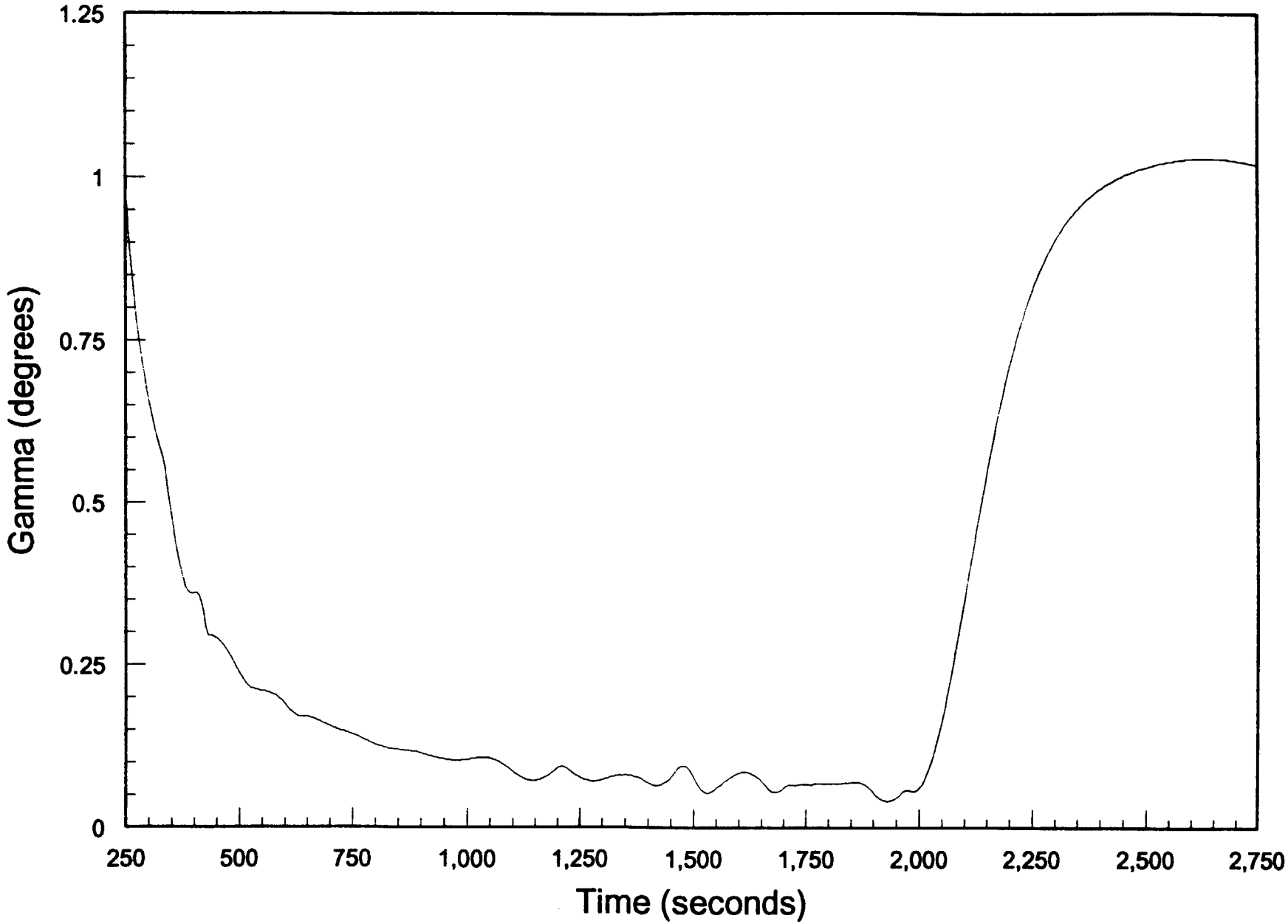

Figure 36. Gamma vs time - phase II model
Starting 250 seconds after takeoff

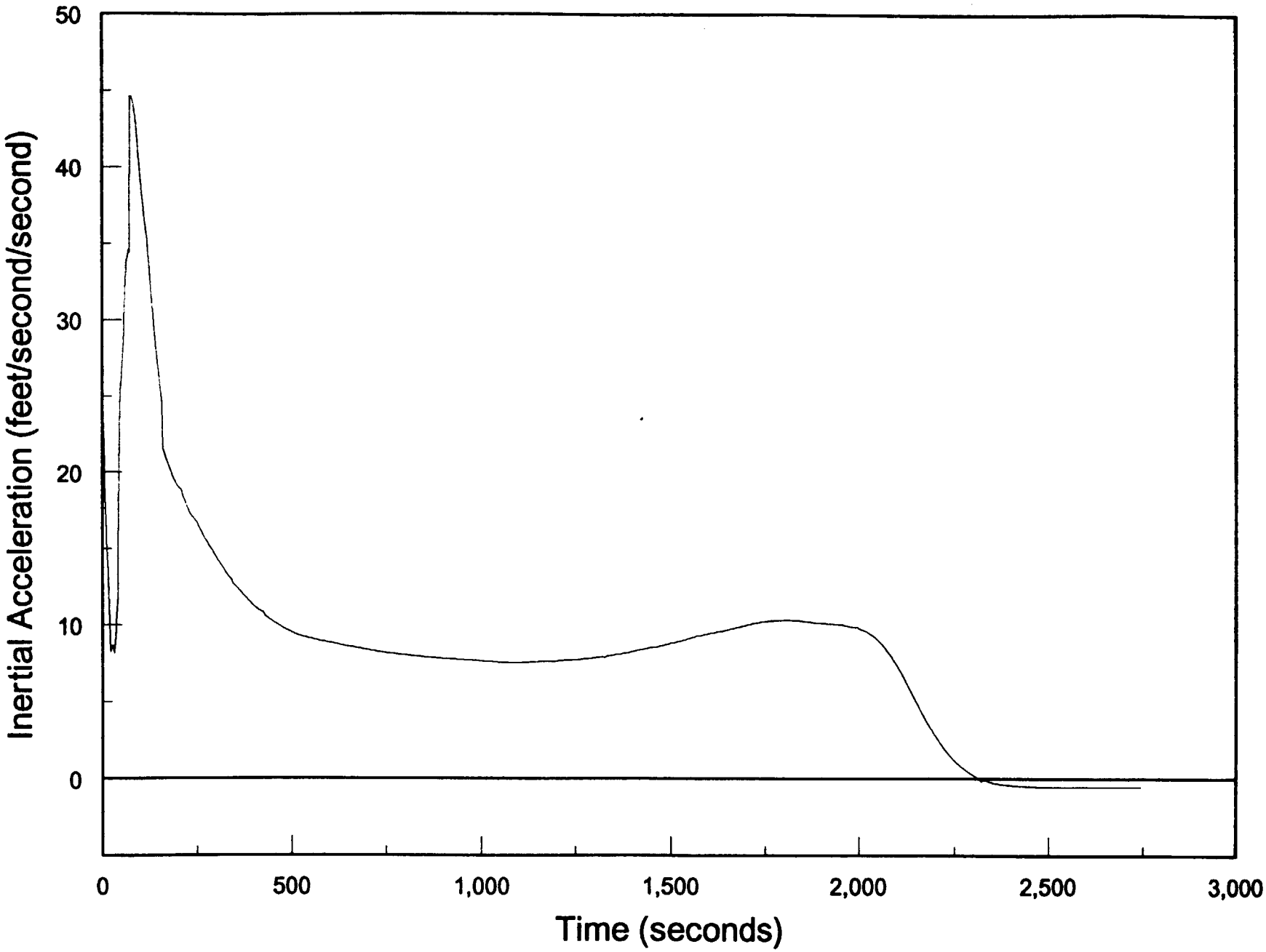

Figure 37. Accel. vs time - phase II model

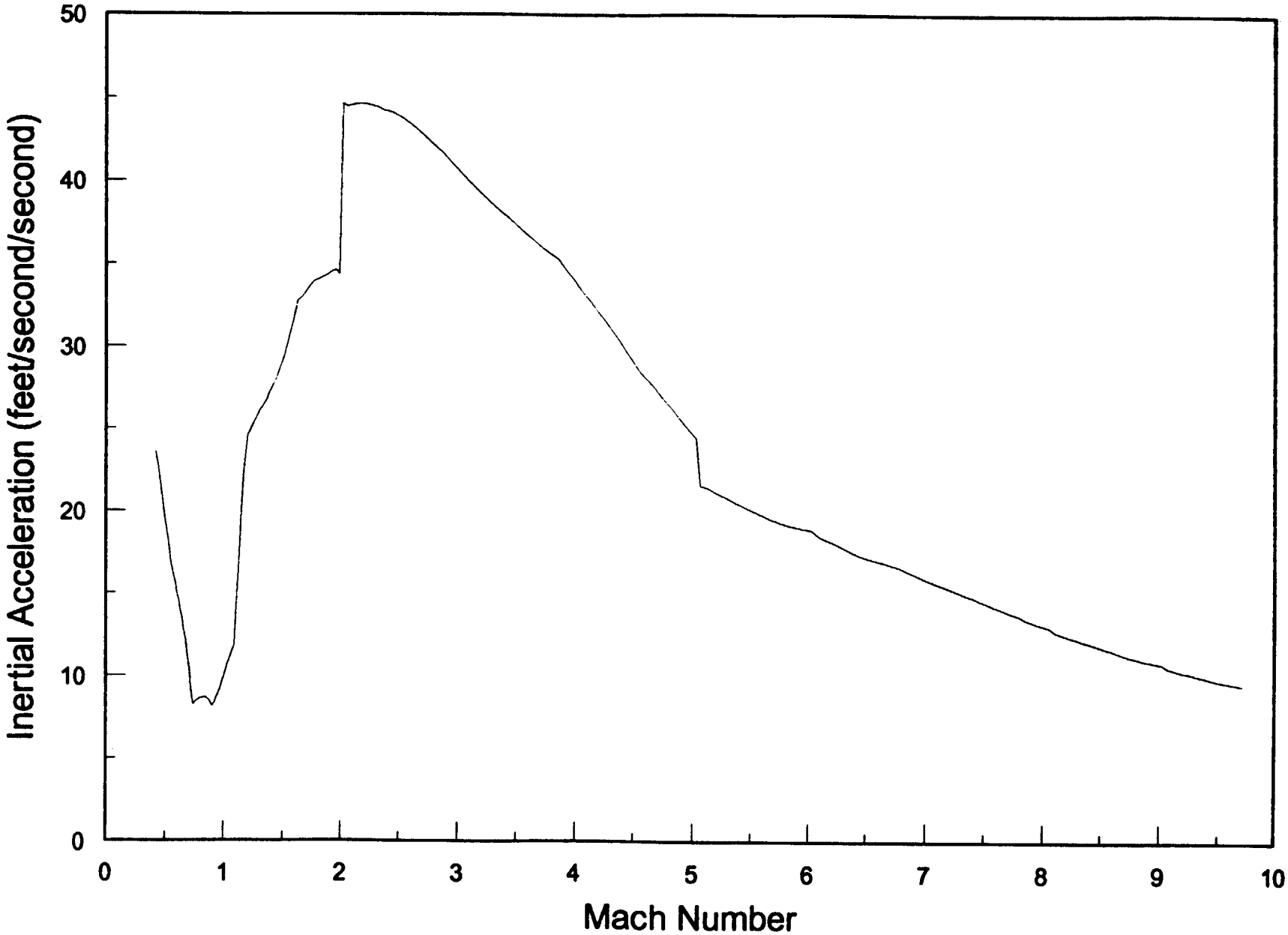

Figure 38. Accel. vs Mach - phase II model
First 500 seconds of flight

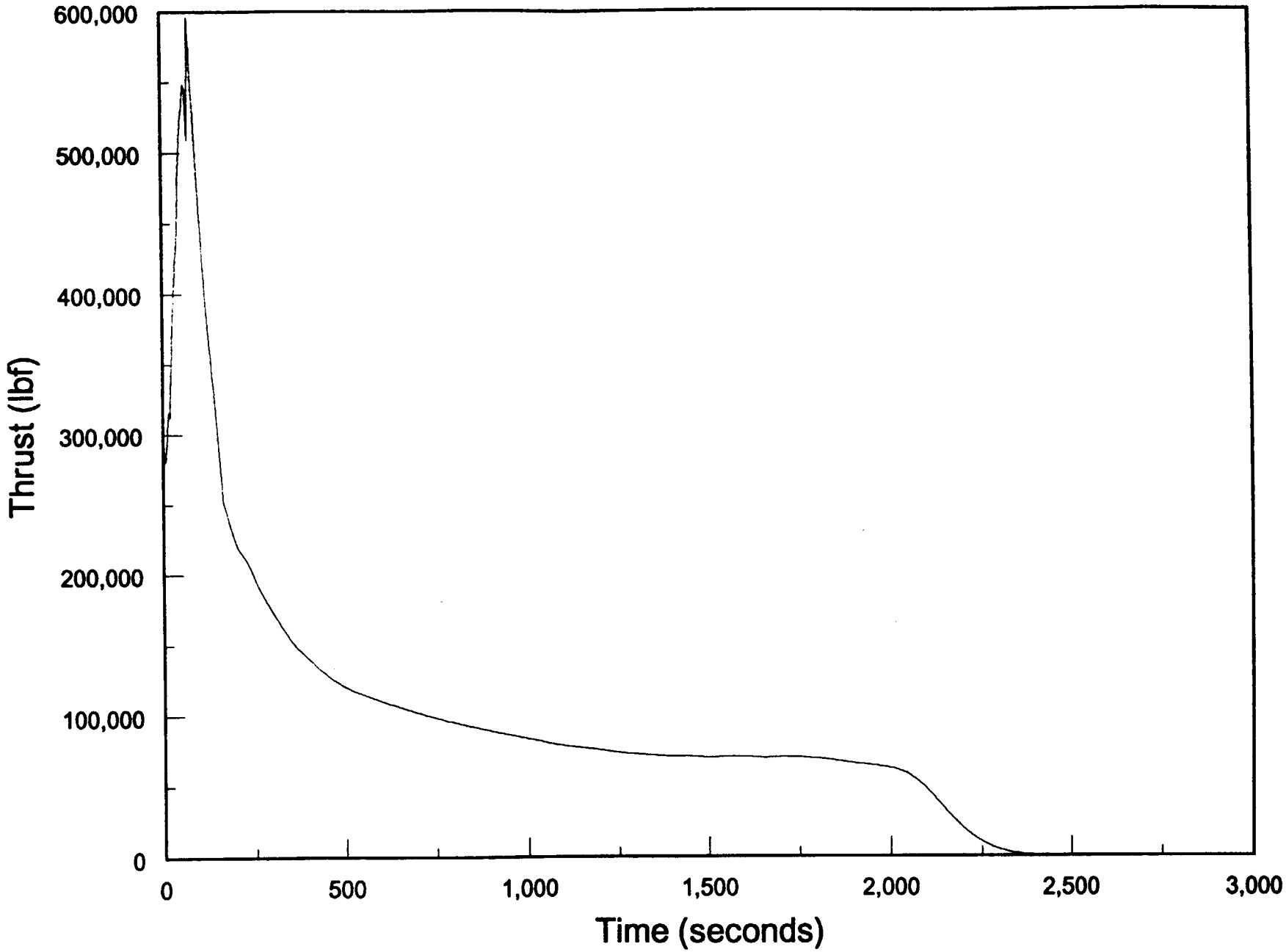

Figure 39. Thrust vs time - phase II model

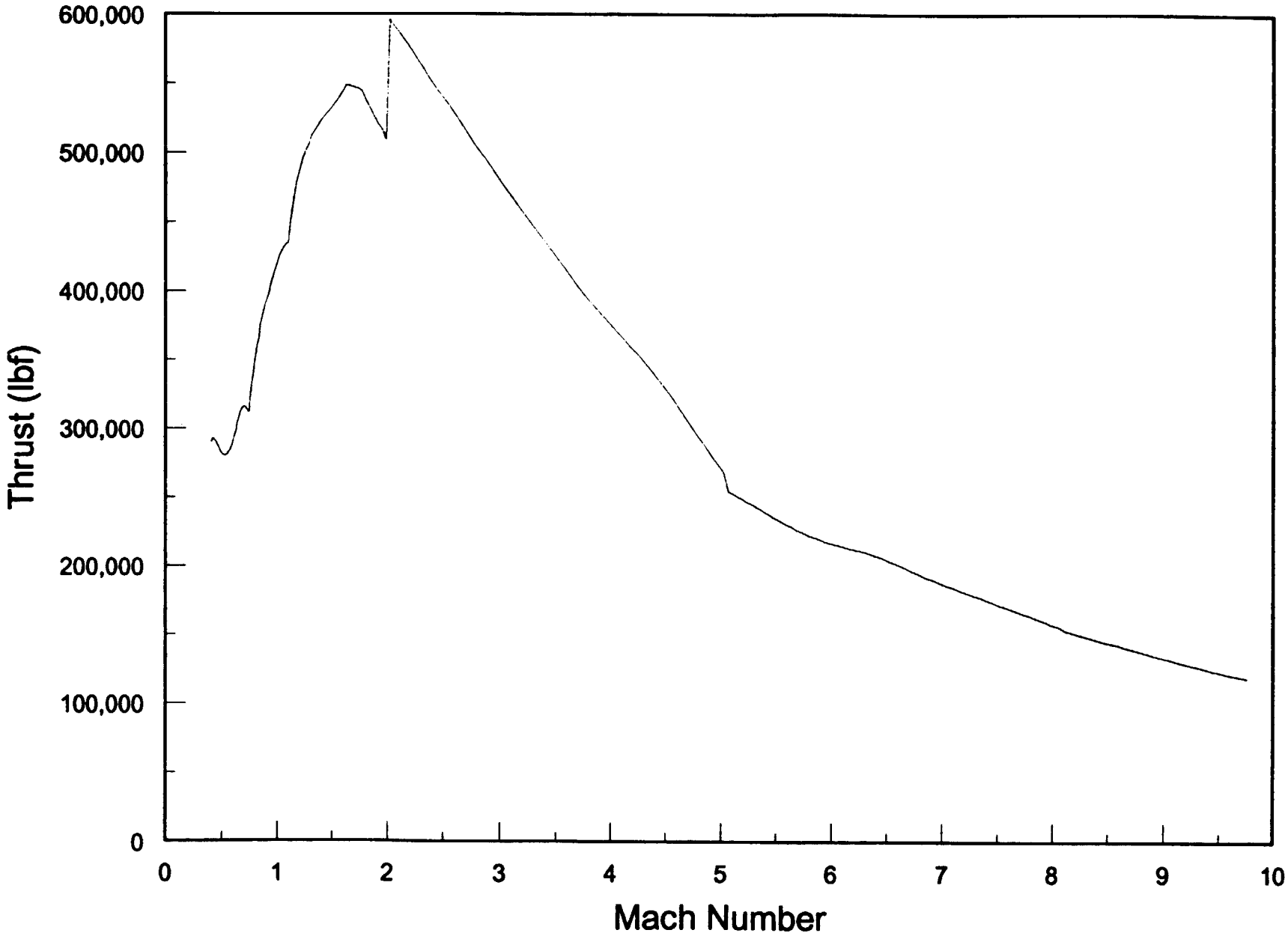

Figure 40. Thrust vs Mach - phase II model
First 500 seconds of flight

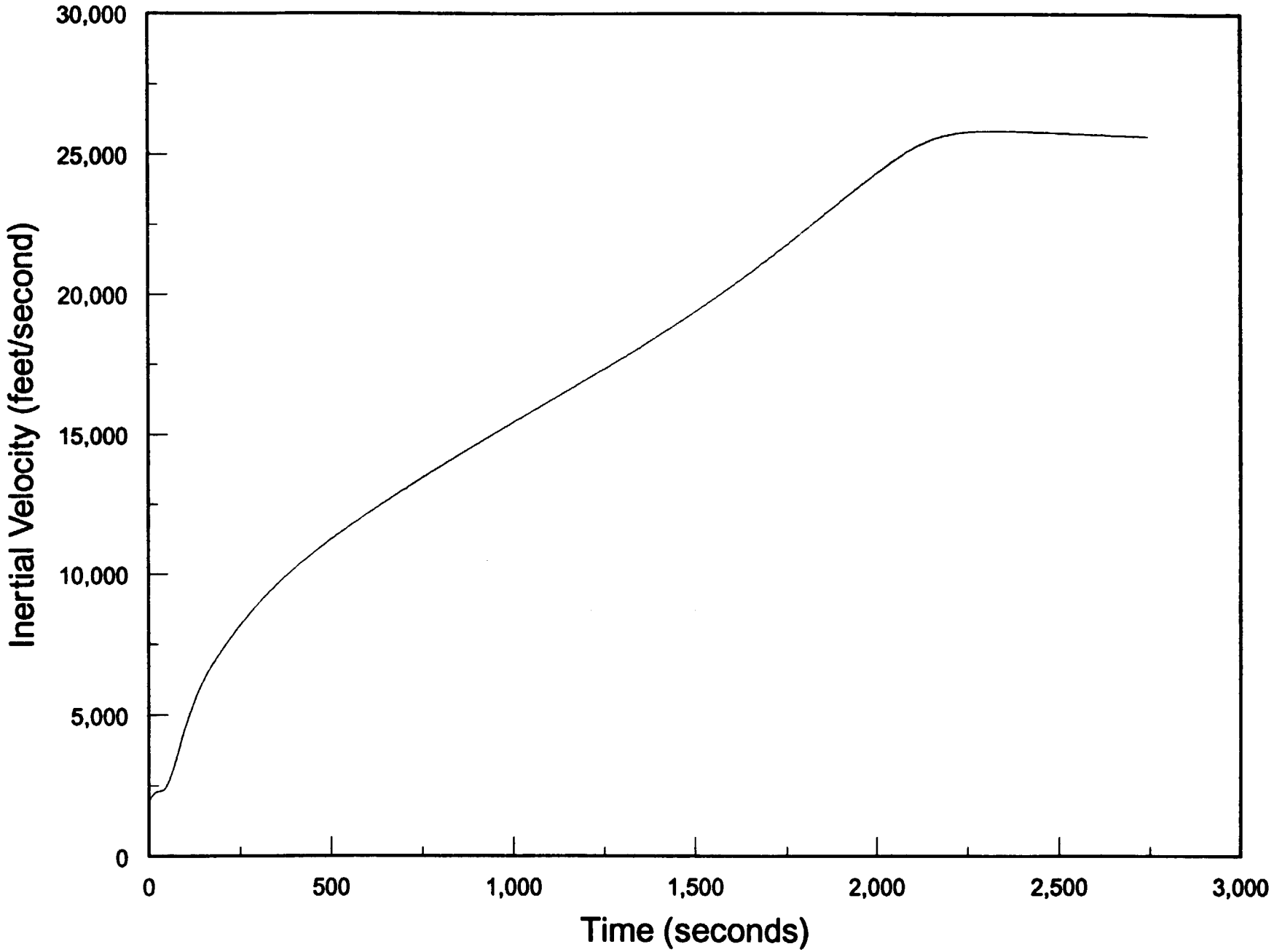

Figure 41. Velocity vs time - phase II model

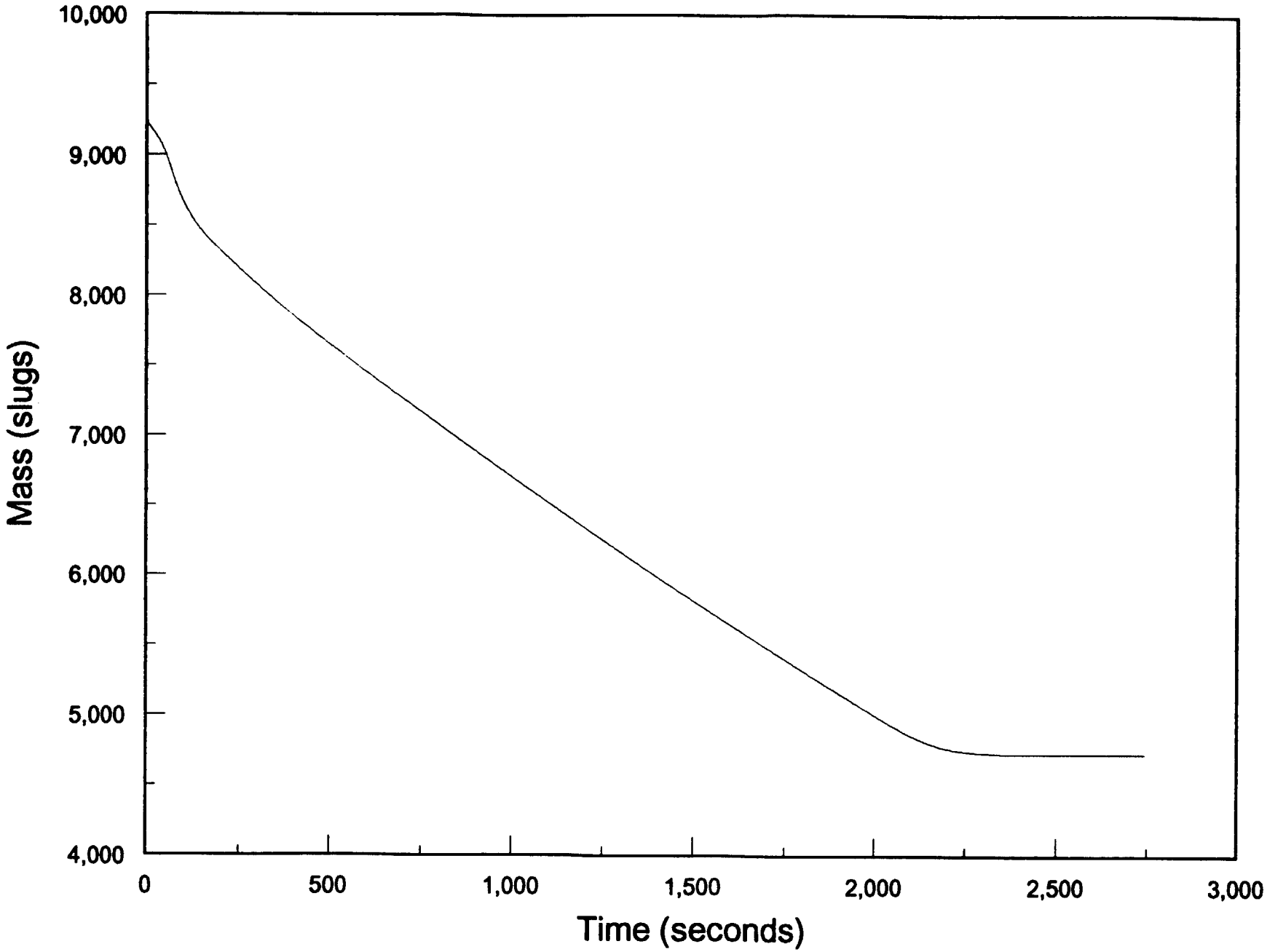

Figure 42. Mass vs time - phase II model

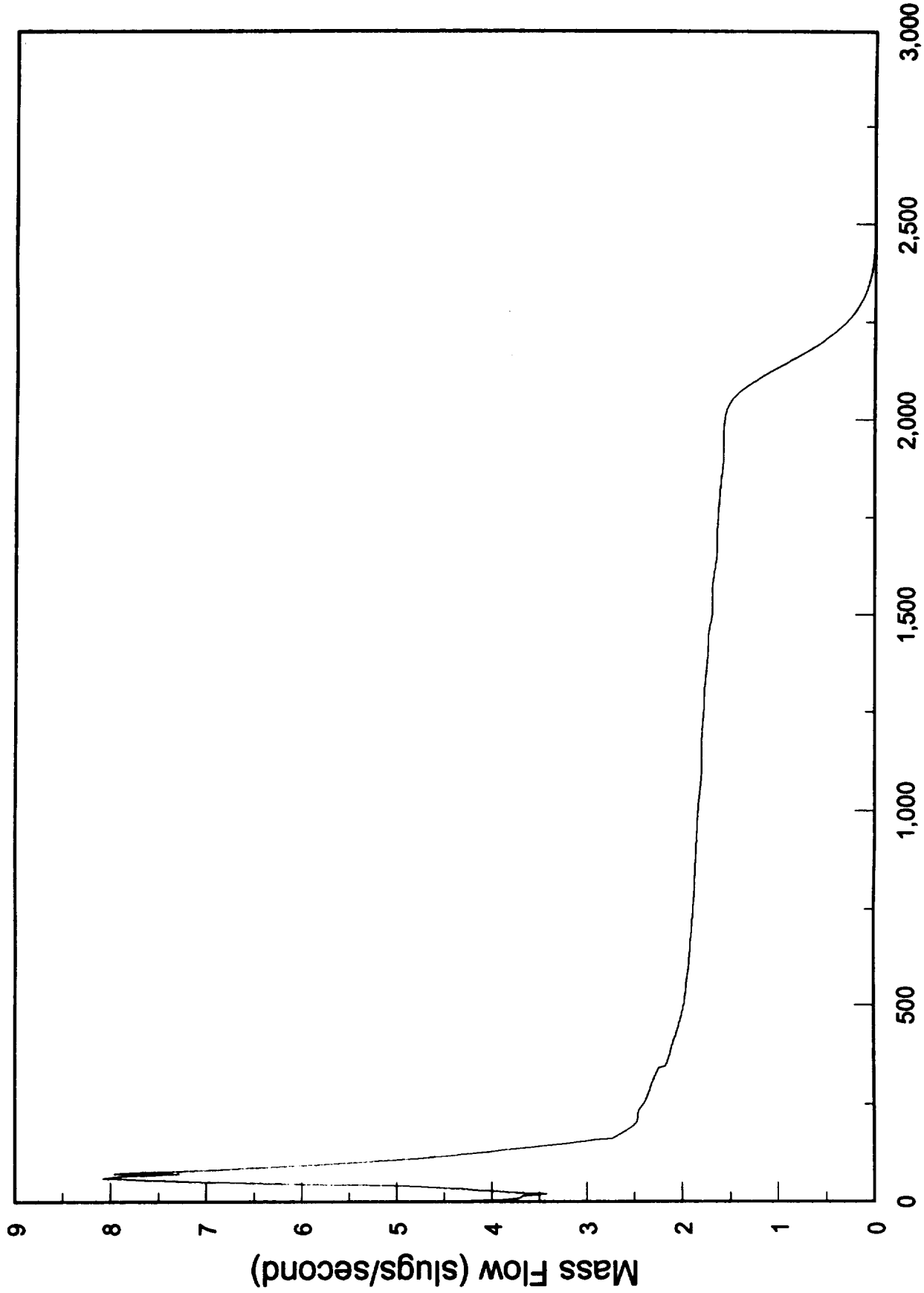

Figure 43. Mass flow vs time - phase II model

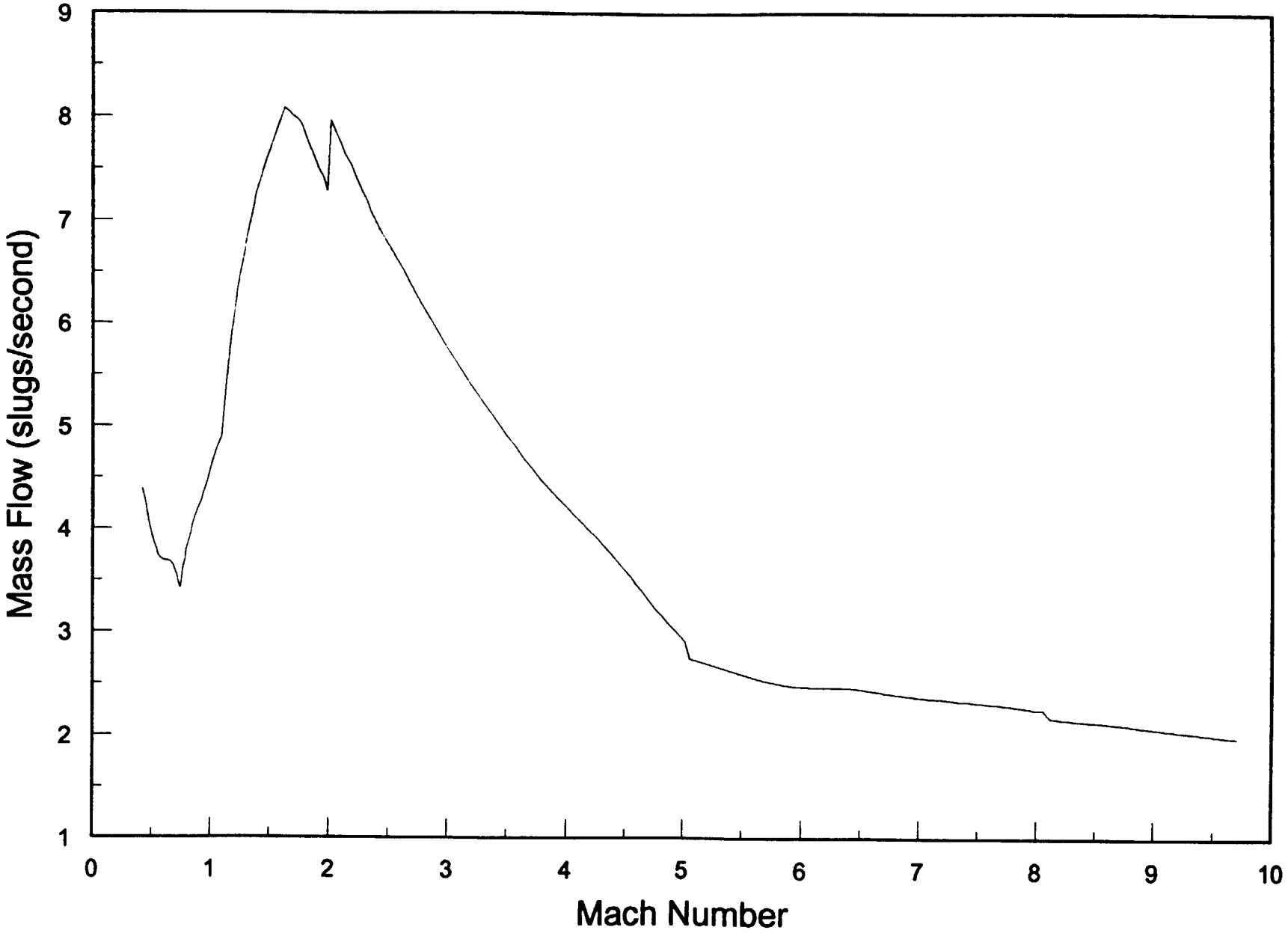

Figure 44. Mass flow vs Mach - phase II model
First 500 seconds of flight

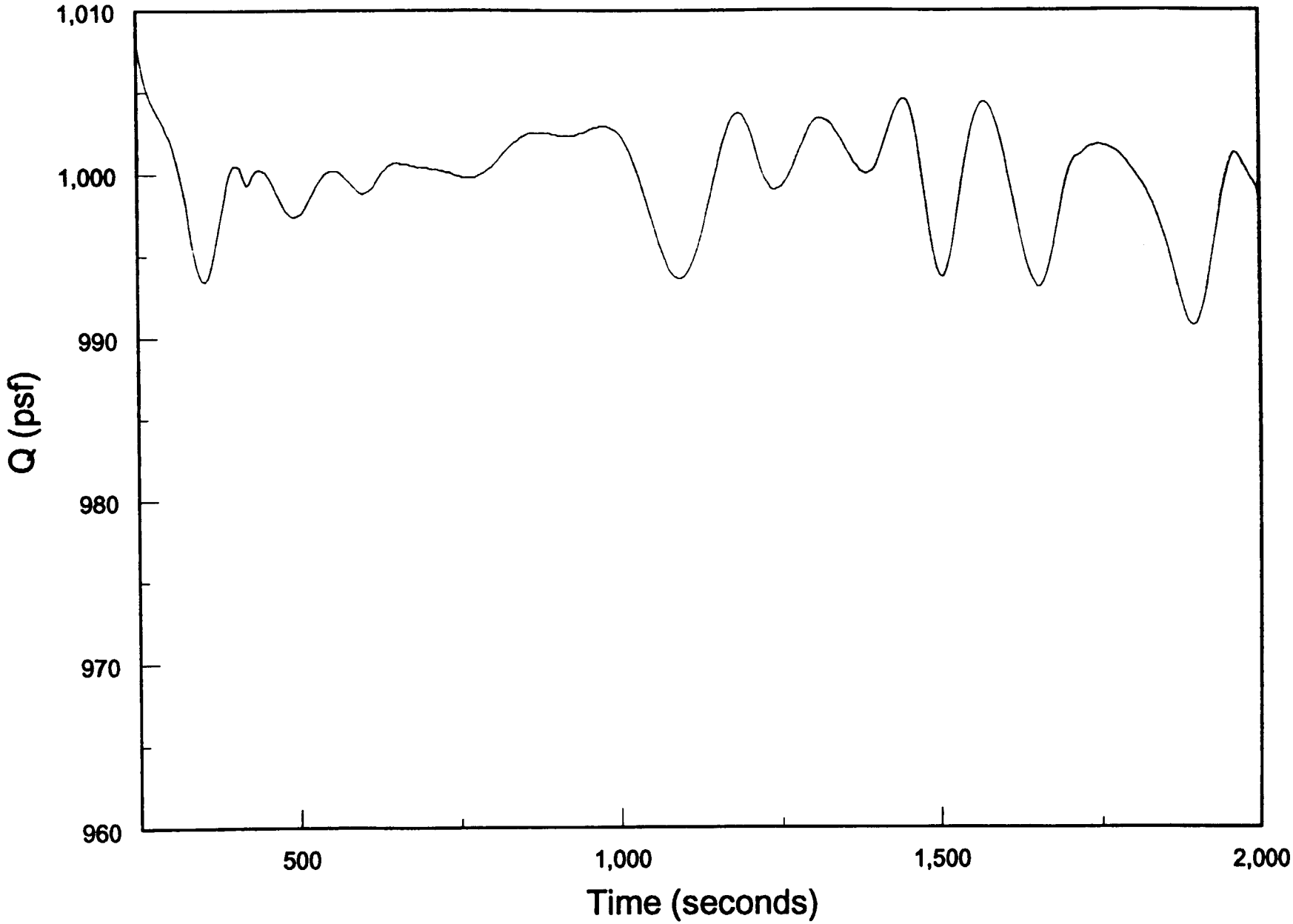

Figure 45. Q vs time - phase II model
From 250 to 2000 seconds after takeoff

REPORT DOCUMENTATION PAGE

Form Approved
OMB No. 0704-0188

1. AGENCY USE ONLY (Leave blank)	2. REPORT DATE	3. REPORT TYPE AND DATES COVERED
	October 1992	Contractor Report

4. TITLE AND SUBTITLE
Air-Breathing Hypersonic Vehicle Guidance and Control Studies: An Integrated Trajectory/Control Analysis Methodology - Phase II

5. FUNDING NUMBERS
C NAS1-18565
WU 505-70-64-01

6. AUTHOR(S)
Philip D. Hattis and Harvey L. Malchow

7. PERFORMING ORGANIZATION NAME(S) AND ADDRESS(ES)
The Charles Stark Draper Laboratory, Inc.
555 Technology Square
Cambridge, MA 02139-3563

8. PERFORMING ORGANIZATION REPORT NUMBER

9. SPONSORING/MONITORING AGENCY NAME(S) AND ADDRESS(ES)
National Aeronautics and Space Administration
Langley Research Center
Hampton, VA 23665-5225

10. SPONSORING/MONITORING AGENCY REPORT NUMBER
NASA CR-189703

11. SUPPLEMENTARY NOTES
Langley Technical Monitor: John D. Shaughnessy
Final Report - Task 13

12a. DISTRIBUTION/AVAILABILITY STATEMENT
Unclassified-Unlimited

Subject Category 08

12b. DISTRIBUTION CODE

13. ABSTRACT *(Maximum 200 words)*

An integrated trajectory/control analysis algorithm has been used to generate trajectories and desired control strategies for two different hypersonic air-breathing vehicle models and orbit targets. Both models used cubic spline curve fit tabulated winged-cone accelerator vehicle representations. Near-fuel-optimal, horizontal takeoff trajectories, imposing a dynamic pressure limit of 1000 psf, were developed. The first model analysis case involved a polar orbit and included the dynamic effects of using elevons to maintain longitudinal trim. Analysis results indicated problems with the adequacy of the propulsion model and highlighted dynamic pressure/altitude instabilities when using vehicle angle of attack as a control variable. Also, the magnitude of computed elevon deflections to maintain trim suggested a need for alternative pitch moment management strategies. The second analysis case was reformulated to use vehicle pitch attitude relative to the local vertical as the control variable. A new, more realistic, air-breathing propulsion model was incorporated. Pitch trim calculations were dropped and an equatorial orbit was specified. Changes in flight characteristics due to the new propulsion model have been identified. Flight regimes demanding rapid attitude changes have been noted. Also, some issues that would affect design of closed-loop controllers were ascertained.

14. SUBJECT TERMS
Air-breathing hypersonic vehicles; Constrained trajectories; Data smoothing; Generic hypersonic guidance and control; Near-minimum-fuel trajectories; Single-stage-to-orbit

15. NUMBER OF PAGES
85

16. PRICE CODE
A05

17. SECURITY CLASSIFICATION OF REPORT	18. SECURITY CLASSIFICATION OF THIS PAGE	19. SECURITY CLASSIFICATION OF ABSTRACT	20. LIMITATION OF ABSTRACT
Unclassified	Unclassified		